University of Alberta

Paleomagnetic and petromagnetic studies of Chinese Cenozoic sediments: Paleoclimatic, tectonic, and evolutionary implications

by

Rui Zhang

A thesis submitted to the Faculty of Graduate Studies and Research
in partial fulfillment of the requirements for the degree of

Doctor of Philosophy
in
Geophysics

Department of Physics

Spring 2011
Edmonton, Alberta

Examining Committee

Dr. René W. Barendregt, Geography, University of Lethbridge (External examiner)

Dr. Duane Froese, Earth and Atmosphere Sciences, University of Alberta (Examiner)

Dr. Moritz Heimpel, Physics, University of Alberta (Chair and Examiner)

Dr. Vadim A. Kravchinsky, Physics, University of Alberta (Supervisor and Examiner)

Dr. Mauricio D. Sacchi, Physics, University of Alberta (Examiner)

Abstract

The anisotropy of magnetic susceptibility (AMS) was investigated in three Chinese Loess Plateau sedimentary sections along a W–E transect. Previously published models assumed that winter monsoons were responsible for the magnetic fabric formation of loess sequences. In our new interpretation, the stronger summer monsoons from the southeast played the major role in magnetic fabric orientation in the studied west and central parts of the Chinese Loess Plateau. The AMS was generated during the rainy summer monsoon when the sedimentary particles including magnetite were rearranged, settled, and fixed. We reconstruct the summer paleomonsoon routes for the last 130 kyr. These winds prevail from SE to NW but appear to be affected by regional topographic factors.

Evidence in the world's ocean current system indicates an abrupt cooling from 34.1 to 33.6 Ma across the Eocene-Oligocene boundary (EOB) at 33.9 Ma. I describe and date with magnetostratigraphy a section from the north Junggar Basin (Burqin section). Three fossil assemblages revealed through the EOB (34.8, 33.7, and 30.4 Ma) demonstrate that perissodactyl faunas were abruptly replaced by rodent/lagomorph-dominant faunas during climate cooling, and the changes in mammalian communities were accelerated by aridification in central Asia.

Paleomagnetic studies of two sections of the northern Junggar Basin, China, are presented from Burqin and Tieersihabahe. Our paleomagnetic results

demonstrate counterclockwise tectonic rotations in Burqin and Tieersihabahe (–17.2 ± 9.6° and –11.8 ± 6.1°, respectively) as well as considerable northward latitudinal displacement (12.2 ± 6.5° and 9.7 ± 4.1°, respectively) with respect to Europe. These results are consistent with the motions of contiguous blocks in the same geological time intervals (India, north and south China, Tarim, Amuria, and Kazakhstan). No significant intracontinental shortening or vertical-axis rotation is observed for the Junggar block from 40 Ma to 20 Ma. Our results reveal that the major compression and rotation between Junggar and northern Europe occurred after 20 Ma due to continuous penetration of India into Asia. We interpret the uplift of the Altay Mountains and the formation of the Lake Baikal rift system to be due to such intracontinental compression and relative rotations.

Acknowledgements

Foremost, I would like to express my sincere gratitude to my supervisor Dr. Vadim A. Kravchinsky for his continuous support of my Ph.D. study and research, for his patience, motivation, enthusiasm, and immense knowledge. His guidance helped me in all the time of research and writing of this thesis. I could not have imagined having a better advisor and mentor for my Ph.D.

Besides my advisor, I would like to thank the rest of my thesis committee: Dr. René W. Barendregt, Dr. Duane Froese, Dr. Moritz Heimpel and Dr. Mauricio D. Sacchi for their encouragement, insightful comments, and hard questions.

My sincere thanks also goes to Dr. Douglas R. Schmitt and Dr. Claire Currie for offering me the summer field school opportunities and leading me working on diverse and exciting projects.

I thank our Paleomagnetism Group: Luda P. Koukhar, Ted Evans, Shawn Walker, Jeff Samson, Dunia Blanco and Karol Rohraff for the lab assistance and stimulating discussions. I would express my gratitude to Len Tober and Lucas Duerksen for their technical assistance. Also I thank the staff of the Physics Department for their help. In particular, I am grateful to Sarah Derr for her hard work in helping the graduate students in our Department. I thank Heather Schijins, Volkan Tuncer, Jianjun Gao, Helen Yam, Long Zhang, Xuefeng Duo and other friends in the Physics Department for their support and encourage.

Last but not the least, I would like to thank my family: my parents Lisheng Zhang and Zhi Cheng, parents-in-law Zhiming Liu and Xiaoyun Su for

supporting me spiritually throughout my life. I am deeply grateful to my wife Na Liu who has dedicated her effort to my study and work.

Content Table

Chapter 1

Introduction

Chapter 2

Paleomonsoon route reconstruction along a W–E transect in the Chinese Loess Plateau using the anisotropy of magnetic susceptibility: summer monsoon model

Chapter 3

A Continuous Record of Magnetostratigraphy and Mammalian Evolution across the Eocene-Oligocene Transition in the North Junggar Basin

List of Tables

List of Figures

parameters and TL ages are from Porter and An (1995); the marine oxygen isotope reference curve is from Bassinot et al. (1994). 1 – loess intervals, 2 – paleosol intervals, 3 – underdeveloped paleosol.

Figure 2.5. (a) Plots of ε_{12} (the 95% confidence ellipse of K_{max} in the plane joining K_{max} and K_{int}) against lineation. The plots demonstrate inverse relationship between ε_{12} and lineation. (b) Plots of ε_{12} against foliation. The plots demonstrate independence between ε_{12} and foliation. (c) Plots of ε_{23} (the 95% confidence ellipse of K_{min} in the plane joining K_{min} and K_{int}) against foliation. BCY – Baicaoyuan, XF – Xifeng, and YC – Yichuan sections. The inserts are the frequency distributions of ε_{12} using 2° bin sizes and ε_{23} using 0.5° bin sizes. They demonstrate that majority of the samples satisfies statistically significant level of $\varepsilon_{12} < 22.5°$ (70.1% for BCY, 86.6% for XF, and 92.3% for YC). The significance level of ε_{23} is < 11.25° for absolute majority of the samples.

Figure 2.6 AMS results for the Baicaoyuan section: stereographic projection of K_{max} (red dots) and K_{min} (green triangles) (a, d); contours and rose diagram of K_{max} (b, e); contours of K_{min} (c, f). Parameter n is a number of samples included to the analysis. Legend corresponds to a percentage of the samples falling in the indicated by the color contour lines for K_{max} (left) and K_{min} (right).

Figure 2.7 AMS results for the Xifeng section: stereographic projection of K_{max} (red dots) and K_{min} (green triangles) (a, d); contours and rose diagram of K_{max} (b, e); contours of K_{min} (c, f). Parameter n is a number of samples included to the analysis. Legend corresponds to a percentage of the samples falling in the indicated by the color contour lines for K_{max} (left) and K_{min} (right).

Figure 2.8 AMS results for the Yichuan section: stereographic projection of K_{max} (red dots) and K_{min} (green triangles) (a, d); contours and rose diagram of K_{max} (b, e); contours of K_{min} (c, f). Parameter n is a number of samples included to the analysis. Legend corresponds to a percentage of the samples

falling in the indicated by the color contour lines for K_{max} (left) and K_{min} (right).

Figure 2.9 AMS results of selected samples where $\varepsilon_{12} < 11.25^{o}$ and I - $K_{min} > 70^{o}$ for Baicaoyuan (BCY), Xifeng (XF), and Yichuan (YC) sections. Left: stereographic projection of K_{max} (red dots) and K_{min} (green triangles). Center: contour lines and rose diagrams of K_{max}.. Right: contour lines of K_{min}. Parameter n is a number of samples included to the analysis. Legend corresponds to a percentage of the samples falling in the indicated by the color contour lines for K_{max} (left) and K_{min} (right).

Figure 2.10 Illustration of the Bootstrap statistics applied for the mean direction of the AMS ellipsoid for the for Baicaoyuan (BCY), Xifeng (XF), and Yichuan (YC) sections (see also Table 3). The dataset for all samples of L_1 and S_1 horizons is included in this illustration although datasets with $\varepsilon_{12} < 22.5^{o}$ and $\varepsilon_{12} < 11.25^{o}$ show very similar results. Rose diagram for K_{max} is shown in red and for K_{min} is shown in grey color. Bootstrap ellipsoids for eigenvectors of K_{max} (red), K_{int} (blue) and K_{min} (green). Calculations are done using AGICO's software package for the KLY magnetic susceptibility meter using technique developed by Constable and Tauxe (1990). (B) Black (red) arrow corresponds to the mean direction for the dominant wind direction calculated using peak orientation (tensor mean) for K_{max}.

Figure 2.11 A model of AMS that depends on the monsoon directions in the southern part of the Chinese Loess Plateau.

(a) The winter monsoon brings sedimentary and magnetic particles with the dust from the NW. The AMS ellipsoid would reflect the prevailing orientation of the particles as shown in the stereonet below (lower hemisphere projection).

(b) The summer monsoon brings rain and wind from the SE, reorienting and finally fixing sedimentary and magnetic grains in the uppermost seasonally formed layer of loess or soil. The AMS ellipsoid is now oriented in a direction opposite to the winter monsoon direction. Rain helps to settle the sedimentary and magnetic grains and the growing summer vegetation fixes

them in-situ. Grains become immobile. The next winter monsoon covers the site with new eolian material and the process repeats.

Figure 2.12. Surface wind vectors for (A) the winter months of November-March and (B) the summer months of May-September are calculated from the 1950 to 2009 monthly long-term means. Data was compiled by the NOAA-CIRES's NCEP Reanalysis Atlas. Contours are wind velocities in meters per second. In the loess deposits, winter prevailing surface winds come from NW, SW while summer prevailing winds comes from the SSE, SE.

Figure 2.13 Dominant summer monsoon routes for last 130 kyrs reconstructed from our AMS analysis along the west-central transect across the Chinese Loess Plateau. Arrows illustrate the ancient summer monsoon wind direction; the relative strength of the wind is specified by the comment near each local wind model stereographic projection.

Above: lower hemisphere stereographic projections showing the contour lines and rose diagrams for K_{max} for all studied samples with arrows pointing toward major summer monsoon directions in every locality. Below: lower hemisphere stereographic projection of K_{max} and K_{min} from two other localities. Note that original figures in Thistlewood and Sun (1991) are shown for the upper hemisphere.

Figure 3.1 (A) Study area in Asia. (B) Location of the Junggar basin and Burqin section.

Figure 3.2 Detailed magnetostratigraphy of the studied section and its correlation with the GPTS of Cande and Kent (1995). EOB is at 33.9 Ma (Gradstein et al., 2004). Marine oxygen isotope curve is from Coxall et al (2005). Terrestrial EOT in the Junggar Basin is constricted in this study.

1 – mudstone, 2 – siltstone, 3 – fine sandstone, 4 – intermediate size sandstone, 5 – coarse sandstone, 6 – conglomerate, 7 – normal polarity interval, 8 – reversed polarity, 9 – uncertain polarity, 10 – perissodactyl-dominant mammalian fossils, 11 – rodent/lagomorph dominant fossils.

and Courtillot (2002). Close (open) circles represent sedimentary (volcanic) data. Sources are presented in table 4.2.

Figure 4.8 Compilation of paleomagnetic poleward displacements and rotation for Asia from 25 Ma to 14 Ma. Poleward displacement and rotations were calculated respect to Eurasia APWP of Besse and Courtillot (2002). Close (open) circles represent sedimentary (volcanic) data. Data from mountains areas are represents as green circle. Sources are presented in table 4.3.

Chapter 1

Introduction

1.1 Basic Principles of Petromagnetism

Magnetism arises from the motion of electrically charged particles. In natural materials, magnetization originates from the intrinsic electron spin and the orbital motion of electrons around the atomic nucleus.

When a magnetic field H is applied to a substance the electron motion is modified, resulting in an induced magnetization M. The relationship between M and H is:

$$M=K\times H=K\frac{B}{\mu_0},$$

where M is the magnetic dipole moment per unit volume in Ampere per meter (A/m), H is the magnetic field strength (A/m), B is the fundamental field strength measured in Tesla (also called magnetic induction), μ_0 is the permeability of free space ($4\pi\times10^{-7}$ Henry/m), and K is the magnetic susceptibility (dimensionless).

In general, all materials are magnetic, however some materials are more magnetic than others. The main reason for the difference is the strength of the interaction of atomic magnetic moments in the material. The overall magnetic properties depend on how all the magnetic moments superpose on each other. Macroscopically, these effects determine how the material will behave when it is placed in an external magnetic field H. Magnetic behavior can be classified into the three major groups described below.

Diamagnetic Materials

In diamagnetic materials (Figure 1.1) all electrons are paired so that the magnetic moments associated with the electronic spins are compensated and a net magnetic moment arises only from orbital movements. When an external magnetic field is applied to a diamagnetic material, the angular momentum vector associated with the orbits precesses around the direction of the applied field with an angular velocity proportional to the applied field. The magnetic moment associated with the precession is induced in a direction opposite to the applied field. All materials have diamagnetic properties but a paramagnetic or ferromagnetic response masks the weaker diamagnetic behavior. Magnetization (defined as the quantity of magnetic moment per unit volume) disappears when the applied magnetic field is removed (Butler, 1992; Dunlop and Őzdemir et al., 1997).

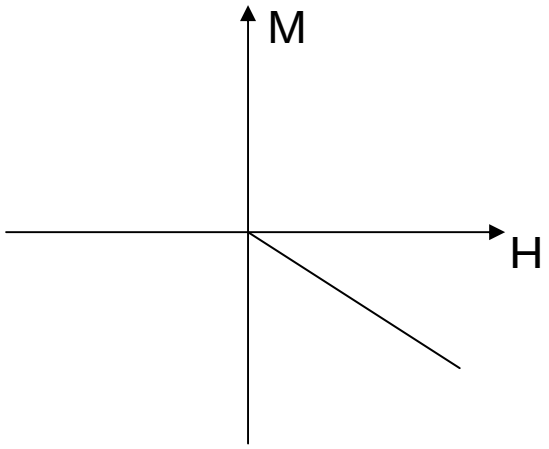

Figure 1.1 Magnetization M versus magnetic field H for a diamagnetic material (examples of diamagnetic minerals are quartz, plagioclase, calcite, and apatite).

Paramagnetic Materials

Materials containing atoms with unpaired electron spins exhibit paramagnetism (Figure 1.2), where the magnetic moment per atom has a nonzero

value and a resultant moment arises in the material when a magnetic field is applied. This net magnetization is in the field direction and persists until the applied field is removed (Butler, 1992; Dunlop and Őzdemir, 1997).

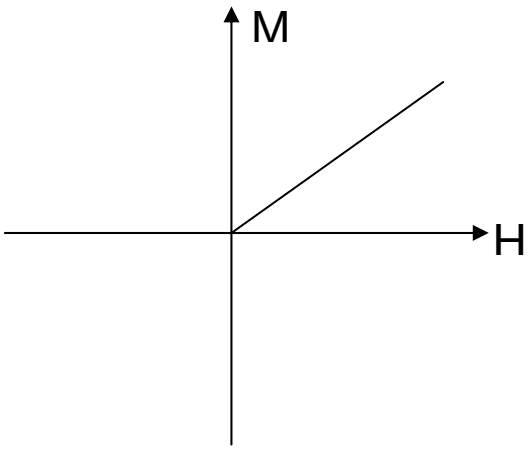

Figure 1.2 Magnetization M versus magnetic field H for a paramagnetic material (examples of paramagnetic minerals are biotite, olivine, serpentinite, and chromite).

Ferromagnetic Materials

Ferromagnetism

Similar to paramagnetic materials, ferromagnetic materials (Figure 1.3) have uncompensated spins. Magnetization is produced when adjacent atomic moments of the electrons interact in the absence of an external field. If the distance between neighbor atoms is small enough, the atomic orbitals overlap. In the simplest case of two electrons, the energy of the system is not the sum of the energy of the individual electrons; it contains an additional quantum mechanical term to account for the exchange energy between electrons. The exchange energy represents the interaction between the magnetic moments of the electrons and is minimized by alignment of the atomic moments of the electrons in the absence of an external magnetic field (Butler, 1992; Dunlop and Őzdemir, 1997).

Ferrimagnetism and antiferromagnetism

In ferrimagnetic materials (Figure 1.4), the magnetization of each sublattice has a different intensity and antiparallel direction. Remanent magnetization persists in the absence of an external magnetic field below the Curie temperature, but disappears above the Curie temperature, where the material behaves paramagnetically. The most important ferrimagnetic mineral is magnetite, the most magnetic of all the naturally occurring minerals on Earth (Tarling and Hrouda, 1993).

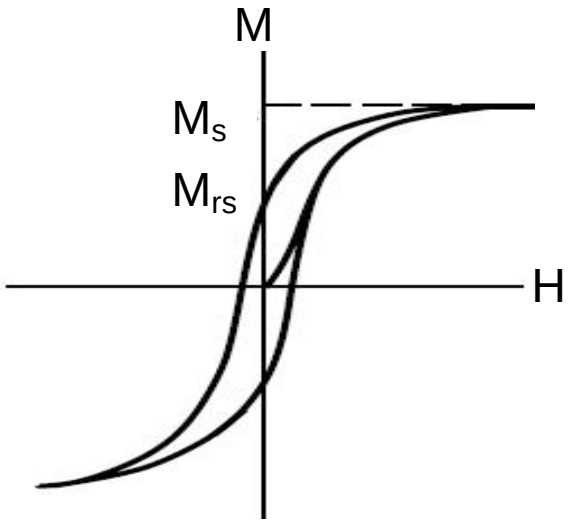

Figure 1.3 Magnetization M versus magnetic field H for a ferromagnetic (similar to a ferrimagnetic) material. The magnetization exhibits a hysteresis loop. Saturation magnetization (M_s) is reached when the external magnetic field cannot increase the magnetization of the material further; saturation remanence (M_{rs}) is the magnetization remaining in zero field after the saturation field is applied.

In antiferromagnetic materials (Figure 1.4), the magnetic moments of atoms or molecules align in opposite positions, similar to ferromagnetic and ferrimagnetic materials. When no external field is applied, the opposing moments are usually equal and no spontaneous magnetization remains. In some cases, a kind of ferrimagnetic behavior may be displayed in the antiferromagnetic phase.

An example is hematite which is antiferromagnetic with a weak parasitic ferromagnetism that results from either spin-canting or defect ferromagnetism.

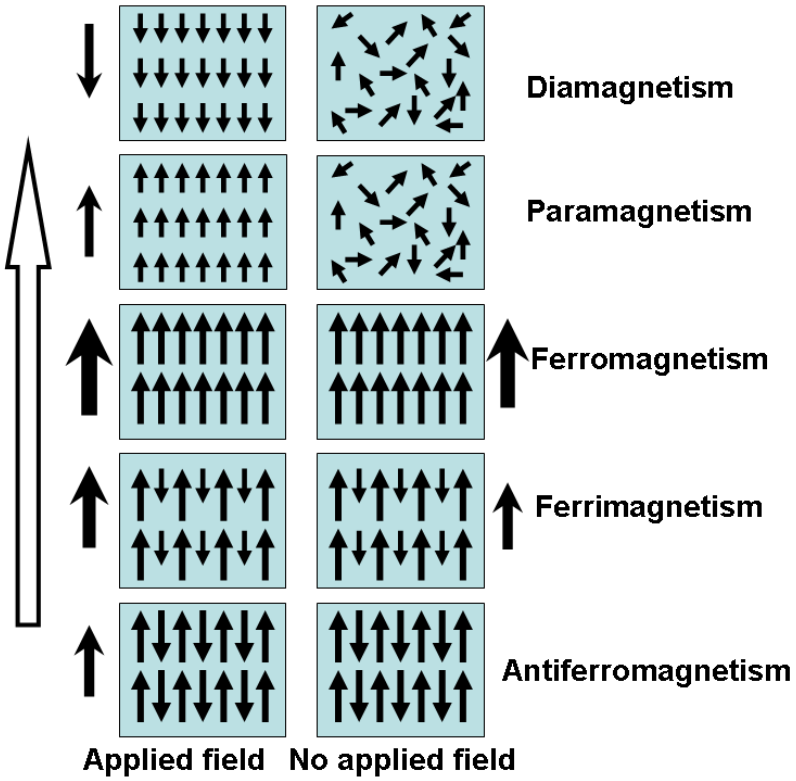

Figure 1.4 Different forms of magnetization (modified from Tarling and Hrouda, 1993). The left-hand column shows the total magnetization (solid arrow) that a substance acquires when in an applied magnetic field (hollow arrow). The right-hand column illustrates the magnetization after the field is removed. The small arrows inside the frames represent the magnetic moment in the material.

1.2 Magnetic Anisotropy

The majority of igneous rocks are magnetically isotropic because the magnetic materials they contain are randomly oriented. As noted earlier, the variation of magnetic susceptibility with orientation is called the anisotropy of magnetic susceptibility. In most rock and sedimentary samples, the strength of the magnetization induced by a weak field of constant strength depends on the

orientation of the sample within the field. Such materials are magnetically anisotropic. The variation of magnetic susceptibility with orientation can be described mathematically in terms of a second-rank tensor and can be visualized as a magnetic susceptibility ellipsoid (e.g. Janák, 1965; Jelinek, 1977, 1978; Tarling and Hrouda, 1993; Borradaile et al., 1997; Dunlop and Őzdemir, 1997) (Figure 1.5). The magnetic anisotropy of magnetic susceptibility used in most published articles is determined from measurements of magnetic susceptibility in a weak field (≤ 1 mT) unless specifically stated.

There are three different types of magnetic anisotropy:

- magnetocrystalline anisotropy
- stress anisotropy
- shape anisotropy

Magnetocrystalline anisotropy, also called crystalline anisotropy, arises from the action of lattice forces on the electron-spin configuration along a specific direction termed the easy plane or the easy axis. Stress anisotropy is related to spin-orbit coupling called magnetostriction. Magnetostriction arises from a strain dependence on magnetic anisotropy constants. Shape anisotropy is due to the shape of a mineral grain. The surface charge distribution of a magnetic mineral is another source of a magnetic field (Tarling and Hrouda, 1993).

Rocks usually contain a variety of minerals – ferromagnetic, paramagnetic, and diamagnetic – each grain of which makes its own contribution to the total magnetic susceptibility. The bulk magnetic susceptibility will thus represent a summation of the magnetic susceptibilities of all the mineral species present in a sample. When applying a weak magnetic field to a solid material, the

demagnetizing field of the sample (which is the magnetic field generated by the magnetization in a magnet field) can usually be neglected except in rocks with a large amount of magnetite. Either direct measurement of induced magnetization or use of systems that respond only to anisotropic magnetic susceptibility can be used to measure magnetic anisotropy.

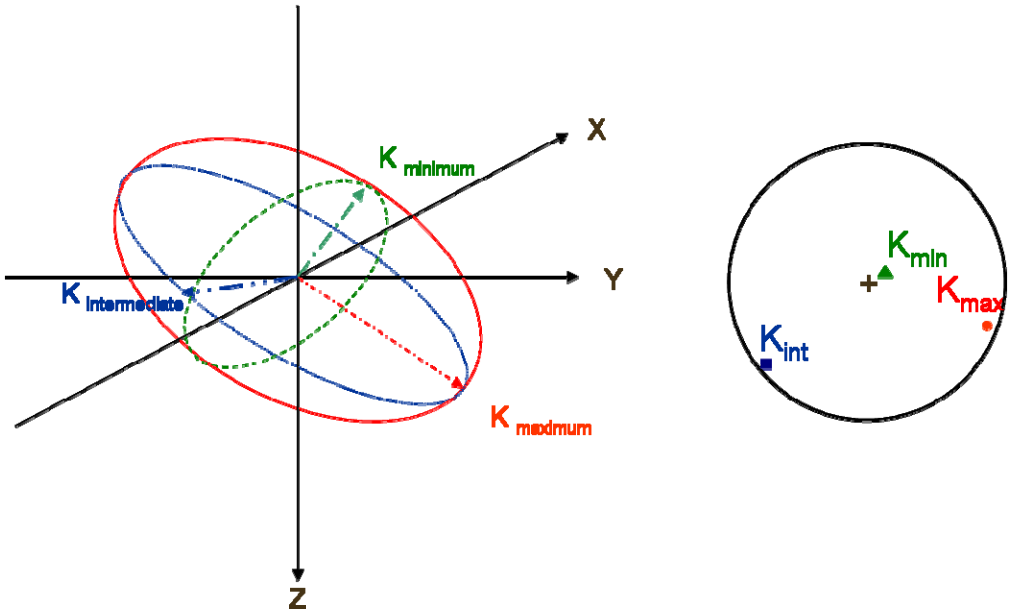

Figure 1.5 Schematic illustration of the magnetic susceptibility ellipsoid in a rock or sediment specimen. Left diagram: the tensor defining the magnetic susceptibility anisotropy of a sample is illustrated by means of an ellipsoid with three orthogonal axes that correspond to the maximum, intermediate, and minimum principal axes ($K_{maximum}$, $K_{intermediate}$, and $K_{minimum}$). Right diagram: stereographic projection of the principal axes of a magnetic susceptibility ellipsoid; K_{min}, K_{int}, and K_{max} correspond to the minimum, intermediate, and maximum principal axes of the ellipsoid.

1.2.1 Mathematical Description and Determination of Anisotropy of Magnetic Susceptibility in Sediments

The aim of a mathematical description of AMS is to give a physical concept of the values measured for magnetic susceptibility. A theory for calculating the

magnetic susceptibility tensor using least-squares techniques has been described by Granar (1958), Girdler (1961), Janák (1965), Jelinek (1977), and Hanna (1977). The following methods can be used to determine the magnetic anisotropy of a material.

a. Measured Magnetic Susceptibility in an Arbitrary Direction

In measurements of rocks (Figure 1.6), i.e., on bodies of relatively small magnetic susceptibility, the demagnetizing field of the sample can usually be neglected. Exceptions are rocks with a large amounts of magnetite. Janák (1965) was first to demonstrate that the magnetization could be expressed by a 3×3 matrix:

$$M_1 = K_{11}H_1 + K_{12}H_2 + K_{12}H_3$$

$$M_2 = K_{21}H_1 + K_{22}H_2 + K_{23}H_3$$

$$M_3 = K_{31}H_1 + K_{32}H_2 + K_{33}H_3,$$

which can be written in the matrix form

$$(M) = (K)(H)$$

or in the tensor symbolic form

$$Mi = K_{ij}H_j, \qquad (1.1)$$

where $K_{ij} = K_{ji}$; $i,j = 1, 2, 3$; M_i is the component of the induced magnetization in the direction i, H is the component of the magnetic field in the direction j, K_{ij} is the symmetric tensor of the second order, expressing the magnetic susceptibility, which can also be expressed as a symmetric matrix:

$$K_{ij} = \begin{pmatrix} K_{11} & K_{12} & K_{13} \\ K_{12} & K_{22} & K_{23} \\ K_{31} & K_{32} & K_{33} \end{pmatrix}, \qquad (1.2)$$

where $K_{12} = K_{21}$, $K_{23} = K_{32}$, and $K_{31} = K_{13}$. To completely describe the magnetic susceptibility ellipsoid, a minimum of six independent elements must be determined.

If a sample of sediments is placed in a homogeneous magnetic field, the direction of which is denoted by n, the induced magnetic polarization is given by Eq. (1.1), i.e., in the case of a magnetically anisotropic sample its direction is different from that of the external field. Both directions agree only if the field is inserted in the principal direction of magnetic anisotropy. A system of measured values is used to find these principal directions and determine the values of the magnetic susceptibility along these directions. In the case of a magnetically isotropic sample, K_{ij} ($i \neq j$) is zero and $K_{11} = K_{22} = K_{33}$, so that the direction of the induced magnetic polarization agrees with the direction n.

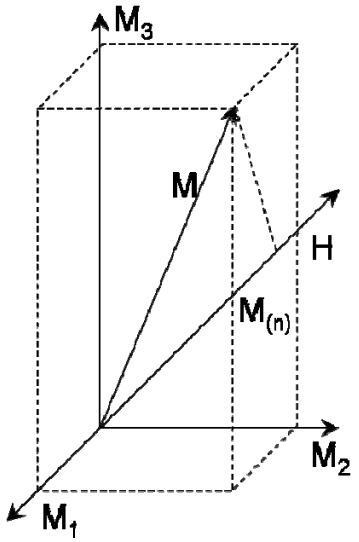

Figure 1.6 Scheme of directional magnetic susceptibility: magnetic field (H) and magnetization (M).

I express the components of the external field H_j by means of the direction cosines (n), denoting the intensity of the external field H_0, so that instead of Eq. (1.1), we have

$$(M) = H_0(K)(n), \qquad (1.3)$$

where the parentheses denote matrices. The components K^x derived from Eq. (1.3),

$$(K^x) = (M)/H_0 = (K)(n), \qquad (1.4)$$

express the magnetic susceptibility. With measuring equipment it is possible to record the value of the magnetic susceptibility in the direction (n) of the external field so that we are measuring a value corresponding only to the projection of the vector of magnetic polarization in the direction n (Figure 1.6).

The magnetic susceptibility, measured by direction cosines n_1, n_2, n_3, will be called the directional magnetic susceptibility, and is given by the relation

$$\kappa = K\,(n)/H_0 = (n)(K)(n), \qquad (1.5)$$

where

$$(n) = (n_1, n_2, n_3),\ (K) = K_{ij} = \begin{pmatrix} K_{11} & K_{12} & K_{13} \\ K_{12} & K_{22} & K_{23} \\ K_{31} & K_{32} & K_{33} \end{pmatrix},\ (n) = \begin{pmatrix} n_1 \\ n_2 \\ n_3 \end{pmatrix}.$$

When choosing the directions we try to keep the relation for the directional magnetic susceptibility simple and the measurements in the chosen direction easily realizable.

An example of a suitable system of measurement is shown in Figure 1.7, where the directional cosines of the AMS measurements have the following values:

$A_1(1, 0, 0)$, $A_4(0, \frac{1}{\sqrt{2}}, \frac{1}{\sqrt{2}})$, $A_7(0, -\frac{1}{\sqrt{2}}, \frac{1}{\sqrt{2}})$,

$A_2(0, 1, 0)$, $A_5(\frac{1}{\sqrt{2}}, 0, \frac{1}{\sqrt{2}})$, $A_8(-\frac{1}{\sqrt{2}}, 0, \frac{1}{\sqrt{2}})$,

$A_3(0, 0, 1)$, $A_6(\frac{1}{\sqrt{2}}, \frac{1}{\sqrt{2}}, 0)$, $A_9(-\frac{1}{\sqrt{2}}, \frac{1}{\sqrt{2}}, 0)$.

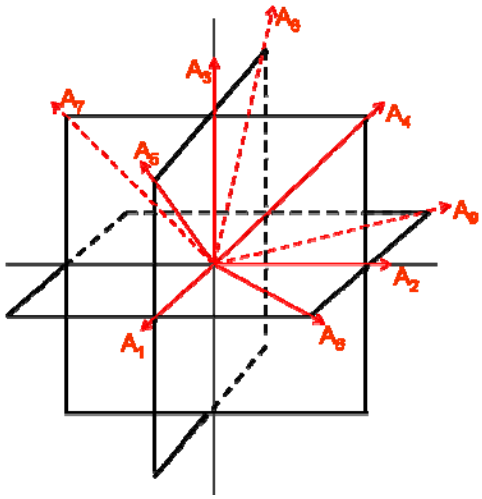

Figure 1.7 Measurement directions (A1…A9 are measurements of AMS values from suitable directions) (modified from Janák (1965).

Figure 1.7 is an example of measurements from A1 to A9, but 6, 15, 18 or even more measurements could be made. During measurements of the anisotropy of magnetic susceptibility of oriented samples using the KLY-3S Kappabridge magnetometer described in chapter 2, the specimen slowly rotates about three perpendicular axes. The magnetic susceptibility differences are measured during specimen spinning (64 measurements during one spin, 192 measurements in total) which results in a very sensitive determination of the magnetically anisotropic component of the magnetic susceptibility tensor, profiting from measurement in the lowest possible and therefore most sensitive range.

b. Methods of Determining the Magnetic Anisotropy Tensor

With the matrix tensor representations, it must be remembered that the tensor's values in Eq. (1.3) depend on the observed measurements from the coordinate frame. The remaining three diagonal values are called the principal values of the magnetic susceptibility K_1, K_2, and K_3 (or K_{max}, K_{int}, and K_{min}). For a magnetically isotropic material, the off-diagonal components are equal to zero. It is necessary to describe the orientation of the principal axes with respect to the original coordinate frame axes by the three remaining numbers. A 3D elliptical object can represent the value of the magnetic susceptibility in any direction.

When measuring the sample, one places it in a variety of orientations in a uniform magnetic field H. The sample will get an induced magnetization M, but as noted M is not generally parallel with H and the instrument measures only the projection of M in the direction of the external field. So, the task is to make sufficient measurements in a variety of directions to get a series of corresponding directional magnetic susceptibilities, and then to back-calculate to obtain the full magnetic susceptibility tensor of Eq. (1.3) from these observations.

As the magnetic anisotropy tensor contains six unknown coefficients, six independent measurements are required to determine the magnetic anisotropy tensor. K_{ij} can be calculated from the directional magnetic susceptibilities when the values of the directional magnetic susceptibilities $\kappa_1 \ldots \kappa_9$ are determined:

$$\begin{pmatrix} K_{23} \\ K_{13} \\ K_{12} \end{pmatrix} = \begin{pmatrix} 0 & -1/2 & -1/2 & -1 & 0 & 0 \\ -1/2 & 0 & -1/2 & 0 & 1 & 0 \\ -1/2 & -1/2 & 0 & 0 & 0 & 1 \end{pmatrix} \begin{pmatrix} \kappa_1 \\ \kappa_2 \\ \kappa_3 \\ \kappa_4 \\ \kappa_5 \\ \kappa_6 \end{pmatrix}. \qquad (1.6)$$

An estimate of the best fit of the magnetic susceptibility ellipsoid as well as the magnitude and direction of the principal axes can be obtained using the least squares method. Details of the calculation can be found in *Girdler* (1961) and Janák (1965). The final equation giving the six coefficients K_{ij} is:

$$\begin{pmatrix} K_{11} \\ K_{22} \\ K_{33} \\ K_{23} \\ K_{31} \\ K_{12} \end{pmatrix} = \frac{1}{18} \begin{pmatrix} 10 & -2 & -2 & 4 & 4 & -2 & 4 & 4 & 2 \\ -2 & 10 & -2 & 4 & -2 & 4 & 4 & -2 & 4 \\ -2 & -2 & 10 & -2 & 4 & 4 & -2 & 4 & -9 \\ 0 & 0 & 0 & 0 & 0 & 9 & 0 & 0 & 0 \\ 0 & 0 & 0 & 0 & 9 & 0 & 0 & -9 & 0 \\ 0 & 0 & 0 & 9 & 0 & 0 & -9 & 0 & 0 \end{pmatrix} \begin{pmatrix} \kappa_1 \\ \kappa_2 \\ \kappa_3 \\ \kappa_4 \\ \kappa_5 \\ \kappa_6 \\ \kappa_7 \\ \kappa_8 \\ \kappa_9 \end{pmatrix}. \qquad (1.7)$$

The directions of the principal axes can be calculated by:

$$\tan\theta = \frac{n_2}{n_1}, \qquad (1.8)$$

$$\sin\varphi = n_3, \qquad (1.9)$$

where n_i are the directional cosines of the principal axes. The directional cosines are converted to the (θ, φ) notation where θ is the angle of declination in degrees measured clockwise from $OA1$ and φ is the angle of inclination with reference to the $A1$–$A2$ plane (Figure 1.7). According to Janák (1965), the average coefficient deviation of error is less than 1%.

1.2.2 AMS Parameters and Their Illustration

A variety of parameters have been defined to quantify the magnitude of magnetic anisotropy and to describe the shape of the magnetic susceptibility ellipsoid. The low-field AMS is usually determined after measuring the magnetic susceptibility of a rock specimen along different directions. This enables one to calculate the AMS tensor, which can be represented by an ellipsoid with maximum (K_{max} or K_1), intermediate (K_{int} or K_2), and minimum (K_{min} or K_3) magnetic susceptibility axes (Tarling and Hrouda, 1993).

An arithmetical or geometrical mean of the principal axes is used in most publications. If we substitute the ellipsoid of magnetic anisotropy by a sphere of the same volume and define the mean magnetic susceptibility by means of the radius of this sphere, then the geometrical mean of the principal axes is given by

$$K_{geo\text{-}mean} = \sqrt[3]{K_1 \cdot K_2 \cdot K_3}\ . \qquad (1.10)$$

In another approach the surfaces of the ellipsoid and the sphere are compared. The arithmetical mean magnetic susceptibility of a single specimen is equivalent to the mean value of the integral of the directional magnetic susceptibility over the whole specimen (Nagata, 1961; Janák, 1965), given by

$$K = \frac{K_{max} + K_{int} + K_{min}}{3}\ . \qquad (1.11)$$

The arithmetical mean magnetic susceptibility of a sample group K_{Mean} is obtained as follows:

$$K_{Mean} = \frac{\sum K_i}{n};\ n = 1, 2, 3, \ldots i. \qquad (1.12)$$

Lineation (Balsley and Buddington, 1960) and foliation (Stacey et al., 1960) are earlier parameters which were defined in terms of ratios between principal magnetic susceptibility values. The eccentricity of an AMS ellipsoid can be expressed as:

$$\text{Lineation (L)} = \frac{K_{max}}{K_{int}}, \tag{1.13}$$

$$\text{Foliation (F)} = \frac{K_{int}}{K_{min}}. \tag{1.14}$$

For sediments, variations in lineation are usually much smaller than variations in foliation, i.e., the majority of the anisotropic magnetic grains exhibit oblate fabrics (disk shape) indicating that magnetic anisotropy is determined by foliation (Figure 1.8).

The magnitude of magnetic anisotropy is also based on the ratio of maximum to minimum magnetic susceptibilities, known as the magnetic anisotropy degree (Nagata, 1961):

$$\text{P} = \frac{K_{max}}{K_{min}}. \tag{1.15}$$

The shape parameter T of the AMS is defined as:

$$\text{T} = \frac{2\eta_2 - \eta_1 - \eta_3}{\eta_1 - \eta_3}, \tag{1.16}$$

where η_1, η_2 and η_3 are $\ln(K_{max})$, $\ln(K_{int})$, and $\ln(K_{min})$, respectively.

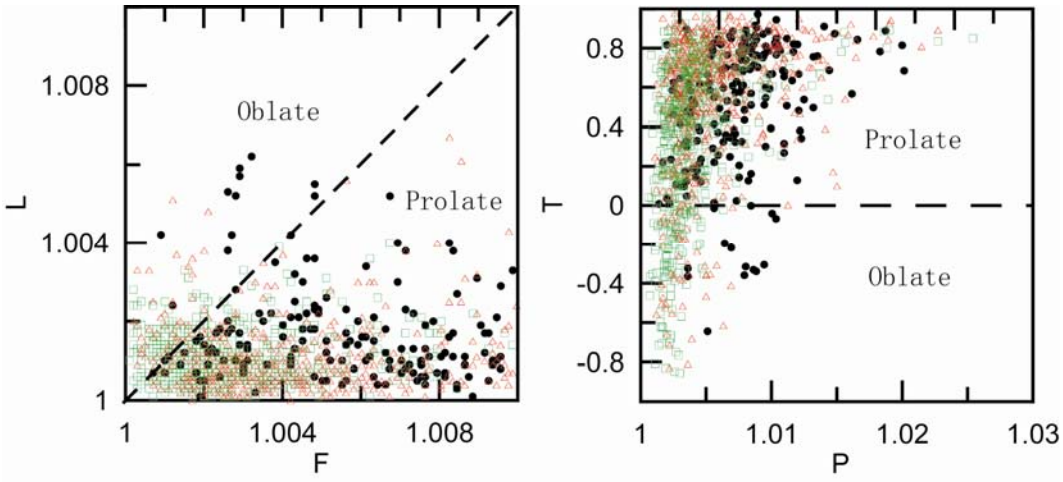

Figure 1.8 Basic parameters of AMS (left: lineation (L) vs. foliation (F); right: shape parameter (T) vs. anisotropy degree (P).

According to Tarling and Hrouda (1993), the predominantly oblate fabric is usually tilted by 0–20º away from the bedding plane, even under a strong current. Previous studies (Lagroix et al., 2004; Zhu et al., 2004), accepted a vertical minimum Inc-K_{min} of 70º because even a strong current cannot cause it to be less than 70º.

1.2.3 Dynamic Models of Theoretical Depositional Fabrics

The initial fabric of a rock specimen is largely determined by gravitational and dynamic forces and is controlled by the size, shape, and mass of the detrital grains and the velocity of the medium in which they are transported. An additional force on the magnetic minerals is caused by the Earth's magnetic field – although this is weak, affecting only small grain sizes (< 1–2 μm), and becomes important mainly during postdepositional processes.

Interpretation of the measurements is not as straightforward as making AMS measurements. In order to build a geological model it is essential to establish the

material composition, the size of magnetic grains, and the physical relationships between mineral grains when interpreting a magnetic fabric.

Wind tunnel experiments showed that eolian deposition is analogous to deposition under hydrodynamic conditions (Wu et al., 1998). When deposition occurs grain by grain in still water, gravitational settling is the only significant force and causes all platy grains to lie in the plane of the depositional surface (bedding plane). The majority of rod-like grains will also lie with their longer axes aligned randomly within the bedding plane. This gives rise to a simple, strongly oblate fabric that is confined to the bedding plane, with the result that the minimum shape axes are all perpendicular to it (Figure 1.9). This type of fabric is only slightly modified by the slope of the horizontal surface on which deposition is taking place.

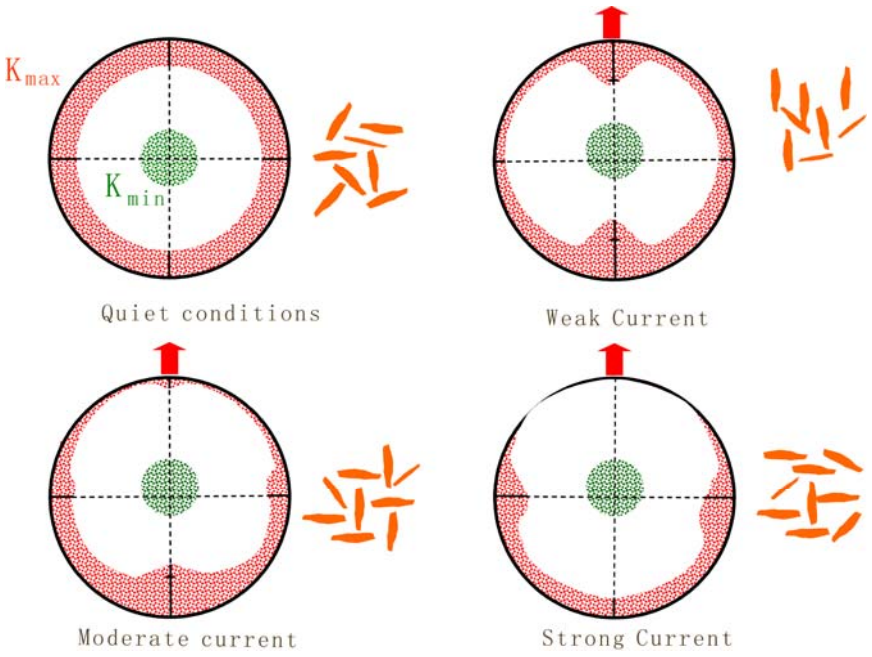

Figure 1.9 Theoretical depositional fabric in the presence of water currents (revised from Tarling and Hrouda (1993)). The red and green areas in the diagrams represent the orientations of K_{max} and K_{min}, respectively. The orange colored grains to the right of each stereonet illustrate the preferred alignment of the rod-like magnetic particles in the horizontal plane.

Quiet conditions: on a horizontal surface, gravity is the only force, so the fabric of the sample which includes all the rod-like magnetic grains is entirely foliated (oblate) and has no superimposed lineation.

Weak water current aligns the long axes of prolate grains, producing a lineation parallel to the direction of the flow. The imbrication is generally less than 10°, so the oblate fabric is still essentially confined to the bedding plane.

Strong water current increases the angle of imbrication so that the predominantly oblate fabric is tilted by 5–20° away from the bedding plane. However, the more prolate grains are now more stable if they lie with their long axes perpendicular to the flow direction (Granar, 1958), i.e., at right-angles to the direction of imbrication and, therefore, some 90° from the lineations associated with lower-velocity conditions.

The stronger the water current, the higher the tendency of prolate particles to become oriented perpendicular to the current flow.

1.3 Magnetic Remnance and Magnetostratigraphy

Sediments acquire a remanent magnetization through a variety of mechanisms collectively called natural remanent magnetization (NRM). NRM does not include laboratory-induced magnetizations. Often NRM contains more than one component. The component acquired during sediment formation is called primary NRM. Secondary NRM components are acquired after sediment formation and can disturb or even change the primary NRM. The total NRM is expressed as:

NRM = primary NRM + secondary NRM.

The three most common natural remanent magnetizations are (1) thermo-remanent magnetization, acquired during cooling from high temperature; (2) chemical-remanent magnetization, acquired by growth of ferromagnetic grains below the Curie temperature; and (3) detrital remanent magnetization, formed during accumulation of sediments controlled by detrital ferromagnetic minerals. Viscous remanent magnetism (VRM) is remanent magnetization that is gradually acquired during long-term exposure to weak magnetic fields. Natural VRM is a secondary magnetization caused by the overprint of ancient geomagnetic fields and usually is undesirable noise.

Secondary NRM can be caused by chemical changes in ferromagnetic minerals or any reheating of the sediment or rock (metamorphism). Processes of acquisition of secondary NRM should be examined to recognize (1) coexistence of primary and secondary NRM in the same rock, (2) how many components of NRM can be determined, and (3) how limited demagnetization procedures could preferentially remove secondary NRM, allowing a separation of primary NRM.

Postdepositional processes such as bioturbation, compaction, and chemical processes can alter original detrital ferromagnetic minerals with attendant effects on the paleomagnetic record. These processes result in many uncertainties in the accuracy of paleomagnetic recordings in sedimentary rocks. The combination of depositional and postdepositional magnetization processes is referred to as detrital remanent magnetism (DRM). Magnetite and hematite are the dominant detrital ferromagnetic minerals in most sediments.

Earth's magnetic field reversed many times during geologic history. A record of these reversals is preserved as rocks are laid down in layers over time, and can be interpreted by measuring the remnant magnetic properties of sedimentary layers. Magnetostratigraphy is a chronostratigraphic technique used to date sedimentary and volcanic sequences. Black and white magnetostratigraphic columns of rocks indicate normal polarity (parallel to the present magnetic field) and reversed polarity (antiparallel to the present magnetic field), respectively. When measurable changes in polarity of the preserved geomagnetic field vary in sedimentary sequences they can provide a robust stratigraphic correlation framework. The direction of the remnant magnetic polarity recorded in the stratigraphic sequence can be used as the basis for the subdivision of the sequence into units characterized by their magnetic polarity. Direction variations of the remanent magnetization show that such reversals of polarity have taken place many times during geologic history due to reversals in polarity of the Earth's magnetic field.

1.4 Paleomagnetism and Tectonic Reconstructions

The study of remnant magnetic properties in rocks, paleomagnetism, has been used to verify and develop continental drift theory since the 1950s and helped drive the earth science "revolution" in the 1960s. Paleomagnetic studies led to the transformation of the "plate tectonics theory" that measures the movement of continental fragments. Paleomagnetic theory is now applied to identify movement of the main tectonic plates or local scale terrane (blocks), to define complex and widespread strains in orogenic belts, and as a quantitative indicator of translations in paleolatitude and ancient vertical axis rotations of lithospheric blocks.

1.5 Major Goals of the Thesis

The three major goals of the thesis are listed below with a description of the methods I have used to achieve them.

1. The Chinese Loess Plateau has the thickest and oldest eolian (eroded, transported, deposited by wind) sediments on Earth. It has been considered that the winter monsoon winds are responsible for the orientation of the magnetic and sedimentary grains in the loess and paleosol deposits (Thistlewood and Sun, 1991; Hus, 2003). In order to reconstruct past monsoon routes, I investigated the ellipsoid mean orientations of the AMS in three geological sections along the east-west transect in the Chinese Loess Plateau. The AMS ellipsoid orientations mirror the grains' imbrications and can be used to reconstruct the wind's preferred direction. This way paleomonsoon routes were assessed during the last 130 kys.

2. The Eocene-Oligocene transition (EOT) of the climate at ~34 Ma marks a period of Antarctic ice growth and a major climatic transformation from early Cenozoic greenhouse conditions toward the glaciated conditions attributed to the present day. The transition is characterized by an increase in deep-sea benthic foraminiferal oxygen isotope $\delta^{18}O$ values. Timing of the EOT on the continent, however, could vary from the EOT timing in the ocean. For example, the North American EOT may lag the marine transition by ~0.4 Myr (Zanazzi et al., 2007). A stratigraphic section that contains both late Eocene and early Oligocene faunas has not been yet described in Asia and therefore the timing of the EOT in Asia is debatable. I studied sections from the Junggar Basin, China, in order to reconstruct the timing of the EOT in Asia. I aimed to define an age interval for the

EOT in the studied section and to compare it with the sections from the same time intervals in Europe and Mongolia in order to identify a linkage to faunal evolution from perissodactyl-dominant to rodents and lagomorphs (a warm subtropical climate changing to a cool and dry condition) during the EOT.

3. Paleoreconstructions of the Asian continent and various models of crustal deformations during Paleogene and Neogene periods remain controversial because of the rarity of well-dated sediments and igneous rock. I obtained the first paleomagnetic result from the well-dated sediments at two stratigraphic sections in the north Junggar basin in order to reconstruct a paleoposition of the Asian tectonic blocks.

Publications to which I have contributed and that are associated with my Ph.D. program are listed below. The thesis is based on the first three publications. The forth manuscript was also prepared during my Ph.D. work. The rest of the publications are related to the Ph.D. research in paleomagnetism and petromagnetism of Cenozoic sediments that I carried out in China.

1. ***R. Zhang***, V. A. Kravchinsky, R. Zhu, and L. Yue. Paleomonsoon route reconstruction along a W–E transect in the Chinese Loess Plateau using the anisotropy of magnetic susceptibility: summer monsoon model. ***Earth and Planetary Science Letters,*** 2010, 299, 436–446.
2. ***R. Zhang***, V. A. Kravchinsky and L. Yue. Reconstruction of the Missing Link between Global Cooling and Mammalian Transformation across the Eocene-Oligocene Boundary in the Continental Interior of Asia. *Submitted to* ***Palaeogeography Palaeoclimatology Palaeoecology***, 2011.

3. ***R. Zhang***, V. A. Kravchinsky, D. Blanco and L. Yue. New paleomagnetic poles for the northern Junggar Basin, northwest China, about 40 and 20 Ma: Evidence of intracontinental shortening between Junggar and Europe after 20 Ma. *Submitted to* ***Geophysical Journal International***, 2011.

4. V. A. Kravchinsky, D. R. Eccles, ***R. Zhang*** and M. Cannon. Paleomagnetic dating of the Northern Alberta kimberlites. ***Canadian Journal of Earth Sciences***, 2009, 46, 231–245.

5. R. Zhu, ***R. Zhang***, C. Deng, Y. Pan. Q. Liu, and Y. Sun. Are Chinese loess deposits essentially continuous? ***Geophysical Research Letters***, 2007, 34, L17306, doi: 10.1029/2007GL030591.

6. C. Deng, R. Zhu, ***R. Zhang***, H. Ao, Y. Pan. Timing of the Nihewan Formation and faunas. ***Quaternary Research***, 2008, 69, 77–90.

7. ***R. Zhang***, L.Yue, J. Wang. Magnetostratigraphic dating of mammalian fossils in Junggar Basin, northwest China. ***Chinese Science Bulletin***, 2007, 52, 1526–1531.

8. C. Deng, Q. Wei, R. Zhu , H. Wang , ***R. Zhang***, H. Ao, L. Chang, Y. Pan. Magnetostratigraphic age of the Xiantai Paleolithic site in the Nihewan Basin and implications for early human colonization of Northeast Asia. ***Earth and Planetary Science Letters,*** 2006, 244, 336–348.

9. R. Zhu, Q. Liu, Y. Pan, C. Deng, ***R. Zhang,*** and X. Wang. No apparent lock-in depth of the Laschamp geomagnetic excursion: Evidence from the Malan loess. ***Science in China Series D: Earth Sciences***, 2006, 49, 960–967. DOI: 10.1007/s11430-006-0960-x.

Bibliography

Balsey, J. R., and A. F. Buddington, 1960. Magnetic susceptibility anisotropy and fabric of some adirondack granites and orthogneisses, Am. J. Sci., 258(A), 6–20.

Borradaile, G., 1988. Magnetic susceptibility, petrofabrics and strain, Tectonphysics, 156, 1–20.

Borradaile, G., 1991. Correlation of strain with anisotropy of magnetic susceptibility (ams), Pure and Applied Geophysics, 135, 15–29.

Borradaile, G., 2001. Magnetic fabrics and petrofabrics: their orientation distributions and anisotropies, J. Struct. Geol., 23, 1581–1596.

Borradaile, G., and D. Gauthier, 2003. Interpreting anomalous magnetic fabrics in ophiolite dike, J. Struct. Geol., 25, 171–182, 2003.

Borradaile, G., and B. Henry, 1997. Tectonic applications of magnetic susceptibility and its anisotropy, Earth Sci. Rev., 42, 49–93.

Borradaile, G., and F. Lagroix, 2001. Magnetic fabrics reveal upper mantle flow fabrics in the troodos ophiolite complex, cyprus, J. Struct. Geol., 23, 1299–1317.

Borradaile, G. J., and M. Stupavsky, 1995. Anisotropy of magnetic susceptibility: Measurement schemes, Geophysical Research Letters, 22, 1957–1960.

Borradaile, G. J.,W. Keeler, C. Alford, and P. Sarvas, 1987. Anisotropy of magnetic susceptibility of some metamorphic minerials, Physics of the Earth and Planetary Interiors, 48, 161–166.

Dunlop, D., and O. Őzdemir, 1997. Rock magnetism: Fundamentals and frontiers, Cambridge University Press.

Dunlop, D., and M. Prévot, 1982. Magnetic properties and opaque mineralogy of drilled submarine intrusive rocks, Geophys. J. Roy. Astron. Soc., 69, 763–802.

Girdler, R.W., 1961. The measurement and computation of anisotropy of magnetic susceptibility of rocks, Geophys. J. R. Astr. Soc., 5, 34–44.

Granar, L., 1958. Magnetic measurements on Swedish varved sediments, Arkiv. F. Geofysik, 3, 1–40.

Hanna, W. F., 1977. Weak-field magnetic susceptibility anisotropy and its dynamic measurement, U. S. Geol. Surv. Bull., 1418, 1–73.

Hrouda, F., 1982. Magnetic anisotropy of rocks and its application in geology and geophysics, Geophys. Surv., 5, 37–82.

Hus, J. J, 2003. The magnetic fabric of some loess/palaeosol deposits. Physics and Chemistry of the Earth 28, 689–699.

Ising, E., 1942. On the magnetic properties of varved clay, Arkiv Astron. Fysik, 29 A(5), 1–37.

Jackson, M., 1991. Anisotropy of magnetic remanence: a brief review of mineralogical sources, physical origins and geological applications, and comparison with susceptibility anisotropy, Pure Appl. Geophys., 136, 1–28.

Janák, F., 1965. Determination of anisotropy of magnetic susceptibility of rocks, Studia geoph. et geod., 9, 290–300.

Jelinek, V., 1977. The statistical theory of measuring anisotropy of magnetic susceptibility of rocks and its application, Brno, Geofyzika, pp. 1–88.

Jelinek, V., 1978. Statistical processing of anisotropy of magnetic susceptibility measured on groups of specimens, Studia geoph. et geod., 22, 50–62.

Jelinek, V., 1981. Characterization of the magnetic fabric of rocks, Tectonophysics, 79, 63–67.

Lagroix, F., and G. Borradaile, 2000. Magnetic fabric interpretation complicated by inclusions in mafic silicates, Tectonophysics, 325, 207–225.

Nagata, T., Rock magnetism, 2 ed., 1961. Maruzen, Tokyo.

Owens, W. H., 1974. Mathematical model studies on factors affecting the magnetic anisotropy of deformed rocks, Tectonphysics, 24, 115–131.

Rochette, P., M. Jackson, and C. Aubourg, 1992. Rock magnetism and the interpretation of anisotropy of magnetic susceptibility, Rev. Geophys., 30, 209–226.

Rees, A. I., 1965. The use of anisotropy of magnetic susceptibility in the estimation of sedimentary fabric. Sedimentology 4, 257– 271.

Rees, A. I., Wooddall, W. A., 1975. The magnetic fabric of some laboratory deposited sediments. Earth and Planetary Science Letters 25, 121–130.

Stacey, F. D., 1960. Magnetic anisotropy of igneous rocks, J. Geophys. Res., 65, 2429–2442.

Stephenson, A., 1994. Distribution anisotropy: two simple models for magnetic lineation and foliation, Phys. Earth Planet. Inter., 82, 49–54.

Tarling, D. H., 1983. Palaeomagnetism, Chapman and Hall, London.

Tarling, D. H., and F. Hrouda, 1993. The Magnetic Anisotropy of Rocks, Chapman and Hall, London.

Thistlewood, L., Sun, J., 1991. A paleomagnetic and mineral magnetic study of the loess sequence at Liujiapo, X'ian, China. Journal of Quaternary Sciences 6, 13–26.

Zhu, R., Zhang, R., Deng, C., Pan, Y., Liu, Q., Sun, Y. 2007. Are Chinese loess deposits essentially continuous? Geophysical Research Letters 34, L17306, doi: 10.1029/2007GL030591.

Chapter 2*

Paleomonsoon route reconstruction along a W–E transect in the Chinese Loess Plateau using the anisotropy of magnetic susceptibility: summer monsoon model

2.1 Introduction

Half a century ago AMS measurements were proposed as a tool for the rapid quantified description of rock fabrics in a wide range of rocks (Graham, 1954). Anisotropy of magnetic susceptibility (AMS) measure within a specimen is a variation of magnetic susceptibility in different orientations, described by a 3D ellipsoid that has maximum, intermediate, and minimum AMS axes. The anisotropy is determined by both the preferred crystallographic and dimensional (or shape) orientation of grains in the sediment. Superposition of ferri-, para-, and diamagnetic grain properties causes the total AMS value. The anisotropy of low-field magnetic susceptibility quantitatively measures the average preferred mineral orientation and is thus a rapid and precise tool for determining the fabric of rocks and sediments. AMS is a sensitive indicator of the texture of magnetic fabric sediment on the sediment perpetrated by wind. Consequently, wind directions can be intimated by studying the AMS of sediments deposited over time.

* A version of this chapter has been published in the journal of Earth and Planetary Science Letters, 2010, 299, 436–446.

Heller et al. (1987) were the first to measure AMS in loess and concluded that Chinese loess had a uniform magnetic fabric and sedimentation rate through time in the Luochuan section. Further, Liu et al. (1988) demonstrated that AMS parameters could be used to evaluate the water re-working of wind-blown sediments. Thistlewood and Sun (1991) investigated a loess cross-section near X'ian in the southeast part of the Chinese Loess Plateau. Their study demonstrated that in both loess and paleosol samples the minimum axes of the AMS ellipsoids were clustered vertically and the maximum axes were gathered along the WNW–ESE direction.

Tarling and Hrouda (1993) reviewed the effects of wind and water currents on the magnetic grain fabric and AMS orientation and noticed an AMS dependence on wind/water current strength and direction. Hydrodynamic experiments have shown that gravitational forces are usually dominant and give a strong oblate fabric within the bedding plane, whereas elongated particles produce a lineation parallel to the direction of transport (Rees and Woodall, 1975; Tarling and Hrouda, 1993). Platy minerals are usually imbricated by water currents or by wind and the minimum AMS axes tilt toward the flow direction. Stronger water currents or wind increase the tilt of the grains and can rotate and roll them causing prolate grains to align perpendicular to the current flow (Granar, 1958). Figure 2.1 illustrates the dependence of the AMS ellipsoid orientation on wind/water current direction.

Lagroix and Banerjee (2002, 2004a, 2004b) confirmed that the magnetic susceptibility of magnetite and maghemite in loess-paleosol sequences is three to four times greater than that of all other minerals and therefore AMS defines the magnetic lineation of the magnetite and maghemite grains. They also found that

AMS measured in the central Alaska loess mirrors the overall mean paleowind directions for the same time intervals. Minor variance in the AMS orientation for different locations could denote local wind deviations.

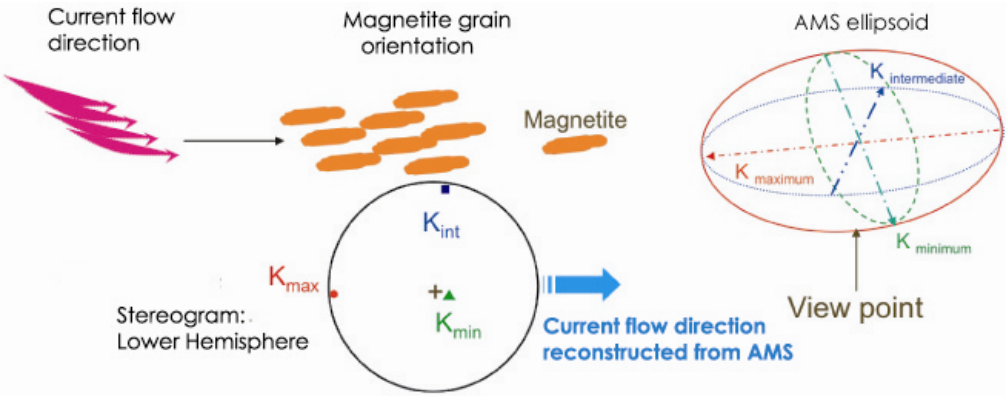

Figure 2.1 Illustration of the mechanism responsible for orientation of the sedimentary and magnetite grains in sediment transported by strong water currents or wind. Anisotropy of magnetic susceptibility (AMS) can be illustrated with the so-called AMS ellipsoid that has a maximum susceptibility axis K_{max} along the longest grain axis. The intermediate K_{int} and minimum K_{min} susceptibility axes are orthogonal to the maximum K_{max} and define the oblateness of the AMS ellipsoid and consequently the magnetic grain. For illustrative purposes we use the lower hemisphere stereonet projection of the three-dimensional ellipsoid to define the current flow direction.

Zhu et al. (2004) demonstrated that three magnetic minerals – primary magnetite, maghemite, and hematite – are the major carriers of the MS signal in the Chinese loess. Magnetic lineation derived from the AMS ellipsoid gathers along NE–SW and NW–SE directions during glacial and interglacial intervals in the area southeast of the Liupan Mountains. Zhu et al. (2004) reported that wind directions correspond to dust carried by the NE winter monsoon and moisture transported by the SE summer monsoon. Such NE direction is different from the commonly recognized winter monsoon course from the NW and caused by the local deviation due to Liupan Mountains. The authors noted that it is still not quite clear which of these two monsoons played a more important role in the

imbrication of the magnetic grains. To further examine the role of the winter and summer monsoons in the AMS signal acquisition and to reconstruct the paleomonsoon routes, we investigated 1204 samples from three sections along an east-west transect in the Chinese Loess Plateau. The samples span the last 130 kyrs.

2.2 Sampling and Methods

We sampled three sections (Baicaoyuan (36.28ºN, 105.21ºE), Xifeng (35.76ºN, 107.7ºE), and Yichuan (36.1ºN, 110.14ºE)) located in the western and central parts of the Chinese Loess Plateau (Figure 2.2).

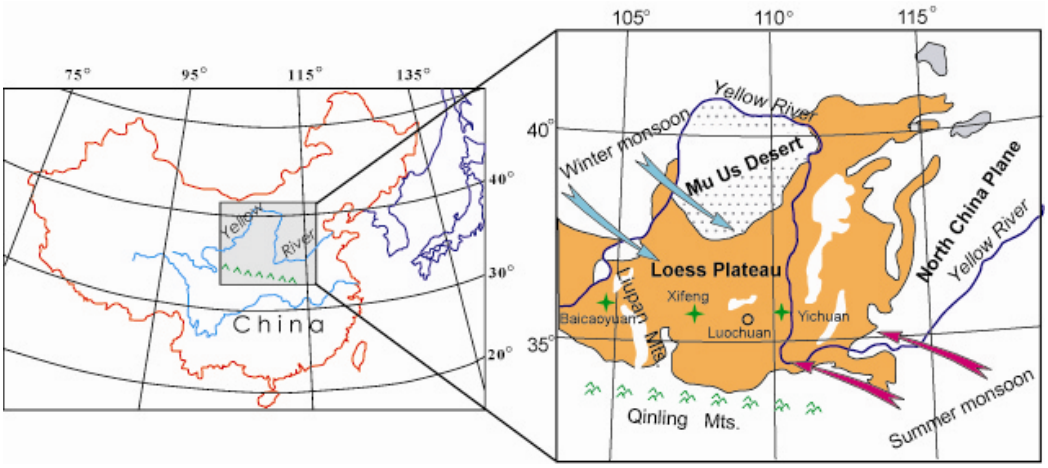

Figure 2.2 Schematic map of the Chinese Loess Plateau showing the sampling localities discussed in the text. Dominant winter and summer monsoon directions of the present day are shown after An (2000), An et al. (2001), Porter (2001).

The dry winter monsoon brings dust from the northwest to the study area. The moist summer monsoon approaches from the southwest and brings rain. The Liupan Mountains are a natural barrier to the summer monsoon and stop some of the moisture from penetrating further west into the Baicaoyuan area. The mountain ridges protect the area from the direct influence of the summer monsoon

and force the wind to change its route. These phenomena are reflected in a lower several year mean temperature (8.5ºC) and several year mean precipitation (350 mm) in Baicaoyuan compared to Xifeng (9.7ºC, 550 mm) and Yichuan (9.9ºC, 577 mm) (Banerjee et al., 1993; Wang et al., 1997). The study areas correspond to the semi–humid (Xifeng and Yichuan) and semi–arid (Baicaoyuan) climate.

Continuity of the eolian sedimentary sequences is highly dependent on the topography. To obtain a higher resolution AMS record we chose the most continuous and thick sections on the plateau. After removing a half-meter thick coverage along a well-exposed gully wall, we collected large blocks unaffected by weathering. The hand-cut blocks of ~10 cm width and ~20-30 cm height were orientated in-situ using a magnetic compass. Geomagnetic azimuth corrections were applied to every sample. Three smaller size cubic samples (8 cm^3) were cut from the same depth in the laboratory at every 2.5 cm depth interval. We measured AMS for all three oriented cubes for the same pilot depth intervals spread through whole section (506 samples). The discrepancy in the AMS result in the all three samples was negligibly small (a standard error was less than 1% for 99% of the depth intervals) and we continued measurements of one cube per one depth interval for the rest of the samples.

The magnetic mineral content in the Baicaoyuan section and the paleomagnetism of the Xifeng and Yichuan sections have been recently discussed in Deng (2008) and Zhu et al. (2007). Magnetite is the dominant magnetic mineral in both loess and paleosol (Figure 2.3). The AMS, however, has never been studied at these sites. We obtained 186 samples at 10 cm intervals in the Baicaoyuan section and 523 and 496 samples from the Xifeng and Yichuan sections, respectively, at 2.5 cm intervals. The top of the Baicaoyuan section is

denuded in most places and was sampled in ~30 km away from the main section. The sampled stratigraphic intervals comprised the Holocene soil (S_0, in our sections). The S_0 layer was heavily cultivated in all of our study areas and therefore the original AMS had been destroyed. Porter and An (1995) and Zhu et al. (2004) demonstrated that the Malan loess (L_1) corresponds to marine isotope stage (MIS) 2–4 and the interglacial soil (S_1) corresponds to MIS 5. Thicknesses of the sections sampled from Baicaoyuan, Xifeng, and Yichuan sections were 19, 16, and 14 m, respectively.

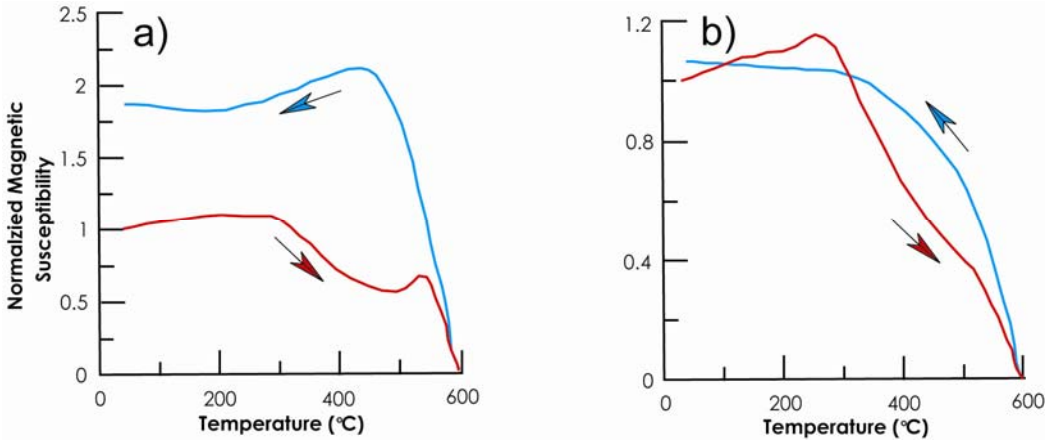

Figure 2.3 Temperature-dependent susceptibility curves (normalized by the initial value) showing heating to different maximum temperatures for a representative loess (a) and paleosol (b) sample. Heating (cooling) curve is red (blue).

The mass-specific low-field magnetic susceptibility (MS) and the AMS of each sample was measured using a KLY-3S Kappabridge (Agico Ltd., Brno) with an automated sample handling system. Each sample was rotated through three orthogonal planes. The susceptibility ellipsoid was calculated by the least-squares method; the anisotropy parameters of lineation (L), foliation (F), degree of anisotropy (P), and shape factor (T) (Jelinek, 1981) were obtained with Anisoft software using the statistical method of Constable and Tauxe (1990).

2.3 Results

In order to construct an age model, we correlated our MS record with the oxygen isotope reference curve from Bassinot et al. (1994) and with the reference Luochuan MS profile from Porter and An (1995) (Figure 2.4). The Luochuan section is situated between two of our sampled sections (Xifeng and Yichuan) and is dated throughout by the thermoluminescence method (TL). To build our first order age model we correlated the MS profiles between sections and with the oxygen isotope curve from Bassinot et al. (1994). Evans and Heller (2003) discussed the necessity and success of this approach. In particular, they demonstrated that paleosols always correspond to the higher MS signals in Chinese loess/paleosol sequences due to higher concentrations of magnetite and maghemite. Our MS values for the modern soil S_0 and the latest paleosol S_1 intervals are always higher than for the loess intervals. Deng et al. (2004) showed that paramagnetic magnetic susceptibility is typically 5–8% of total MS signal in loess, and 2–4% in paleosol. Xie et al. (2009) estimation of paramagnetic effect on total MS is similar. They also concluded that the eolian contribution ~50% in the total MS signal in Chinese loess and ~30% in paleosol. It confirms that major portion of the MS signal in loess and large portion of the signal in paleosol are determined by the ferromagnetic minerals transported by the wind.

In order to adjust our first order age model based on correlation with the oxygen isotope curve (Figure 2.4) we applied a correlation to the reference Luochuan section which has TL dates published by Porter and An (1995). The final results of this correlation and our age model are presented in Table 2.1 The rapid changes in susceptibility values at the L_1/S_0, S_1/L_1, and L_2/S_1 stratigraphic boundaries correlate well with the MIS 2/1 (12.05 kyr), MIS 5/4 (73.91 kyr), and

MIS 6/5 (128 kyr) boundaries. The loess horizon L_1 has higher MS values in the middle part of the profile in Xifeng, Yichuan, and Luochuan sections because of the magnetic signal enhancement caused by the paleosol horizon L_1SS_1 (Figure 2.4). The horizon corresponds to MIS 3. Two warming intervals in MIS 3 (around 29 and 53 ka) are prominent in all cross-sections except the Baicaoyuan. We suppose that dry climate conditions existed in the Baicaoyuan area during MIS 3. Such dry conditions could have been caused by a relatively high rate of Liupan Mountain growth as a result of the continuous penetration of India into the Eurasian continent. The mountains would block the summer monsoon moisture from infiltrating further west into the continent.

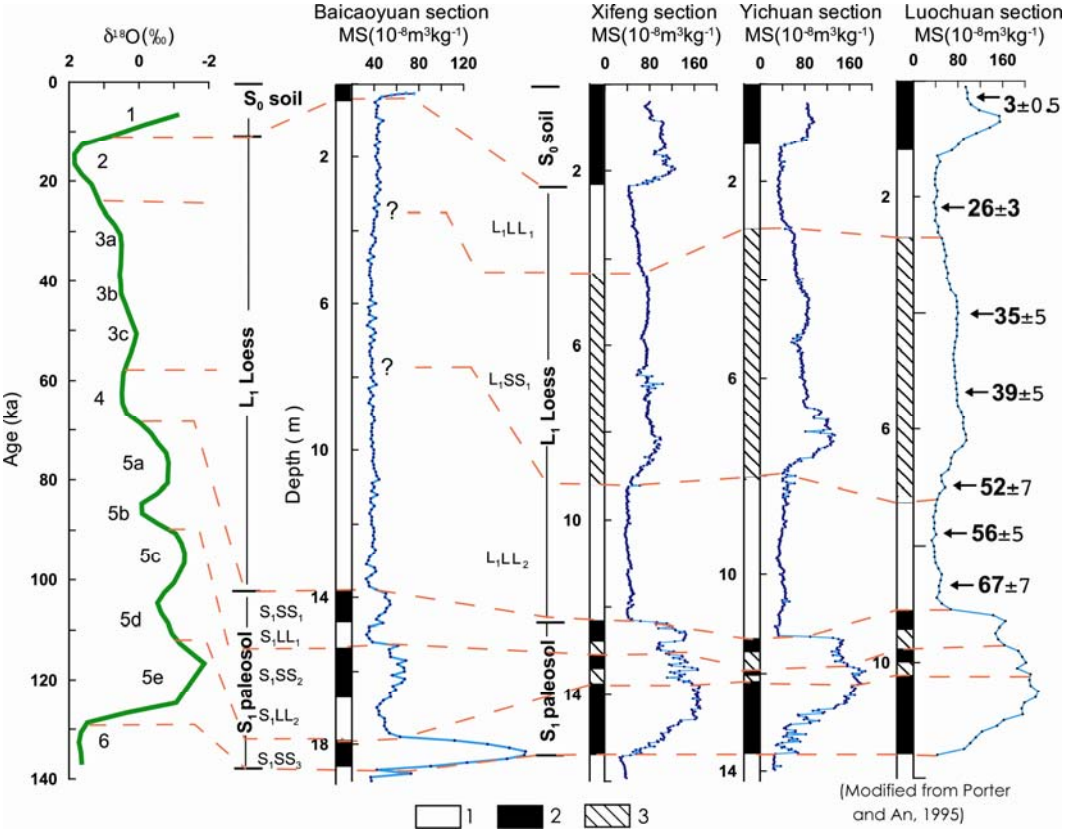

Figure 2.4 Correlation between a marine oxygen isotope δO^{18} reference curve (numbers signify stages), the loess/paleosol stratigraphy, and the low-field magnetic susceptibility in the studied sections. The Luochuan section parameters and TL ages are from Porter and An (1995); the marine oxygen isotope reference curve is from Bassinot et al. (1994). 1 – loess intervals, 2 – paleosol intervals, 3 – underdeveloped paleosol.

Xifeng, Yichuan, and Luochuan had more moisture and the L_1SS_1 horizon is well preserved in these sections. Although the precise time and amplitude of Liupan Mountain growth is difficult to determine, the 2000 m uplift of the Himalayan mountains and Tibet during the Pleistocene epoch is well known (Li, 2006; Rieser et al., 2009).

Table 2.1 Age model for Baicaoyuan, Xifeng, and Yichuan sections.

Age (kyr)	MIS	Depth (m)		
		Baicaoyuan	**Xifeng**	**Yichuan**
12.05	2/1	1.1	2.3	1.23
25.4	3/2	–	4.1	3
59.03	4/3	–	9.2	7.7
73.91	5/4	13.8	12.3	11.3
128	6/5	18.7	15.4	13.7

MIS – Marine Isotope Stage numbers.

The relatively warmer and cooler stages of MIS 5 are well represented in all four sections. For the Baicaoyuan section, however, three subdivided paleosols (S_1SS_1, S_1SS_2, S_1SS_3) and two intrabedded loess units (S_1LL_1, S_1LL_2) are better pronounced inside the MIS 5 pedocomplex (S_1). The Liupan Mountains perhaps had lower elevation than today and did not block all the summer monsoon moisture during MIS 5 allowing a generally more humid climate and soil formation than during MIS 3 and today.

The low field AMS is generally described in the sample by an oriented ellipsoid with maximum (K_{max}), intermediate (K_{int}), and minimum (K_{min}) axes of magnetic susceptibility. Following the technique suggested by Lagroix and Banerjee (2004b) and applied in Zhu et al. (2004), we used epsilon ε_{12} which

represents the half-angle uncertainty of K_{max} in the plane joining K_{max} and K_{int} and ε_{23} which is the half-angle uncertainty of K_{int} in the plane joining K_{int} and K_{min}. In these notations, 1, 2 and 3 are assigned to K_{max}, K_{int} and K_{min}, respectively.

An inverse relationship between ε_{12} (ε_{23}) and the magnetic lineation parameter L (magnetic foliation parameter F) was observed in all sections (Figure 2.5a and 2.5c demonstrates that L (F) decreases as ε_{12} (ε_{23}) increases) due primarily to the increasing importance of random measurement errors for K_{max} (K_{min}) in the lineation (foliation) plane with weak lineations (foliations). Independence between ε_{12} and foliation (Figure 2.5b) reinforces the fact that the lineation and foliation sub fabric could be defined by separate mineral orientation distributions.

The majority of the samples from all three studied localities demonstrate the prevalence of oblate magnetic fabric which is typical for loess (Lagroix and Banerjee, 2004b); nevertheless the presence of prolate grains is evident (Figure 2.5). The majority of the samples satisfies the statistically significant level of $\varepsilon_{12} < 22.5°$ (70.1% for BCY, 86.6% for XF, and 92.3% for YC).

The K_{min} directions are described by the inclination (I - K_{min}) and declination (D - K_{min}) of K_{min} distributed along the vertical axis of the stereonet projection. I - K_{min} is larger than 70^{o} in 87.7%, 78.0%, and 62.2% of our samples from Baicaoyuan, Xifeng, and Yichuan, respectively, corresponding (usually) to an undisturbed (less reworked) loess with an observed oblate fabric.

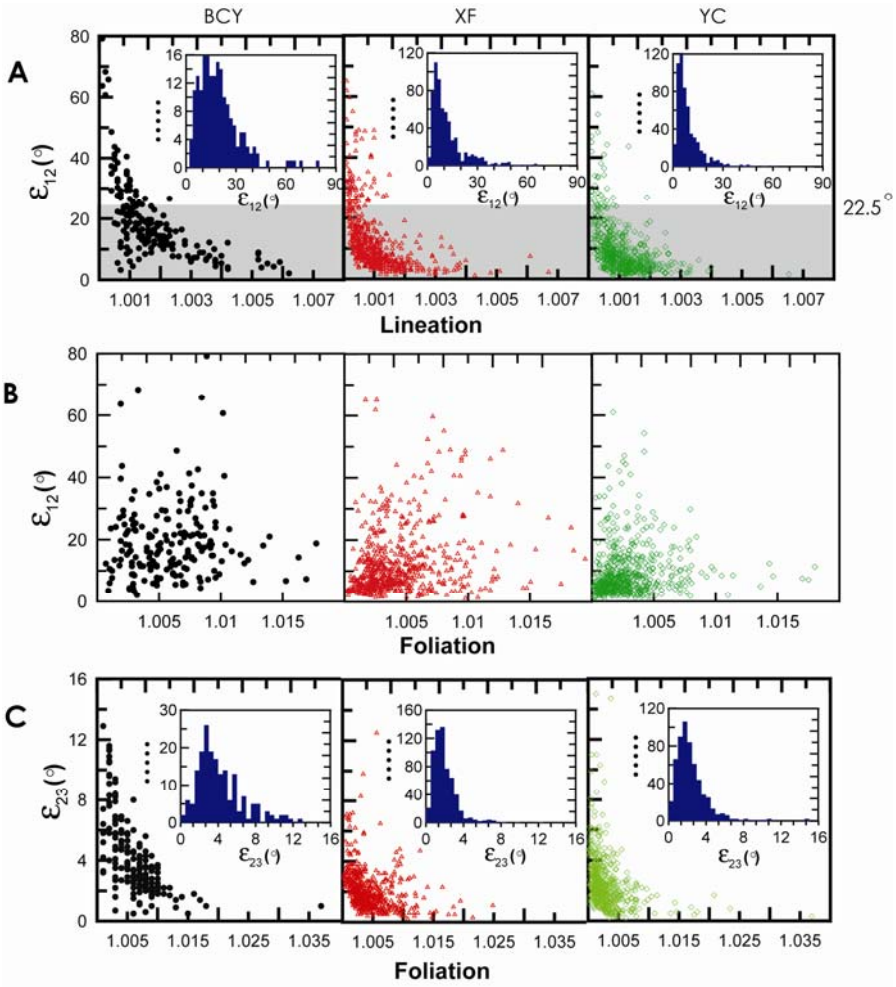

Figure 2.5 (a) Plots of ε_{12} (the 95% confidence ellipse of K_{max} in the plane joining K_{max} and K_{int}) against lineation. The plots demonstrate inverse relationship between ε_{12} and lineation. (b) Plots of ε_{12} against foliation. The plots demonstrate independence between ε_{12} and foliation. (c) Plots of ε_{23} (the 95% confidence ellipse of K_{min} in the plane joining K_{min} and K_{int}) against foliation. BCY – Baicaoyuan, XF – Xifeng, and YC – Yichuan sections. The inserts are the frequency distributions of ε_{12} using 2° bin sizes and ε_{23} using 0.5° bin sizes. They demonstrate that majority of the samples satisfies statistically significant level of $\varepsilon_{12} < 22.5°$ (70.1% for BCY, 86.6% for XF, and 92.3% for YC). The significance level of ε_{23} is < 11.25° for absolute majority of the samples.

Figure 2.6 illustrates the principal orientations of the minimum and maximum susceptibility axes (K_{min} and K_{max}). The majority of K_{max} are distributed along the edge of the stereonets in the Baicaoyuan section. The declinations and inclinations of K_{max} and K_{min} in the stereonet projection are

illustrated by a single point for each sample in Figure 5a. Figure 5d demonstrates selected samples for which $\varepsilon_{12} < 22.5^{\circ}$ and I - $K_{min} > 70^{\circ}$. Samples were selected using the technique suggested by Lagroix and Banerjee (2004b) and Zhu et al. (2004) in order to isolate the most significant K_{max} declination. All D - K_{max} with $\varepsilon_{12} > 22.5^{\circ}$ were rejected to eliminate noisy directions. Lagroix and Banerjee (2004b) discuss this approach and suggest such filter because $\varepsilon_{12} = 22.5^{\circ}$ yields a confidence ratio of 1.0 for maximum and intermediate susceptibility axes in the foliation plane. The rejection of inclinations I - K_{min} lower than 70º provides that only undisturbed sediments are considered. Alternatively we applied contour lines and rose diagrams to illustrate the distribution of K_{max}.

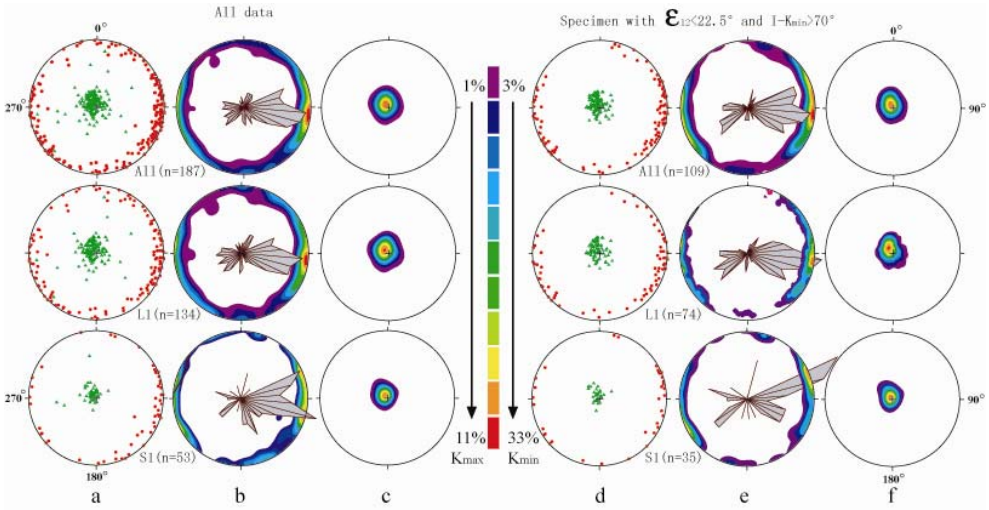

Figure 2.6 AMS results for the Baicaoyuan section: stereographic projection of K_{max} (red dots) and K_{min} (green triangles) (a, d); contours and rose diagram of K_{max} (b, e); contours of K_{min} (c, f). Parameter n is a number of samples included to the analysis. Legend corresponds to a percentage of the samples falling in the indicated by the color contour lines for K_{max} (left) and K_{min} (right).

Figures 2.6 b and 2.6 c illustrate the distributions of K_{max} and K_{min} directions for all samples and Figures 5e and 5f visualize the same for selected samples with $\varepsilon_{12} < 22.5^{\circ}$ and I - $K_{min} > 70^{\circ}$. To construct the contour lines of the stereonet projections we followed the computing method described by Robin and Jowett (1986) that calculates the point distribution densities and their significance over

the lower hemisphere. The method allows us to observe higher concentrations in the sample and to appreciate the significant discrepancy from a uniform distribution.

Rose diagrams for D - K_{max} are a favorite method of depicting orientations because of their ease of comprehension. To construct the rose diagrams in Figures 2.6b and 2.6e, we split the stereonet into an equal number of 10° segments; each segment on the stereonet represents a number of samples and the direction of the D - K_{max}. The longest segments of the rose diagrams and the peak orientation (maximum density of the contour lines) signify the larger number of samples in the specific direction. Without considering the inclination, the rose diagram magnifies only variations in K_{max} declinations. K_{max} has the majority of samples oriented along the NEE direction in the loess horizon L_1 (maximum is at D - K_{max} = 95° from the contour distribution, and it is 90–100° from the rose diagram analysis of Figure 2.6b). The maximum axis susceptibility has two major values in the paleosol horizon S_1 at D - K_{max} = 105° and at D - K_{max} = 69°. The contour lines in Figures 5c and 5f represent the distribution of K_{min} axes on the stereonet projection. The majority of the minimum susceptibility directions are located near the vertical plane with notable imbrications toward the NW (Figure 2.6c and 2.6f). The peak orientation of the contour lines and rose diagram for loess and paleosol are fairly close to each other (D - K_{min} = 323°, I - K_{min} = 85° for L_1 and D - K_{min} = 324°, I - K_{min} = 85° for S_1) and to the major route direction of the present day summer monsoon (An, 2000; An et al., 2001; Porter, 2001).

Combined analysis of all units in the Xifeng section indicates that the K_{max} directions are distributed along a girdle primarily toward the SE (Figures 2.7 b and 2.7 e). The peak orientation of K_{max} indicated by the maximum density of the

contour lines or the longest section of the rose diagram is D - K_{max} = 130° for L_1 and D - K_{max} = 125° for S_1 in samples depicted in Figures 2.7 b and 2.7 e. The preferred orientation of the minimum AMS axis is tilted to the NW (Figure 2.7c and 2.7 f). The peak orientation of the contour lines for loess and paleosol are close to each other (D - K_{min} = 328°, I - K_{min} = 86° for L_1 and D - K_{min} = 327°, I - K_{min} = 80° for S_1), similar to other sections, and correspond to the present day summer monsoon path.

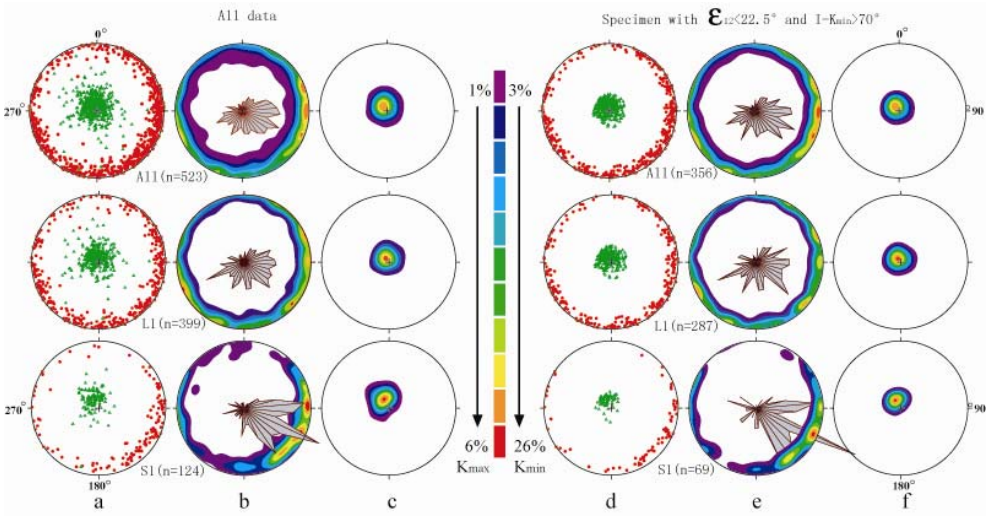

Figure 2.7 AMS results for the Xifeng section: stereographic projection of K_{max} (red dots) and K_{min} (green triangles) (a, d); contours and rose diagram of K_{max} (b, e); contours of K_{min} (c, f). Parameter n is a number of samples included to the analysis. Legend corresponds to a percentage of the samples falling in the indicated by the color contour lines for K_{max} (left) and K_{min} (right).

Figure 2.8 illustrates the AMS inclinations and declinations for the Yichuan section. The major SE direction of L_1 and S_1 units in the Yichuan sections are well illustrated by the contour lines and the rose diagram in Figures 2.8 b and 2.8 e. The orientation of the AMS ellipsoid indicated by the peak orientation or the longest section of the rose diagram has D - K_{max} = 131° for L_1 and D - K_{max} = 151° for S_1 for samples with ε_{12} < 22.5º and I - K_{min} > 70º. The peak orientation of

K_{min} or the longest section of the rose diagram tilted to the NW has D - K_{min} = 323°, I - K_{min} = 87° for L_1 and D - K_{min} = 297°, I - K_{min} = 86° for S_1.

Additionally we performed analysis of the AMS results of selected samples with $\varepsilon_{12} < 11.25°$ and I - $K_{min} > 70°$ for the studied sections (Figure 2.9). These results coincide with the findings of the preferable AMS orientation using all samples and samples with $\varepsilon_{12} < 22.5°$.

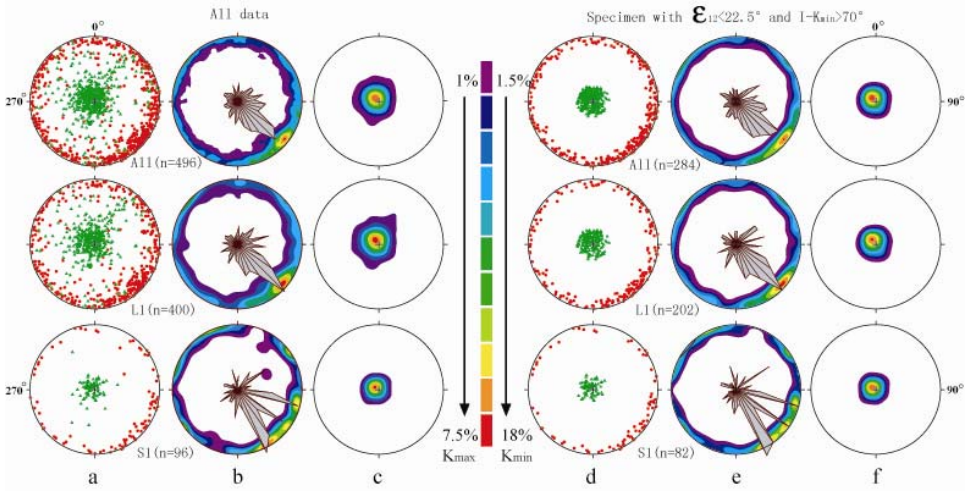

Figure 2.8 AMS results for the Yichuan section: stereographic projection of K_{max} (red dots) and K_{min} (green triangles) (a, d); contours and rose diagram of K_{max} (b, e); contours of K_{min} (c, f). Parameter n is a number of samples included to the analysis. Legend corresponds to a percentage of the samples falling in the indicated by the color contour lines for K_{max} (left) and K_{min} (right).

2.4. Discussion

The contour lines and rose diagrams in Figures 2.6 –2.8 illustrate the statistically preferred orientation of the AMS in the sections studied. The declination of the K_{max} mean directions (D - K_{max}) is nearly horizontal and is projected on the edge of the stereonets. We calculated the peak orientations (declinations and inclinations) for K_{max} and K_{min} for the studied sections using contour lines (Table 2.2). The peak orientations demonstrate that the preferred

orientation of the elongated particles was in the SE direction in the Xifeng and Yichuan sections and in the SEE direction in the Baicaoyuan section. Such orientations indicate that the prevailing paleowind direction was from the SE and SEE on a local scale. Furthermore, the majority of the samples have minimum axes oriented vertically with their peak orientations tilted towards the NW (323°/86°, 325°/85°, and 307°/86° in Baicaoyuan, Xifeng, and Yichuan, respectively). Tarling and Hrouda (1993) and Zhu et al. (2004) demonstrated that the wind tends to change the sedimentary grain orientation and to tilt the longest axes of the grains as demonstrated in Figure 2.1. The minimum AMS axes would be imbricated to a downstream direction (NW in our cases) by small angles (< 20°).

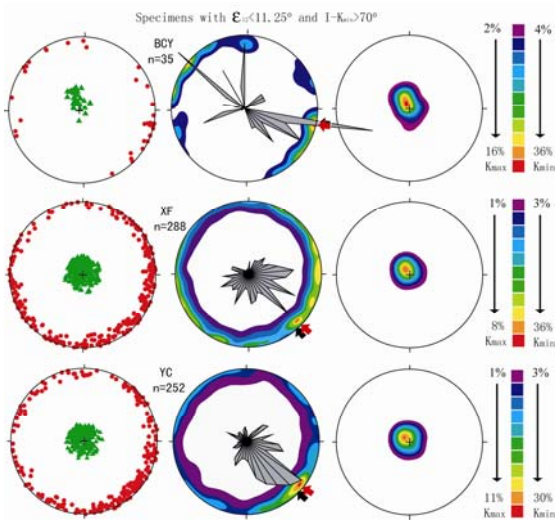

Figure 2.9 AMS results of selected samples where ε_{12} < 11.25º and I - K_{min} > 70º for Baicaoyuan (BCY), Xifeng (XF), and Yichuan (YC) sections. Left: stereographic projection of K_{max} (red dots) and K_{min} (green triangles). Center: contour lines and rose diagrams of K_{max}.. Right: contour lines of K_{min}. Parameter n is a number of samples included to the analysis. Legend corresponds to a percentage of the samples falling in the indicated by the color contour lines for K_{max} (left) and K_{min} (right).

In order to explore statistical significance of our results we calculated the mean directions and corresponding error ellipsoids for the studied sections using

Bootstrap statistics (Constable and Tauxe, 1990) additionally to the maxima analysis of rose diagrams and contour lines. The great advantage of bootstrap is its appropriate way to control and check the stability of the results. The echnique allows estimation of the sample distribution using only very simple methods. It is simplicity to derive estimates of standard errors and correlation coefficients. The results are similar for Baicaoyuan section and deviate from each other only slightly for Xifeng and Yichuan sections (Table 2.3, Figure 2.10).

Table 2.2 Peak orientations (declination/inclination) for different sections and horizons calculated using the contour lines.

Horizon	**All data**			**Data with ε_{12}<22.5º and Inc-K_{min}>70º**		
	N	K_{max}(D/I)	K_{min}(D/I)	N	K_{max}(D/I)	K_{min}(D/I)
L_1+ S_1 (BCY)	187	**96**°/3°	309°/84°	109	**95°**/3°	323°/85°
L_1 (BCY)	134	95°/3°	309°/84°	74	97°/2°	323°/85°
S_1 (BCY)	53	105°/2°	312°/83°	35	69°/3°	324°/85°
L_1+ S_1 (XF)	521	**128**°/3°	327°/83°	354	115°/3°	325°/85°
L_1 (XF)	399	130°/3°	331°/85°	287	130/°3°	328°/86°
S_1 (XF)	124	115°/3°	328°/78°	69	115°/3°	327°/80°
L_1+ S_1 (YC)	496	**129**°/3°	314°/84°	284	129°/3°	307°/86°
L_1 (YC)	401	131°/3°	322°/83°	202	131°/3°	313°/86°
S_1 (YC)	95	150°/3°	282°/86°	82	151°/2°	297°/86°

N – number of samples; BCY – Baicaoyuan section; XF – Xifeng section; YC – Yichuan section. Bold numbers correspond to the dominant wind direction illustration.

The K_{max} and K_{min} orientations demonstrate that the preferred wind direction was from SE and SEE. The Bootstrap statistics treats the AMS ellipsoid as a tensor with three orthogonal eigenvectors (K_{max}, K_{int} and K_{min}). The Bootstrap statistics calculation clearly demonstrates that the mean K_{min} orientations are statistically different from the vertical axis in every studied locality and can be evaluated in terms of imbrication of the ferrimagnetic and paramagnetic particles. At the same time the tensor's average for K_{max} displays the noticeable difference between peak orientation and Bootstrap mean direction.

Table 2.3 Mean direction and corresponding statistical parameters for all studied sections using Bootstrap statistics (Constable and Tauxe, 1990).

Horizon		K_{max}		K_{int}		K_{min}	
	N	D/I	$E_1//E_2$	D/I	$E_1//E_2$	D/I	$E_1//E_2$
L_1+S_1 (BCY)	187	90.9°/4.2°	33.3°/2.4°	181.1°/3.0°	33.3°/2.9°	307.2°/84.8°	2.9°/2.4°
L_1 (BCY)	134	88.7°/3.7°	33.8°/2.5°	178.9°/2.9°	33.8°/3.2°	306.2°/85.3°	3.2°/2.5°
S_1 (BCY)	53	100.8°/5.5°	32.9°/2.3°	191.1°/2.9°	32.9°/2.2°	308.7°/83.7°	2.2°/2.1°
L_1+S_1 (XF)	521	100.3°/5.2°	34.1°/2.6	190.8°/5.4°	34.1°/2.7°	326.8°/82.4°	2.7°/2.6°
L_1 (XF)	399	88.3°/3.3°	34.5°/2.7°	178.7°/4.7°	34.5°/2.5°	323.6°/84.2°	2.5°/2.7°
S_1 (XF)	124	111.6°/9.4°	19.7°/2.4°	202.9°/7.7°	19.7°/2.6°	331.5°/77.8°	2.6°/2.4°
L_1+S_1 (YC)	496	136.3°/5.9°	27.3°/2.9°	46.1°/2.5°	27.4°/3.3°	293.1°/83.5°	3.3°/2.9°
L_1 (YC)	401	136.8°/6.8°	28.7°/3.1°	46.5°/2.5°	28.7°/3.5°	296.4°/82.8°	3.5°/3.1°
S_1 (YC)	95	133.5°/3.7°	29.6°/1.9°	43.4°/2.5°	29.7°/2.6°	279.2°/85.5°	2.5°/1.9°

BCY – Baicaoyuan section; XF – Xifeng section; YC – Yichuan section; N – number of samples; D/I – declination/inclination of K_{max} (K_{int}, K_{min}) mean value; $\mathbf{E_1/E_2}$ – major and minor semi-axes of the uncertainty ellipses defined by the eigenvectors.

One can use either peak orientation or Bootstrap mean for the paleowind direction reconstruction. The rose diagrams illustrate that the orientation distribution of K_{max} and K_{min} are not perfectly aligned in the opposite directions (Figure 2.10), as it would be expected if only prolate particles are present. The AMS of a measured cubic specimen is the sum of each particle AMS. The crystallographic axes of the particle control AMS of a silicate particle (Lagroix and Borradaile, 2000). Magnetite and maghemite, due to their strong intrinsic magnetization and internal demagnetizing field, have AMS controlled by the particle shape where the maximum susceptibility axe is parallel to the grain's long dimension in multi/pseudo domain particles. In stable single domain particles the maximum susceptibility axe is perpendicular to the grain's long dimension. At the particle level, silicates generally give oblate AMS ellipsoid, while magnetites give prolate AMS ellipsoids. The orientation distribution of the magnetite particles versus the silicate particles controls the AMS at the specimen level. The peak

orientation of the K_{max} distribution represents the elongate magnetite grain's orientation while K_{min} is always contaminated by the distribution of the oblate silicate mineral particle's short dimension. Therefore for our paleowind direction reconstruction we prefer to use the peak orientation of K_{max} from the contour lines. We use K_{min} only as an additional factor to determine that apparently the SE direction of the wind caused the particle's imbrications. The different statistics techniques, however, coincide generally between each other in our study and do not alter our conclusions.

Thistlewood and Sun (1991) and Hus (2003) showed that the winter monsoon that comes primarily from the northwestern central Asian desert areas carries a majority of the sedimentary particles and determines the magnetic fabrics' orientation in the loess and paleosol horizons.

Wind tunnel experiments (Wu et al., 1998) showed that eolian deposition is analogous to deposition under hydrodynamic conditions (Rees and Wooddall, 1975; Tarling and Hrouda, 1993). These experiments showed a strong correlation with deviations less than 20° from the actual current direction. In the samples investigated here we compared the K_{max} and K_{min} directions with the theoretically predicted depositional fabrics that would be expected under hydrodynamic flow (Tarling and Hrouda, 1993) and with laboratory results for running water experiments (Rees and Wooddall, 1975). Figure 1.9 illustrates the results of these studies. When deposition occurs in still water, gravitational settling is the only significant force and the majority of rod-like ferromagnetic grains are arranged with their longer axes aligned randomly within the bedding plane. This gives rise to a simple oblate fabric in the bedding plane (Figure 1.9a). Under a weak water current, most elongated magnetite grains line up parallel to the direction of the

current and the superposition of gravity and current forces causes most of the maximum AMS axes to tilt to the upstream direction and the minimum axes (K_{min}) to tilt to the downstream direction (Figure 1.9 b). The prolate grains are more stable when their longest axes lie perpendicular to the direction of water flow. The stronger the current, the higher the tendency of prolate particles to become oriented perpendicular to the current flow (Figures 1.9 c, 1.9 d).

We suggest a simple explanatory model to explain our AMS results. Current theory states that relatively cold and dry winter monsoon is a major driving force of the grain orientation that yields magnetic fabric (Thistlewood and Sun, 1991). Magnetic fabric is formed by the superposition of gravity and wind forces (Figure 2.11). The wind carries eolian material in the air while gravity pulls the sedimentary grains to earth. On the ground, sedimentary grains are reoriented by wind until they are covered by a new layer of eolian sediment. As layers accumulate on top, the loess becomes immobile and finally solidifies. Magnetic minerals remain ambulant until they solidify. Before burial and eventual solidification, eolian material can be transported back and forth from air to ground if the wind is strong enough. Consequently the particles could probably be rearranged again until they are fixed in the sedimentary layers. Rain and more wind are brought by the moist summer monsoon which approaches from the SE, a direction opposite to that of the winter monsoon (Figure 2.2).

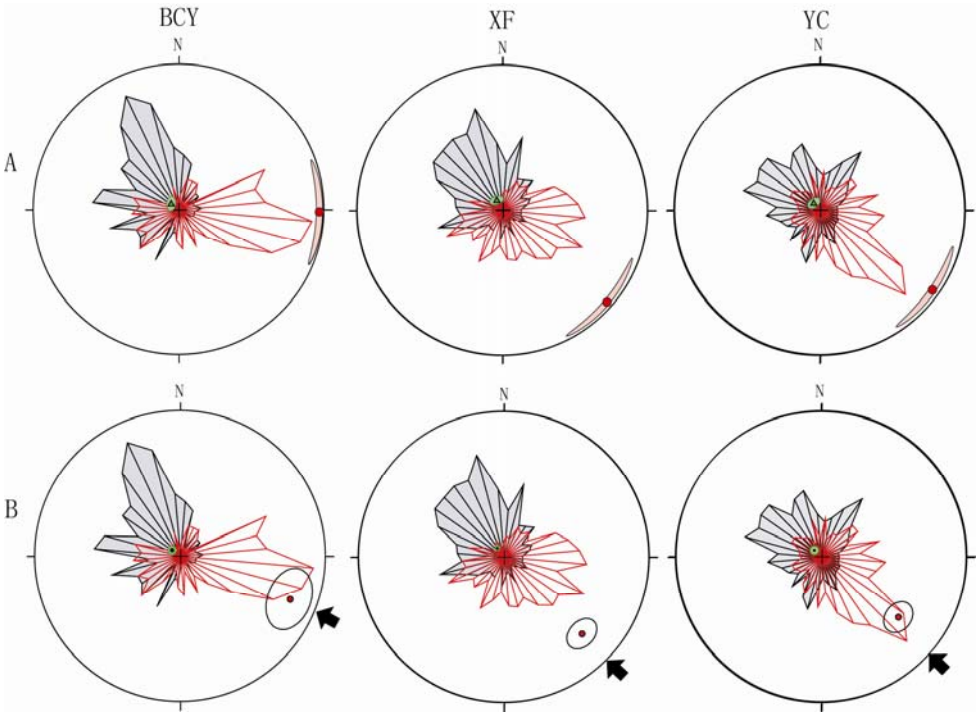

Figure 2.10 Illustration of the Bootstrap statistics applied for the mean direction of the AMS ellipsoid for the for Baicaoyuan (BCY), Xifeng (XF), and Yichuan (YC) sections (see also Table 3). The dataset for all samples of L_1 and S_1 horizons is included in this illustration although datasets with $\varepsilon_{12} < 22.5^{\circ}$ and $\varepsilon_{12} < 11.25^{\circ}$ show very similar results. Rose diagram for K_{max} is shown in red and for K_{min} is shown in grey color. Bootstrap ellipsoids for eigenvectors of K_{max} (red), K_{int} (blue) and K_{min} (green). Calculations are done using AGICO's software package for the KLY magnetic susceptibility meter using technique developed by Constable and Tauxe (1990). (B) Black (red) arrow corresponds to the mean direction for the dominant wind direction calculated using peak orientation (tensor mean) for K_{max}.

We suggest that the summer monsoon wind in the study area (west and center of the Chinese Loess Plateau), which is stronger than the winter monsoon wind (Figure 2.12), is strong enough to rearrange the sedimentary particles in the study areas again. The rain often falling during the summer does not allow the wind to displace the particles far from the site and finally fixes them in the loess or soil layer. New formed magnetite particles at the top of the soil are also reoriented by the summer wind and rain.

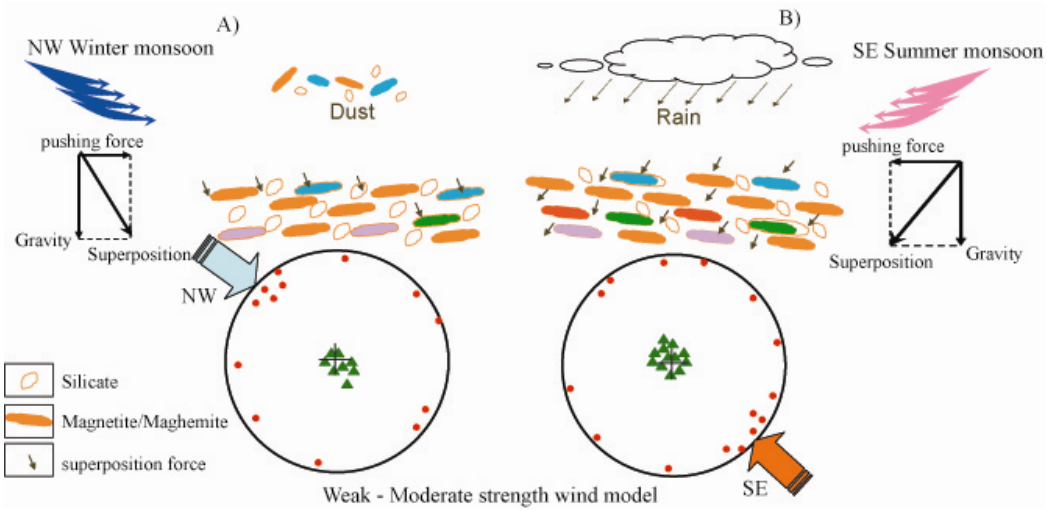

Figure 2.11 A model of AMS that depends on the monsoon directions in the southern part of the Chinese Loess Plateau.
(a) The winter monsoon brings sedimentary and magnetic particles with the dust from the NW. The AMS ellipsoid would reflect the prevailing orientation of the particles as shown in the stereonet below (lower hemisphere projection).
(b) The summer monsoon brings rain and wind from the SE, reorienting and finally fixing sedimentary and magnetic grains in the uppermost seasonally formed layer of loess or soil. The AMS ellipsoid is now oriented in a direction opposite to the winter monsoon direction. Rain helps to settle the sedimentary and magnetic grains and the growing summer vegetation fixes them in-situ. Grains become immobile. The next winter monsoon covers the site with new eolian material and the process repeats.

The rapidly developing summer vegetation covers the newly-formed loess/soil layer and the plant roots do not allow the next winter monsoon to re-orient the grains of the solidified layer. The main process likely occurs during one year although some later compaction of the loess could still take place and cause certain 'noise' in our measurements. The new magnetite formed by pedogenesis processes in the deeper soil layers under surface additionally enhanced the total MS signal but not necessary AMS values. Our model also implies that a lock-in depth phenomenon does not affect at least studied S_1 and L_1 horizons. Such possibility was recently debated by Zhu et al. (2006) for L_1 loess and Liu et al. (2008b) for Brunhes/Matuyama boundary.

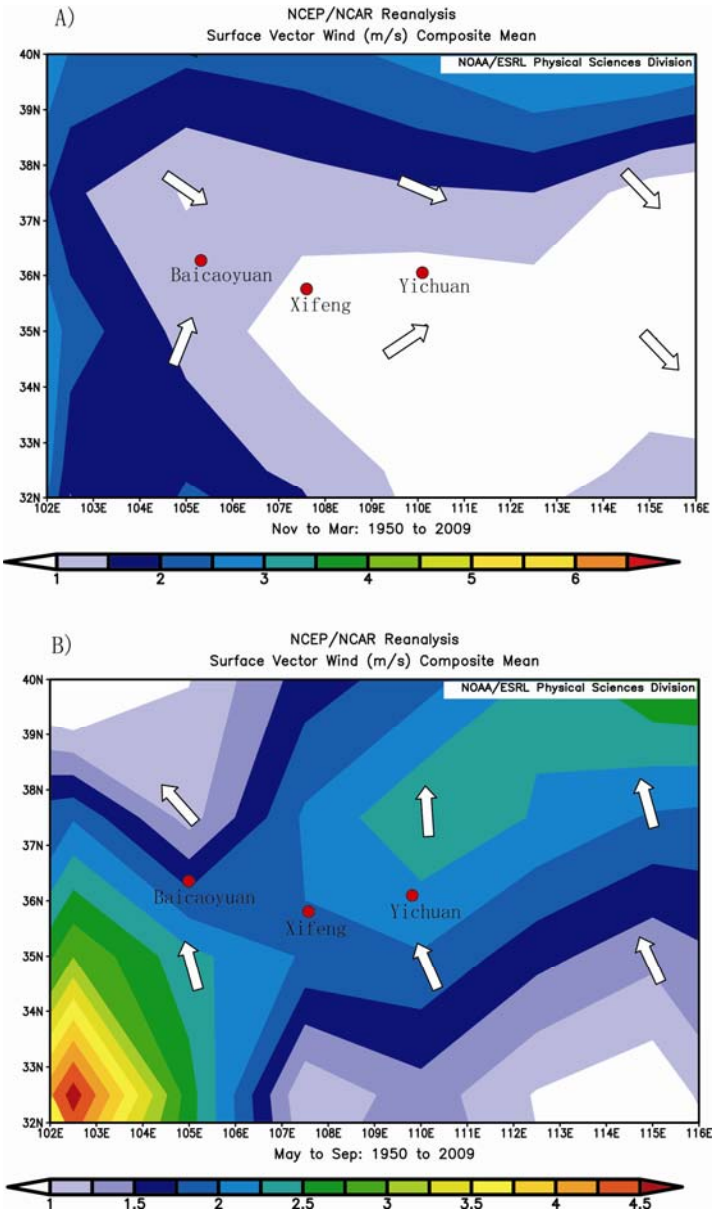

Figure 2.12 Surface wind vectors for (A) the winter months of November-March and (B) the summer months of May-September are calculated from the 1950 to 2009 monthly long-term means. Data was compiled by the NOAA-CIRES's NCEP Reanalysis Atlas. Contours are wind velocities in meters per second. In the loess deposits, winter prevailing surface winds come from NW, SW while summer prevailing winds comes from the SSE, SE.

We consider that both K_{max} and K_{min} orientations could be correlated to the predominant paleowind direction during the summer monsoon in the Chinese Loess Plateau regions. The mean AMS axes directions in the loess horizon L_1 and

paleosol horizon S_1 are both in the SE quarter of the stereonet and broadly correspond to the course of the summer monsoon (Figure 2.13).

We compared our result with the present day regional wind directions using the on-line publically available tool from Physical Sciences Division of Earth System Research Laboratory (National Oceanic and Atmospheric Administration, U.S. Department of Commerce) (Figure 2.12). Surface wind directions and speed for the winter months of November-March (Figure 2.12 a) and the summer months of May-September (Figure 2.12 b) are calculated from the 1950 to 2009 monthly long-term means. The regional winter monsoon wind in the study area is dominantly from north-west and south-south-west. The winter wind is however relatively weak (1–2 m/s) when comparing to the summer monsoon wind strength (2–3 m/s). The strong winter monsoon wind in the desertic areas north of Chinese Loess Plateau carries the dust particles to the Plateau where the particles are deposited (the winter monsoon wind over the Plateau is too weak to carry the particles further). The stronger summer monsoon wind from SW and SSW in the study area of the Plateau is continuously accompanied by the rain and moister which does not allow the loess particles to be transported away from the Plateau.

The model for Chinese Loess Plateau interglacial horizon, i.e. paleosol, formation implies that up to 70% of the particles responsible for the MS signal are crystallized in-situ and are not transported by the wind (Evans and Heller, 2003; Xie et al., 2009). Since we observe that the dominant fabric orientation in loess and paleosol is similar, the prevailing winds are able to reorient grains that are on the ground. Maher and Taylor (1988) were first to demonstrate that the peak neo-formation of fine-grained ferrimagnetics in the modern topsoil is not exactly at the surface but more commonly a few centimeters below the surface. In the specimen

we cannot separate AMS of detrital and pedogenic magnetite but our data demonstrate that overall the AMS signal in S_1 horizons is as strong as in L_1 horizons (Figures 2.6–2.8). We suggest that although the neo-formed magnetite particles contribute to the higher MS values, they are predominantly chaotically oriented in terms of preferred axis orientation and therefore the individual AMS of pedogenic particles generally cancel each other's effects. This way the detrital contribution from the particles arranged by the summer monsoon still dominates the total AMS signal.

Figure 2.13 depicts the spatial variations of the preferred paleowind directions along the Loess Plateau. The contour lines and rose diagrams are separated for loess L_1 and paleosol S_1 combined in every section, while actually there is no significant difference in AMS orientations between soil and loess horizons. In our model the orientations of K_{max} in Yichuan (the upwind azimuth is 129°), Xifeng (128°), and Baicaoyuan (96°) are associated with the summer monsoon coming from the SE in the whole dataset. We observe a shift of ≈ 32° in the monsoon route for the Baicaoyuan section which is located to the west of the WE corridor between the north and south Liupan Mountains. We assume that the mountains cause the monsoon to deviate and propagate deeper into the continent in the Baicaoyuan area. Such local wind deviation does not contradict the present day regional wind course in the study area (Figure 2.12).

The primary SEE directions in the Baicaoyuan section are similar to the weak current model (Tarling and Hrouda, 1993) in Figure 1.9 because the majority of individual K_{max} orientations in the sample are parallel to the direction of the summer monsoon, forming primary SEE and secondary NWW directions. In the Xifeng section, the distributions of magnetic lineation are not clustered well

around the maximum in the contour area and have few remarkably long 10° sectors in the rose diagram that forms a girdle around the SE direction. Based on our comparison to the moderate water current model in Figure 8, we consider that a moderate wind caused rolling of some elongate particles turning them perpendicular to the wind direction; therefore, the magnetic lineation varies notably in its orientation and is spread all over the stereonet projection. The K_{min}, however, is still shifted toward the NW defining the summer monsoon propagation from the SE. The Xifeng section is situated on a large flat surface which is far from the mountains that characterize the Baicaoyuan section and the Yellow River terrace of the Yichuan section. Thus the Xifeng site is more open to the winds than the Baicaoyuan and Yichuan sites. The summer monsoon, unrestricted by mountains and river terrace, could change direction more easily on an open plain. The distributions of K_{max} in Yichuan are intermediate between Baicaoyuan and Xifeng and only one primary direction could be identified in the SE direction. This means that the wind strength in the Yichuan area was stronger than in the Baicaoyuan area and weaker than in the Xifeng area; we classify the wind strength in the Yichuan area as weak-moderate.

In order to independently verify our summer monsoon model, we examined the AMS results from two other sections in the Loess Plateau. One section is described in the east of the Loess Plateau (Liu et al., 2008a) and other is studied near Xi'an (Thistlewood and Sun, 1991). The AMS results from these papers are included to Figure 2.13. Although we cannot quantify the wind strength without their dataset, their primary directions look identical to our weak to moderate wind summer monsoon model. Their samples represent multiple loess and paleosol layers and result demonstrates that the vertical minimum axes K_{min} are tilted towards the NW direction and maximum axes K_{max} are oriented mostly to the SE

direction. It confirms our summer monsoon model that explains the AMS orientation in the central and western parts of the Chinese Loess Plateau. It is a matter of the future study to verify if the AMS signal from the northern parts of the Plateau fits in our model. The winter monsoon wind in the North is much stronger than the summer monsoon wind and the magnetic particle could be probably oriented during the winter only. Such scenario would result in the AMS ellipsoid orientations toward NW.

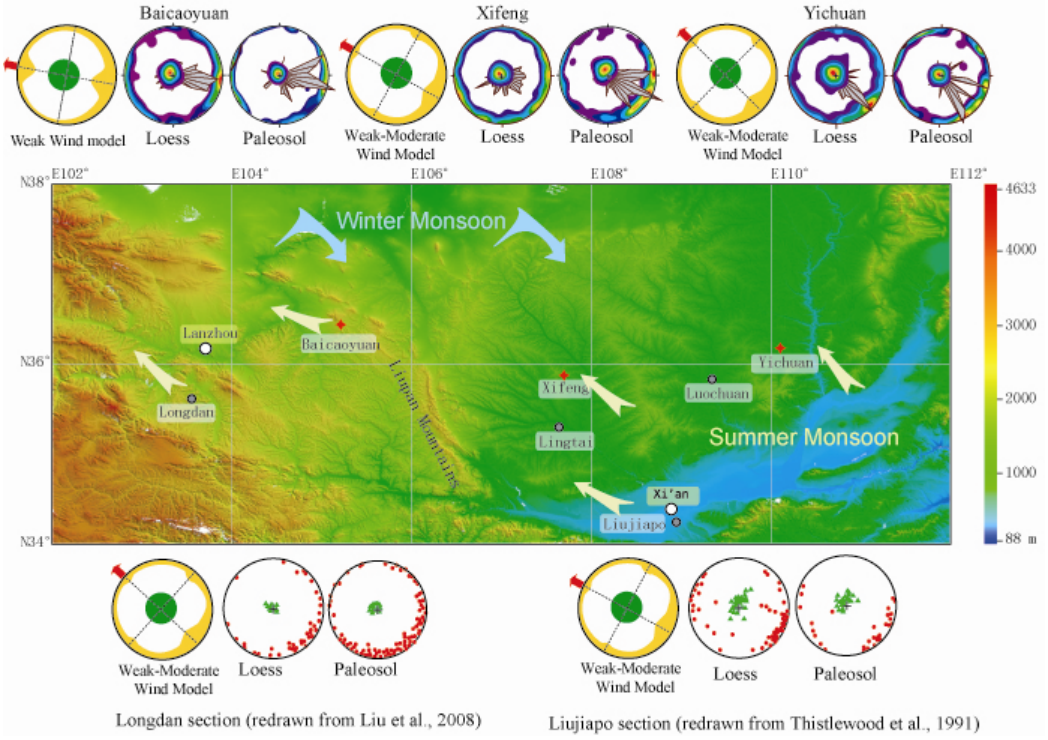

Figure 2.13 Dominant summer monsoon routes for last 130 kyrs reconstructed from our AMS analysis along the west-central transect across the Chinese Loess Plateau. Arrows illustrate the ancient summer monsoon wind direction; the relative strength of the wind is specified by the comment near each local wind model stereographic projection.
Above: lower hemisphere stereographic projections showing the contour lines and rose diagrams for K_{max} for all studied samples with arrows pointing toward major summer monsoon directions in every locality. Below: lower hemisphere stereographic projection of K_{max} and K_{min} from two other localities. Note that original figures in Thistlewood and Sun (1991) are shown for the upper hemisphere.

2. 5 Conclusions

We have studied the AMS in three sections representing the most recent 130 kyr interval along a W–E transect in the Chinese Loess Plateau. The orientations of major and minor AMS axes of sedimentary particles in the studied loess and paleosol sequences were determined to evaluate the paleowind direction. AMS measurements were used to identify the paleowind direction in three eolian deposits in the Chinese Loess Plateau. In our model, the AMS ellipsoid orientation is determined by the moist summer monsoon rather than the dry winter monsoon as previously hypothesized. We consider that the stronger summer monsoon that brings almost all annual rainfall plays a major role in the orientation of near surface dust particles and in their final consolidation. Based on our model, the major stream of the paleowind over the last 130 kyr has been generally similar to the present day summer monsoon routes.

Bibliography

An, Z., 1991. Magnetic Susceptibility Evidence of Monsoon Variation on the Loess Plateau of Central China during the Last 130,000 Years. Quaternary Research 36, 29–36.

An, Z., 2000, The history and variability of the East Asian paleomonsoon climate. Quaternary Science Reviews 19, 171–187.

An, Z., Kutzbach, J. E., Prell, W. L., Porter, S. C., 2001, Evolution of Asian monsoons and phaseduplift of theHimalaya-Tibetan plateau since Late Miocene times. Nature 411, 62–66.

An, Z., Porter, S. C., 1997. Millennial-scale climatic oscillations during the last interglaciation in central China. Geology 25, 603–606.

Balsley, J. R., Buddington, A. F., 1960. Magnetic susceptibility anisotropy and fabric of some Adirondack granites and orthogneisses. American Journal of Science 258A, 6–20.

Banerjee, S. K., Hunt, C. P., Liu, X. M., 1993. Separation of local signals from the regional paleomonsoon record of the Chinese loess plateau: A rock magnetic approach, Geophys. Res. Lett., 20: 843-846.

Bassinot, F. C., Labeyrie, L. D., Vincent, E., Quidelleur, X., Shackelton, N. J., Lancelot, Y., 1994. The astronomical theory of climate and the age of the Brunhes-Matuyama magnetic reversal. Earth and Planetary Science Letters. 126, 91–108.

Borradaile, G. J., 1987. Anisotropy of magnetic susceptibility rock composition versus strain. Tectonophysics 138, 211–223.

Borradaile, G. J., Henry, B., 1997. Tectonic applications of magnetic susceptibility and its anisotropy. Earth Science Reviews 42, 49– 93.

Cande, S. C., Kent, D. V., 1995. Revised calibration of the geomagnetic polarity timescale for the Late Cretaceous and Cenozoic. Journal of Geophysical Research 100, 6093–6095.

Constable, C., Tauxe, L., 1990. The bootstrap for magnetic susceptibility tensors. Journal of Geophysical Research 95, 8383–8395.

Deng, C., Zhu, R., Verosub, K. L., Singer, M. J., Vidic, N. J., 2004, Mineral magnetic properties of loess/paleosol couplets of the central loess plateau of China over the last 1.2 Myr. Journal of Geophysical Research, 109, B01103, doi:10.1029/2003JB002532.

Deng C. L., 2008, Paleomagnetic and mineral magnetic investigation of the Baicaoyuan loess-paleosol sequence of the western Chinese Loess Plateau over the last glacial-interglacial cycle and its geological implications. *Geochemistry Geophysics Geosystems* 9, Q04034, doi: 10.1029/2007GC001928.

Derbyshire, E., Billard, A., Vliet-Lanoe, B.V., Lautridou, J. P., Cremaschi, M., 1988. Loess and paleoenvironment some results of a European joint programme of research. Journal of Quaternary Science 3, 147–169.

Ding, Z., Sun, J., Rutter, N. W., Liu, T., 1999. Changes in Sand Content of Loess Deposits along a North–South Transect of the Chinese Loess Plateau and the Implications for Desert Variations. Quaternary Research 52, 56–62.

Evans, M.E., Heller, F., 2003. Environmental Magnetism: Principles and Applications of Enviromagnetics, Elsevier Science, Academic Press.

Fisher, R., 1953. Dispersion on a sphere. Proceedings Royal Society London, Series A 217, 295–305.

Graham, J. W., 1954. Magnetic anisotropy, an unexploited petrofabric element. Geological Society of America Bulletin 65, 1257–1258.

Grannar, L., 1958. Magnetic measurements on Swedish varved sediments. *Arkiv, F, Geofysik*, 3, 1-40.

Heider, F., Dunlop, D. J., Sugiura, N., 1987. Magnetic properties of hydrothermally recrystallized magnetite crystals. Science 236, 1287–1290.

Heller, F., Beat, M., Wang, J., Liu, H., Liu, T., 1987. Magnetization and sedimentary history of loess in the central Loess Plateau of China. in : T.S. Liu (Ed.), Aspects of Loess Research, China Ocean Press, Beijing, 147–163.

Hrouda, F., 1982. Magnetic anisotropy of rocks and its application in geology and geophysics. Surveys in Geophysics 5, 37–82.

Hus, J. J, 2003. The magnetic fabric of some loess/palaeosol deposits. Physics and Chemistry of the Earth 28, 689–699.

Jackson, M. J., Tauxe, L., 1991. Anisotropy of magnetic susceptibility and remanence: Developments in the characterization of tectonic, sedimentary, and igneous fabric. U.S. Natl. Rep. Int. Union Geod. Geophys. 1987–1990, Reviews of Geophysics, 29, 371–376.

Jelinek, V., 1981. Characterization of the magnetic fabric of rocks. Tectonophysics 79, 63–67.

Lagroix, F., Banerjee, S. K., 2002. Paleowind directions from the magnetic fabric of loess profiles in central Alaska. Earth and Planetary Science Letters 195, 99–112.

Lagroix, F., Banerjee, S. K., 2004a. Cryptic post-depositional reworking of aeolian sediments revealed by the anisotropy of magnetic susceptibility. Earth and Planetary Science Letters 224, 453–459.

Lagroix, F., Banerjee, S. K., 2004b. The regional and temporal significance of primary aeolian magnetic fabrics preserved in Alaskan loess. Earth and Planetary Science Letters 225, 379–395.

Lagroix, F., Borradaile, G.J., 2000. Magnetic fabric interpretation complicated by inclusions in mafic silicates. Tectonophysics 325 (3-4), 207–225.

Li, T., 2006. The process and mechanism of the rise of the Qinghai-Tibet Plateau. Tectonophysics 260, 45–53.

Liu, X. M., Xu, T., Liu, T., 1988. The Chinese loess in Xifeng, II. A study of anisotropy of magnetic susceptibility of loess from Xifeng. Geophysical Journal International 92 349–353.

Liu, P., Jin, C. S., Zhang, S., Han, J. M., Liu, T. S. 2008a. Magnetic fabric of early Quaternary loess-paleosols of Lingdan Profile in Gansu Province and the reconstruction of the paleowind direction. Chinese Science Bulletin 53 (9), 1450-1452.

Liu, Q., Roberts, A. P., Rohling, E. J., Zhu, R. Sun, Y. 2008b. Post-depositional remanent magnetization lock-in and the location of the Matuyama–Brunhes geomagnetic reversal boundary in marine and Chinese loess sequences. Earth and Planetary Science Letters 275, 102–110.

Maher, B. A., Taylor R. M., 1988, Nature Formation of ultra-fine magnetite in soils. Nature 336, 368–370.

Matalucci, R. V., Shelton, J. W., Abdel-Hady, M., 1969. Grain orientation in Vicksburg loess. Journal of Sedimentary Petrology 39, 969–979.

Nagata, T., 1961. Rock Magnetism. 2nd edition, Maruzen, Tokyo, 350 pp.

Porter, S. C., An, Z., 1995. Correlation between climate events in the North Atlantic and China during the last glaciation. Nature 375, 305–308.

Porter, S. C., 2001, Chinese loess record of monsoon climate during the last glacial–interglacial cycle. Earth Science Reviews 54, 115–28.

Rees, A. I., 1965. The use of anisotropy of magnetic susceptibility in the estimation of sedimentary fabric. Sedimentology 4, 257– 271.

Rees, A. I., Wooddall, W. A., 1975. The magnetic fabric of some laboratory deposited sediments. Earth and Planetary Science Letters 25, 121–130.

Rieser, A. B., Bojar, A. V., Neubauer, F., Genser, J., Liu, Y. J., Ge, X. H., Friedl, G., 2009. Monitoring Cenozoic climate evolution of northern Tibet: stable isotope

constraints from the western Qaidam Basin, China. International Journal of Earth Sciences 98, 1063-1075.

Robin, P. F., Jowett, E. C., 1986. Computerized density contouring and statistical evaluation of orientation data using counting circles and continuous weighting functions. Tectonophysics 121, 207-223.

Spassov, S., Heller F., Kretzschmar, R., Evans, M.E., Yue, L. P., Nourgaliev, D. K., 2003, Detrital and pedogenic magnetic mineral phases in the loess/palaeosol sequence at Lingtai (Central Chinese Loess Plateau). Physics of the Earth and Planetary Interiors 140, 255–275.

Stacey, F. D., 1960. Magnetic anisotropy of igneous rocks. Journal of Geophysical Research 65, 2429–2442.

Tarling, D. H., and Hrouda, F., 1993. The Magnetic Anisotropy of Rocks. 217 pp., CRC Press, Boca Raton, Fla.

Thistlewood, L., Sun, J., 1991. A paleomagnetic and mineral magnetic study of the loess sequence at Liujiapo, X'ian, China. Journal of Quaternary Sciences 6, 13–26.

Vandenberghe, J., An, Z., Nugteren, G., Lu, H., Huissteden, K. V., 1997. New absolute time scale for the Quaternary climate in the Chinese loess region by grain-size analysis. Geology 25**,** 35–38.

Wu, H B, Chen, F. H., Wang J. M., Cao J. X., Zhang, Y., T., 1999. Study on the relationship between magnetic anisotropy of modern eolian sediments and wind direction. Chin. J. Geophys., 42(1): 71-78.

Xie, Q., Chen, T. Xu, H., Chen, J., Ji J., Lu, H., Wang, X., 2009. Quantification of the contribution of pedogenic magnetic minerals to magnetic susceptibility of loess and paleosols on Chinese Loess Plateau: Paleoclimatic implications. Journal of Geophysical Research, 114, B09101, doi:10.1029/2008JB005968.

Zhu, R., Liu, Q., Jackson, M. J., 2004. Paleoenvironmental significance of the magnetic fabrics in Chinese loess-paleosols since the last interglacial (<130 ka). Earth and Planetary Science Letters 221, 55–69.

Zhu, R., Liu, Q, Pan Y., Deng, C., Zhang, R., Wang, X., 2006, No apparent lock-in depth of the Laschamp geomagnetic excursion: Evidence from the Malan loess. Science in China Series D: Earth Sciences 49, 960—967.

Zhu, R., Zhang, R., Deng, C., Pan, Y., Liu, Q., Sun, Y. 2007. Are Chinese loess deposits essentially continuous? Geophysical Research Letters 34, L17306, doi: 10.1029/2007GL030591.

Chapter 3*

Reconstruction of the Missing Link between Global Cooling and Mammalian Transformation across the Eocene-Oligocene Boundary in the Continental Interior of Asia

3.1 Introduction

As recorded by a large-scale positive marine benthic $\delta^{18}O$ anomaly and gradual drops in sea level, a dramatic decrease of deep-sea temperature from "greenhouse" to "icehouse" conditions occurred across the Eocene-Oligocene boundary (EOB) 33.9 Ma (Miller et al., 1987; Zachos et al., 2001; Coxall et al., 2005; Tripati et al., 2005). At the same time, major continental cooling in North America, Europe, and Asia is attributed to the Eocene-Oligocene transition (EOT) (Meng and Mckenna, 1998; Grimes et al., 2005; Gale et al., 2006; Zanazzi et al., 2007). Such global scale climate change during the EOT caused the most significant mammal biotic reorganization since the extinction at the end of the Cretaceous period (Meng and Mckenna, 1998; Kraatz and Geisler, 2010). Eocene–Oligocene land mammalian fossils in different parts of the world clearly demonstrate the Asian *Mongolian Remodeling* and the European *Grande Coupure* in which medium-sized communities of perissodactyl were abruptly replaced by small-sized rodent/lagomorph-dominant faunas like rodents and lagomorphs (Meng et al., 1998; Kraatz and Geisler, 2010). The age of the *Mongolian Remodeling*, however, is still not precise.

* A version of this chapter will be submitted to the journal of ***Palaeogeography Palaeoclimatology Palaeoecology***, 2011.

A broad pattern of aridification across the late Eocene and early Oligocene within central Asia was recently reported in Mongolia (Kraatz and Geisler, 2010) and the northeast Tibetan Plateau (Dai et al., 2006; Dupont-Nivet et al., 2007, 2008). In the Xining Basin of northeastern Tibet, the authors of Dupont-Nivet et al. (2007, 2008) built an age model based on magnetostratigraphy and correlations between local/regional pollen records and a marine oxygen isotope reference curve to perform their paleoenvironmental reconstructions. However, the mammalian fossils found in the upper part of the described section correspond to the late Oligocene, and late Eocene to early Oligocene fossils are not found in Xining as shown earlier by magnetostratigraphic dating (Dai et al., 2006). Therefore, other studies are required to clarify timing of the EOT in Asia. Kraatz and Geisler (2010) reported on several sections across the EOT from Mongolia. Their age model was based on a magnetostratigraphic compilation of a few short sedimentary sequences that sometimes contained only one or two normal/reversal polarity zones. Although the authors described faunal transitions during the EOT, late Eocene faunas were not found. We expect that both late Oligocene and early Eocene faunas are preserved in other sections in continental Asia; such faunas would confirm the Mongolian timing of the EOT and determine the lower boundary of the transition.

To better understand the character and timing of the faunal modification in Asia compared to Europe, as well as differences and similarities between continental and oceanic climate changes around the Eocene-Oligocene boundary—an age of late Eocene to early Oligocene faunal transformations across the EOT—we studied the Burqin section (northern Junggar Basin) in central Asia. The section is situated 2,000 km to the west of the Mongolian section described

by Kraatz and Geisler (2010). Our section could be compared to sections from similar time intervals in Europe and Mongolia in order to specify a linkage to faunal turnover during the EOT (Wu et al., 2004; Ye et al., 2005; Ni et al., 2007).

All stratigraphic layers in the Burqin section are horizontal and there are no tectonic deformations in the region; that makes the Burqin section one of the key sections to study the EOT and the EOB in Asia. In this paper we base the timing of terrestrial cooling and aridification on our magnetostratigraphic dating of mammalian fauna findings in the Burqin section.

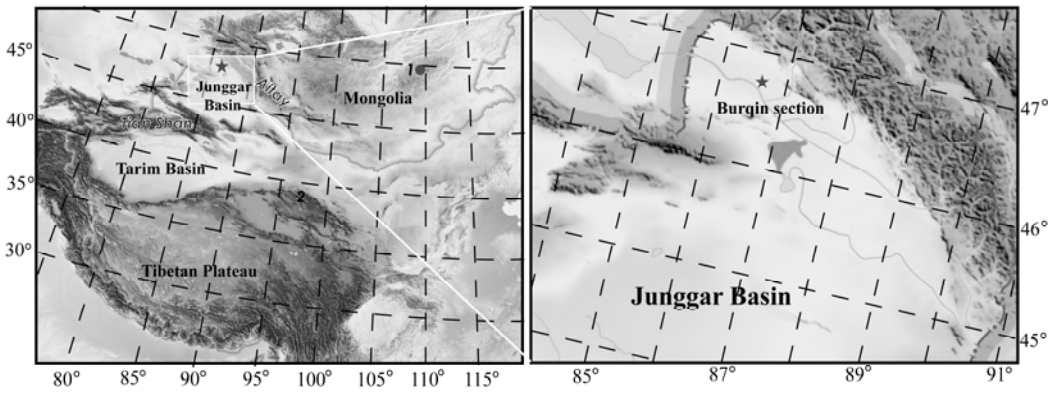

Figure 3.1 (A) Study area in Asia. (B) Location of the Junggar basin and Burqin section.

3.2 Mammalian fossils of the Burqin section

The terrestrial Tertiary strata on the northern bank of the Irtysh River near Burqin City (Figure 1) consist of the lower segment of the Irtysh River Formation—a set of bright colors of rusty-yellow, purplish red on the weathered surface sediments—and the upper segment of the Keziletuogayi Formation—a set of yellowish-green sandstone with variegated green mudstones (Ye et al., 2005; Ni et al., 2007). All layers are horizontal and there are no signs of sedimentary

discontinuity or tectonic deformation in the study area. Three mammalian fossil assemblages across the EOB have been found in the Keziletuogayi Formation in the Burqin section (Wu et al., 2004; Ye et al., 2005; Ni et al., 2007). The first assemblage was discovered in a 70 mm thin layer of black manganese siltstone in grayish green mudstone at a depth of 58 m (Figure 2). These findings are described in detail by Ye et al. (2005) and Ni et al. (2007). Six species representing four families include Cadurcodon cf. C. *ardynensis*, Amynodontidae gen. et sp. indet., *Gigantamynodon giganteus*, Indricotheriinae gen. et sp. indet., Rhinocerotidae gen. et sp. indet., and Brontotheriidae gen. et sp. indet.; all are perissodactyls and the assemblage is similar to the Khoer-Dzan and Ergilin faunas of Mongolia (Wu et al., 2004; Ye et al., 2005; Ni et al., 2007). The apparent lack of forest related species like euprimates, chiropterans, and plesiadapiformes suggests an absence of dense forest in Burqin during the study interval. *Rhynchosia* and *Elaeagnus* pollen findings and evidence of perissodactyl-dominant mammals indicate a warm subtropical climate (Ye et al., 2005).

The second mammalian assemblage includes fossils found at a depth of 45 m in a 1.7 m layer of brown mudstone in between green sandstone strata (Figure 2) (Ye et al., 2005; Ni et al., 2007). Fossils collected from the Burqin section and two other neighboring localities of the same stratigraphic level represent 13 species from 7 mammalian genera; all are mammals similar in size to *Hyaenodon* sp. and *Desmatolagus* sp. and comparable to the early Shandgolian faunas (Ye et al., 2005; Ni et al., 2007). Such a critical change in mammalian assemblage indicates a faunal turnover from perissodactyl-dominant mammals to rodents and lagomorphs along the cross section.

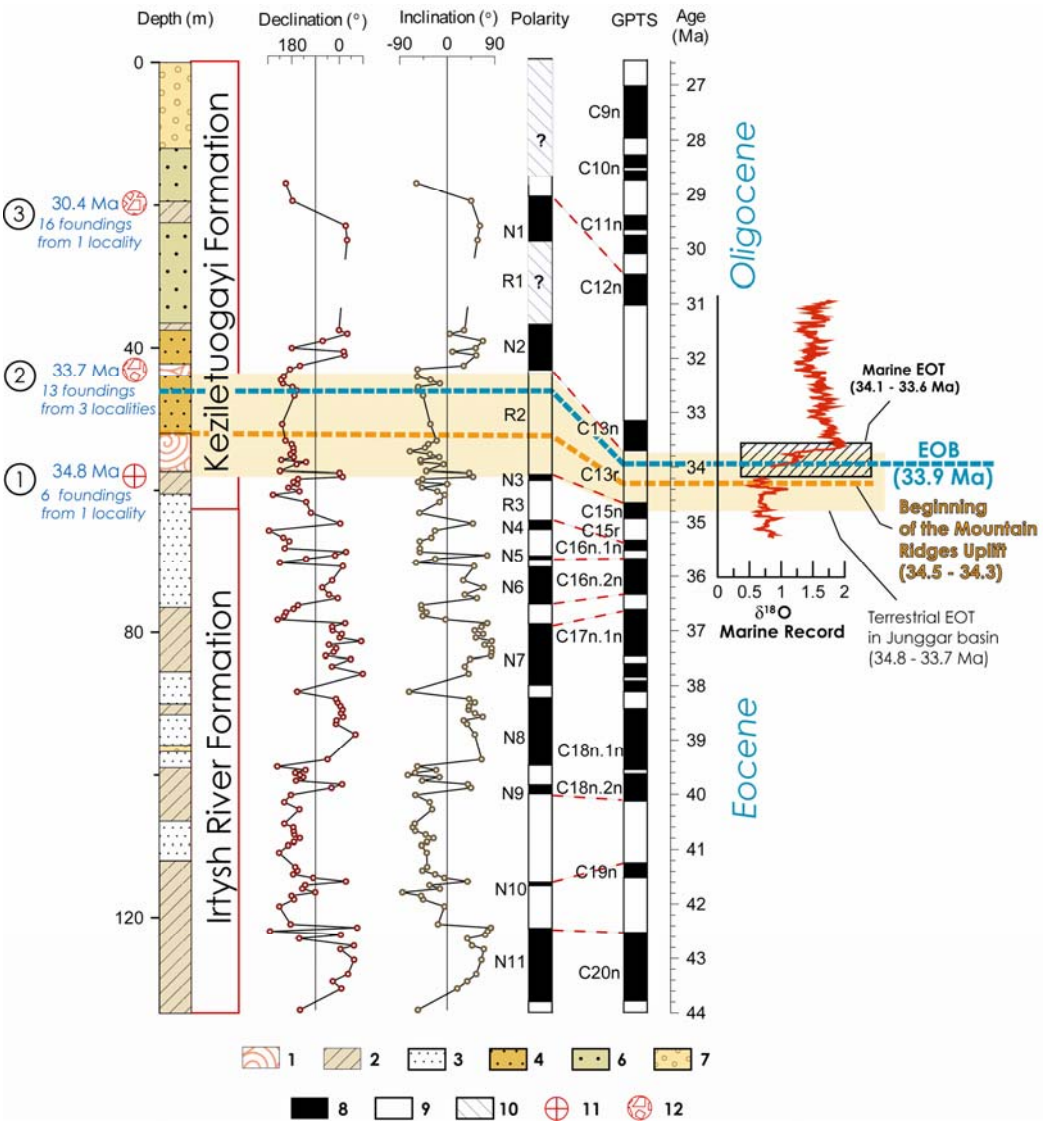

Figure 3.2 Detailed magnetostratigraphy of the studied section and its correlation with the GPTS of Cande and Kent (1995). EOB is at 33.9 Ma (Gradstein et al., 2004). Marine oxygen isotope curve is from Coxall et al (2005). Terrestrial EOT in the Junggar Basin is constricted in this study.

1 – mudstone, 2 – siltstone, 3 – fine sandstone, 4 – intermediate size sandstone, 5 – coarse sandstone, 6 – conglomerate, 7 – normal polarity interval, 8 – reversed polarity, 9 – uncertain polarity, 10 – perissodactyl-dominant mammalian fossils, 11 – rodent/lagomorph dominant fossils.

The third mammalian fossil assemblage, collected at a depth of 65 m of green mudstone, also reflects a faunal turnover. Its dominant small-sized

mammals included 16 species similar in size to *Palaeoscaptor* cf. *P. acridens* and *Tupaiodon* cf. *T. Morrisi*, and analogous to the Shandgolian from Mongolia (Meng and Mckenna, 1998; Ye et al., 2005; Kraatz and Geisler, 2010).

3.3 The magnetostratigraphic result and the age model

We sampled a 128 m long Burqin sedimentary section that corresponds to the Irtysh River (lower part of the section) and Keziletuogayi (upper part of the section) formations at the north bank of the Irtysh River. Paleomagnetic sampling was performed approximately every 0.5 m. The uppermost stratum of the section was dominated by a massive grayish-white fluvial conglomerate which made paleomagnetic sampling unfeasible. Therefore our sampling began from the grayish lacustrine sandstone and mudstone layers beneath the conglomerate layer (Figure 2). There was a general trend toward coarser particles upward to the top of the section. At a depth of 26–37 m, the lithology of the Keziletuogayi Formation was dominated by coarse, yellowish sandstone which also did not yield to paleomagnetic analysis. Thus there is no paleomagnetic data for these two stratigraphic intervals. In the laboratory we thermally demagnetized 178 samples from different depth intervals, applying 12–16 temperature steps up to 690°C and measuring the natural remanent magnetization (NRM) after every step. Our paleomagnetic analysis yielded reliable primary remanent magnetization directions from 126 samples (details are published in Zhang et al., 2010). We identified 11 normal polarity and 11 reversed polarity intervals. The detailed magnetostratigraphy was determined by the declination and inclination correlation to the geomagnetic polarity time scale (GPTS) of Cande and Kent (1995). Recent paleontological constraints suggest that perissodactyl-dominant mammals (first assemblage) were characteristic of the late Eocene and that the dominant species

turned over to rodents and lagomorphs (second and third assemblages) in the early Oligocene; this data suggests that the Eocene-Oligocene boundary is between the first and second assemblages (Wu et al., 2004; Ye et al., 2005; Ni et al., 2007). We started matching our polarity scale to the GPTS in the most evident intervals of reverse polarity at 40–55 m, R2 and R3, to the long reverse polarity chrons C13r and C15r, separated by a shorter normal polarity chron C15n (Figure 2). Then we matched other polarity intervals further down and up the section. Although there are alternative options for matching the GPST, our model in Figure 2 provides the most reasonable fit that is in agreement with (1) the mammalian fossil assemblages of the Keziletuogayi Formation and (2) the increase in sedimentary grain size from fine grain sediment at the bottom of the section to medium and course sandstone at the top of the section. This indicates that the rate of sedimentation increased from 0.76 cm/kyr to 0.98 cm/kyr. Such an increase in sedimentation rate may signify acceleration of mountain uplift toward the north of the sampling locality (Altay Mountains). The uplift may be a result of the Tibetan uplift and subsequent shortening of the distance between India and northern Eurasia.

The sedimentation rate in our section is much lower than the 2.2 cm/kyr rate in the Xining Basin during the Eocene/Oligocene epochs (Dai et al., 2006). Our study locality was far from northeastern Tibet where the Xining Basin section is situated. Therefore the Xining section was much more affected by the uplift of the Tibet Plateau ~38 Ma (Dupont-Nivet et al., 2008). Our age model enables us to calculate an expected increase in sedimentation rate (Figure 3). Linear interpolation between the magnetic chrons yields ages of 34.8 and 33.7 Ma, respectively, for the first and second faunal assemblages. The third assemblage is

right above the N1 normal polarity of our sequences and corresponds to an age of 30.4 Ma.

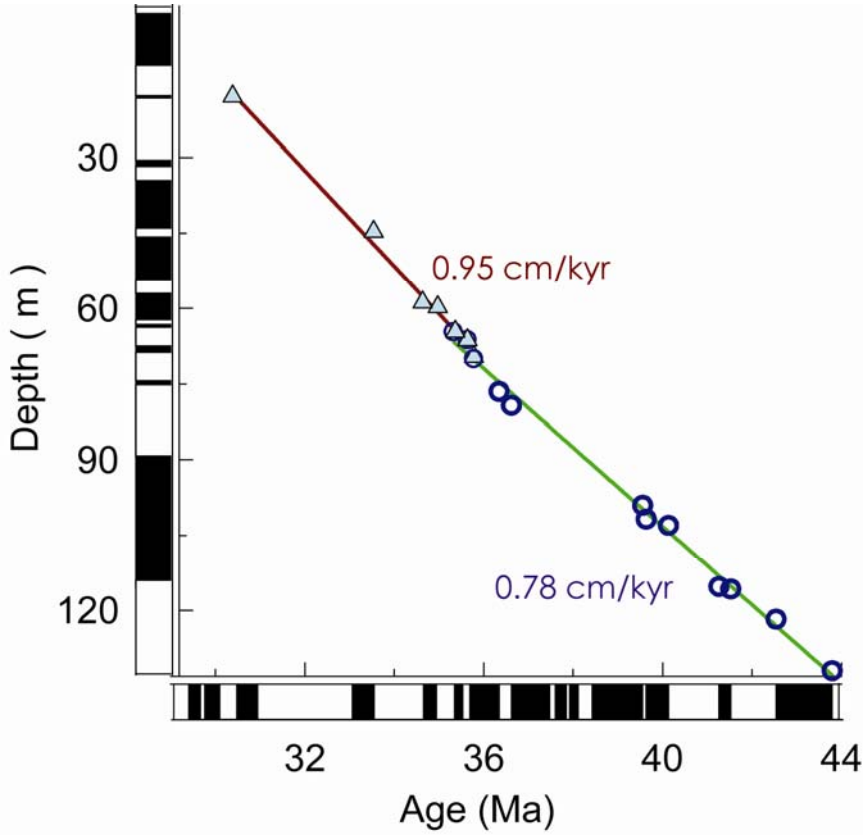

Figure 3.3 Stratigraphic level in meters versus age according to magnetostratigraphic correlation to the GPTS at the Burqin section. Sedimentation rate of 0.78 cm/kyr and 0.95 cm/kyr is shown near fine grain (dashed line) and coarser grain (solid line) sediment intervals in the section.

3.4 Discussion

The fossil assemblage from the Burqin section provides paleontological evidence for the onset of important environmental change across the EOT that is consistent with the global climate shift characterized by a gradual decrease in deep-sea temperature (Coxall et al., 2005; Tripati et al., 2005) recorded in the marine oxygen isotope curve (Figure 2). An average low sedimentation rate of

0.84 cm/kyr in the section and an absence of regional tectonic rotations inside the basin during the end of the Eocene – beginning of the Oligocene (Zhang et al., 2010) confirm that there were no considerable stratigraphic discontinuities or destructions before or after the EOB in the studied section.

The prominent terrestrial biotic reorganization in central Asia has been recognized and named the Mongolian Remodeling (Meng and McKenna, 1998). The Mongolian Remodeling is characterized by a shift from Eocene perissodactyl-dominant faunas to Oligocene rodent/lagomorph-dominant faunas. Recently, Kraatz and Geisler (2010) demonstrated that the first post-Mongolian Remodeling faunas appeared as Hsandagolian EALMA found in the Hsanda Gol Formation in Mongolia at 33.3 Ma. The first finding of rodent/lagomorph-dominant mammals in our section was located at 33.7 Ma (Figure 2) which indicates that these mammals should appear in the study area and possibly the whole of central Asia at least 0.5 Myrs earlier than was considered based on recent Mongolian findings.

We do not have evidence of a mixture of perissodactyl and rodent/lagomorph faunas in Burqin. All 13 findings from 3 different localities in Burqin indicate only rodent/lagomorph faunas. This could be interpreted as a complete disappearance of perissodactyls in the Burqin Basin and perhaps in central Asia by 33.7 Ma. It means that the mixture of both types of fauna could have appeared earlier than our pure rodent/lagomorph-dominant mammal findings from 33.7 Ma, but later than our pure perissodactyl faunas findings from 34.8 Ma.

Fossils show that mammals in the north Junggar Basin and Mongolia lived about the same latitude. The climate of the central Asian Junggar Basin between 34.8 Ma and 33.7 Ma turned from a warm environment that favored

perissodactyls to cool conditions that supported rodents and lagomorphs. Our study results enable us to estimate the age of the terrestrial EOT in central Asia more accurately and are consistent with the findings in Mongolia.

Dupont-Nivet et al. (2007) demonstrated firmly that the aridification in central Asia at the EOB was a result of global climatic cooling. The major Tibetan uplift occurred a little earlier (~38 Ma) based on the Xining Basin data (Dupont-Nivet et al., 2008). Gradual change to a higher sedimentation rate, approximately at the EOB in our section, suggests that uplift of the Altay Mountains north of the Junggar Basin could have occurred due to shortening of the distance between India and northern Eurasia. Gravel stratum in the upper part of the study section indicates that a large energy river input to the Barquin site ancient lake corresponds to ~30 Ma. It implies that the mammalian reorganization occurred as a result of global cooling and Asian aridification as shown by Dupont-Nivet et al. (2007) and not as a result of a very slow Altay Mountains uplift. The delayed Altay uplift, in conjunction with the Tibetan Plateau uplift, could have accelerated the aridification process in the Junggar Basin by further cutting off the basin from atmospheric currents that brought moisture to the region. Our model is fairly consistent with Dai et al. (2006) who demonstrated a sudden increase in sedimentation rates in the Xining Basin between 34.5 and 31.0 Ma (from 1.8 cm/kyr before 34.5 Ma to 4.1 cm/kyr, and back to 2.3 cm/kyr after 31.0 Ma). Our section sedimentation rate increased after ~34.5 Ma although it did not drop back after 31.0 Ma as shown by Dai et al. (2006). At the same time, it is noticeable in Figure 10 of Dai et al. (2006) that the major increase in sedimentation rate occurred at ~34.5 Ma. This is consistent with the interpretation in Dupont-Nivet et al. (2007) for the same sections, where the authors showed only one substantial lithological change at ~118 m (~380 m in the description in Dai et al., 2006).

The uplift of Tibet and retreat of the Paratethys epicontinental sea triggered aridification of the continental environment (Graham et al., 2005; Harris, 2006; Rowley and Currie, 2006; Zhang et al., 2007; Dupont-Nivet et al., 2007, 2008). Aridification, however, began at least 3 Myr before the EOT in Asia (Dupont-Nivet et al., 2008). Therefore, global cooling could be the main reason for species' extinctions and appearances. Reorganization of faunal compositions of the Junggar Basin in a short time interval, most likely between 34.8 and 33.7 Ma, was followed by a long period of stability of new faunal communities. This change fits with marine oxygen isotope data that demonstrate that the marine EOT (34.1–33.6 Ma) occurred around the EOB (33.9 Ma). The terrestrial EOT in the Junggar Basin and central Asia occurred about the same time interval (34.8–33.7 Ma). It is possible that the terrestrial EOT in the Junggar Basin could have terminated a little earlier (33.7 Ma) than the marine EOT (33.6 Ma), as central Asia experienced both cooling and aridification around the EOB, conditions that were rougher for perissodactyl faunas and accelerated their replacement with rodent/lagomorph faunas by 33.7 Ma.

Bibliography

Cande, S.C., and Kent, D.V., 1995, Revised calibration of the geomagnetic polarity time scale for the Late Cretaceous and Cenozoic: Journal of Geophysical Research, v. 100, p. 6093–6095, doi: 10.1029/94JB03098.

Coxall, H.K., Wilson, P.A., Palike, H., Lear, C.H., and Backman, J., 2005, Rapid stepwise onset of Antarctic glaciation and deeper calcite compensation in the Pacific Ocean: Nature, v. 433, p. 53–57, doi: 10.1038/nature03135.

Dai, S., Fang, X., Dupont-Nivet, G., Song, C., Gao, J., Krijgsman, W., Langereis, C., and Zhang, W., 2006, Magnetostratigraphy of Cenozoic sediments from the Xining Basin: Tectonic implications for the northeastern Tibetan Plateau: Journal of Geophysical Research, v. 111, B11102, p. doi: 10.129/2005JB004187.

Dupont-Nivet, G., Krijgsman, W., Langereis, C.G., Abels, H.A., Dai, S., and Fang, X., 2007, Tibetan plateau aridification linked to global cooling at the Eocene–Oligocene transition: Nature, v. 445, p. 635–638, doi: 10.1038/nature05516.

Dupont-Nivet, G., Hoorn, C., and Konert, M., 2008, Tibtan uplift prior to the Eocene-Oligocene climate transition: Evidence from pollen analysis of the Xining Basin: Geology, v. 36, p. 987-990, doi: 10.1130/G25063A.1.

Gale, A.S., Huggett, J.M., Pälike, H., Laurie, E., Hailwood, E.A., and Hardenbol, J., 2006, Correlation of Eocene–Oligocene marine and continental records: Orbital cyclicity,

magnetostratigraphy and sequence stratigraphy of the Solent Group, Isle of Wight, UK: Geological Society of London Journal, v. 163, p. 401–415, doi: 10.1144/0016-764903-175.

Graham, S.T., Chamberlain, C.P., Yue, Y., Ritts, B.D., Hanson, A.D., Horton, T.W., Waldbauer, J.R., Poage, M.A., and Feng, X., 2005, Stable isotope records of Cenozoic climate and topography: Tibetan Plateau and Tarim Basin: American Journal of Science, v. 305, p. 101–118, doi: 10.2475/ajs.305.2.101.

Grimes, S.T., Hooker, J.J., Collinson, M.E., and Mattey, D.P., 2005, Temperatures of the late Eocene to early Oligocene freshwaters: Geology, v. 39, p. 189–192, doi: 10.1130/G21019.1.

Harris, N.B.W., 2006, The elevation history of the Tibetan Plateau and its implications for the Asian monsoon: Palaeogeography, Palaeoclimatology, Palaeoecology, v. 241, p. 4–15, doi: 10.1016/j.palaeo.2006.07.009.

Kraatz, B. P., and Geisler, J. H., 2010, Eocene-Oligocene transition in Central Asia and its effects on mammalian evolution: geology, v. 38, p. 111-114, doi: 10.1130/G30619.1.

Miller, K.G., Fairbanks, R.G. and Mountain, G. S., 1987, Tertiary Oxygen isotope synthesis, sea level history, and continental margin erosion: Paleoceanography, v. 2, p. 1–19.

Meng, J., and McKenna, M.C., 1998, Faunal turnovers of Paleogene mammals from the Mongolian plateau: Nature, v. 394, p. 364–367, doi: 10.1038/28603.

Ni, X. J., Meng, J., Ye, J. and Wu, W. Y., 2007, A new Early Oligocene peradectine marsupial (Mammalia) from the Burqin region of Xinjiang, China: Naturwissenschaften, v. 94, p.237–241, DOI 10.1007/s00114-006-0182-2.

Rowley, D.B., and Currie, B.S., 2006, Palaeoaltimetry of the late Eocene to Miocene Lunpola basin, central Tibet: Nature, v. 439, p. 677–681, doi: 10.1038/nature04506.

Tripati, A., Backman, J., Elderfield, H., and Ferretti, P., 2005, Eocene bipolar glaciation associated with global carbon cycle changes: Nature, v436, p. 341-346, doi: 10.1038/nature03874.

Wu, W., Meng, J., Ye, J., and Ni, X., 2004, Propalaeocastor (Rodentia, Mammalia) from the Early Oligocene of Burqin Basin, Xinjiang: Am Mus Novit, v. 3461, p. 1–16.

Ye, J., Meng, J., Wu, W, and Ni, X., 2005, Lithological and biostratigraphic sequence across the Eocene-Oligocene boundary in Burqin of Xinjiang: Vertebrata PalAsiatica, v. 43, p. 49–60.

Zachos, J.C., Pagani, M., Sloan, L., Thomas, E., and Billups, K., 2001, Trends, rhythms, and aberrations in global climate 65 Ma to present: Science, v. 292, p. 686–693, doi: 10.1126/science.1059412.

Zanazzi, A., Kohn, M.J., MacFadden, B.J., and Terry, D.O., Jr., 2007, Large temperature drop across the Eocene–Oligocene transition in central North America: Nature, v. 445, p. 639–642, doi: 10.1038/nature05551.

Zhang, Z., Wang, H., Guo, Z., and Jiang, D., 2007, What triggers the transition of alaeoenvironmental patterns in China, the Tibetan Plateau uplift or the Paratethys Sea retreat?: Palaeogeography, Palaeoclimatology, Palaeoecology, v. 245, p. 317–331, doi: 10.1016/j.palaeo.2006.08.003.

Zhang, R., Kravchinsky, V. A., Blanco, D., Yue, L., 2010, Paleomagnetism and tectonic rotation in the Northern Junggar basin, Northwest China: Geophysical Journal International, in press.

Chapter 4*

New paleomagnetic poles for the northern Junggar Basin, northwest China, about 40 and 20 Ma: Evidence of intracontinental shortening between Junggar and Europe after 20 Ma

4.1 Introduction

Paleomagnetic data obtained on Tertiary formations from central Asia provide new evidence for crustal deformation of the Asian continent since the collision between India and Eurasia (e.g., Gilder et al., 1993, 2001; Dupont-Nivet et al., 2002, 2003; Huang et al., 2004, 2006; Hankard et al., 2007). However, paleoreconstructions of the Asian continent and models of crustal deformation remain controversial because of the rarity of well-dated igneous rocks and sediments in many critical areas. Previous studies described a 20–30° Tertiary inclination anomaly in Asia associated with the shallower inclinations when compared with the expected inclinations calculated from the reference apparent polar wander path (APWP) for Europe (Thomas et al., 1993, 1994; Chauvin et al., 1996; Cogné et al., 1999; Gilder et al., 2001, 2003; Tan et al., 2003; Huang et al., 2004, 2006). In the Cretaceous, northward drift of central Asian continental blocks could explain the shallower than expected inclinations that result in a larger than 2000 km intercontinental shortening between the Tarim block and Siberia (Cogné et al., 1999; Gilder et al., 2001; Hankard et al., 2007). Local magnetic field anomalies or global anomalies (Si and Van der Voo, 2001; Van der

* A version of this chapter is submitted to the journal of Geophysical Journal Intrnational, 2011.

Voo and Torsvik, 2001), a syndepositional inclination shallowing and postdepositional compaction-induced shallowing (Gilder et al., 2001; Tan et al., 2003; Narumoto et al., 2006), and several other causes are often used to explain the observed inclination shallowing.

Recently, Hankard et al. (2007) summarized an alternative hypothesis for inclination shallowing in central Asia during the Cenozoic based on the new poles they derived from Mongolian and Siberian volcanic rocks. They suggested that approximately 40 Ma the Siberian craton and Amuria block were located 1450 ± 250 km to the south of their expected paleolatitudes from the European APWP of Besse and Courtillot (2002). Around 20 Ma, the difference decreases to 850 ± 200 km and apparently vanishes (20 ± 200 km) by 13 Ma.

To further examine the new hypothesis for the inclination shallowing anomaly and to perform paleoreconstructions, we studied two well-dated sedimentary sections in the north of the Junggar Basin. The magnetostratigraphy aspects of the sections were discussed in Zhang et al. (2007) and Zhang et al. (2011).

4.2 Geological setting and sampling

The Junggar Basin, formed in late Paleozoic, Mesozoic, and Cenozoic, is a large-scale piled sedimentary basin bounded by the Tian-Shan Mountains to the south and the Altay Mountains to the north. The thickness of sediments varies from 1500–4600 m in the south to 100–800 m in the north. Bedding orientation is usually horizontal in the northern parts of the basin and folded and steep in the southern periphery of the basin where it varies distinctly from 30° to 90° toward the south and north.

We sampled two sections situated in the north of the Junggar Basin (Figure 4.1). The bedding orientation is horizontal in both sections. There is no tectonic tilting or folding in the study area, therefore the fold test could not be performed. The Tieersihabahe section (25 to 17 Ma, 46.7°/88.5°) comprises, from bottom to top, the Ulunguhe, Suosuoquan, and Kekemaideng Formations described by Ye et al. (2001, 2003). The Ulunguhe Formation contains yellowish mudstones to sandstones with two neighbored fossil-rich layers. The Suosuoquan Formation, dominated by reddish mudstones to siltstones with interbedded thin sandstones, conformably overlies the Ulunguhe Formation. The Kekemaideng Formation consists mainly of gray or white sandstones with interbedded conglomerates and green siltstones. The upper part of the Kekemaideng Formation consists of layers of brown to yellowish sandstones and conglomerates.

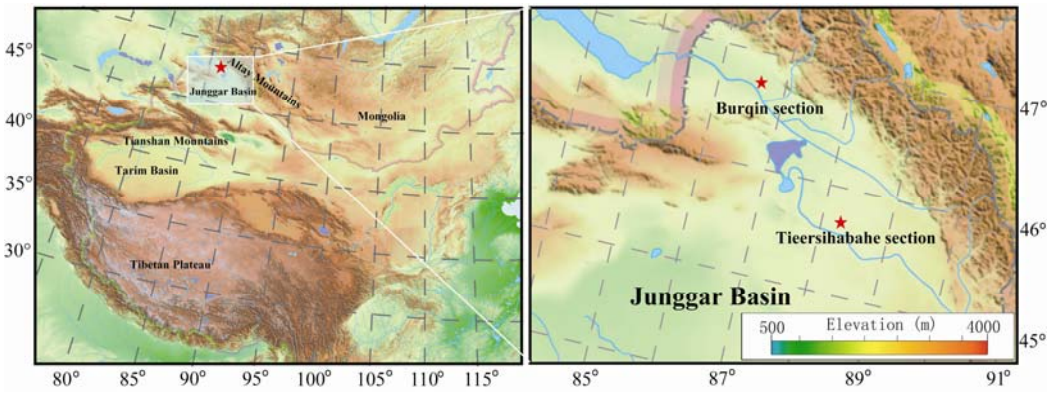

Figure 4.1 Simplified map of central Asia and the Junggar Basin with sampling localities (red starts) described in the text.

The strata of the Burqin section (44 to 25 Ma, 48.0°N/86.7E°) are known as the Irtysh River Formation and the Keziletuogayi Formation (Ye et al., 2005). The Irtysh River Formation is a set of sediments in bright colors of rusty-yellow and purplish red on the weathered surface. There are mainly brown mudstone, siltstone, and sandstone layers in the lower part of the Irtysh River Formation; the

upper part of the Formation is primarily yellowish to red sandstone. The Keziletuogayi Formation consists mainly of yellowish sandstones with green mudstones. The outcrop thicknesses of the studied sections are 192 m and 128 m in Tieersihabahe and Burqin, respectively. Hand block samples were collected at about 50 cm intervals yielding 339 and 178 sampling levels, for Tieersihabahe and Burqin, respectively. The blocks were orientated insitu using a magnetic compass and then cut in the laboratory to 2 × 2 × 2 cubic cm specimens for further paleomagnetic measurements.

4.3 Laboratory treatment

4.3.1 Magnetic Mineralogy

The samples were subjected to temperature-dependent magnetic susceptibility (MS) experiments from room temperature to 700°C (in an argon atmosphere to prevent oxidation) using an AGICO KLY-3 Kappabridge susceptibility meter coupled with a CS-3 high-temperature furnace.

4.3.2 Magnetic remanence

Specimens from the Burqin (178) and Tieersihabahe (359) sections were subjected to stepwise thermal demagnetization using the following stepwise heating routine: (i) 25–50°C steps from room temperature to 585°C and (ii) 10–25°C steps up to 690°C. A second sample from the same hand block was demagnetized if the first yielded an unstable result or if a polarity interval was defined by only one sample. Magnetic remanences were measured with a three-axis 2G-entrprise cryogenic magnetometer housed in a magnetic shield at the Paleomagnetism Laboratory at the Institute of Geology and Geophysics (Chinese

Academy of Sciences, Beijing) and at the Laboratory of Paleomagnetism and Petromagnetism (Faculty of Science, University of Alberta).

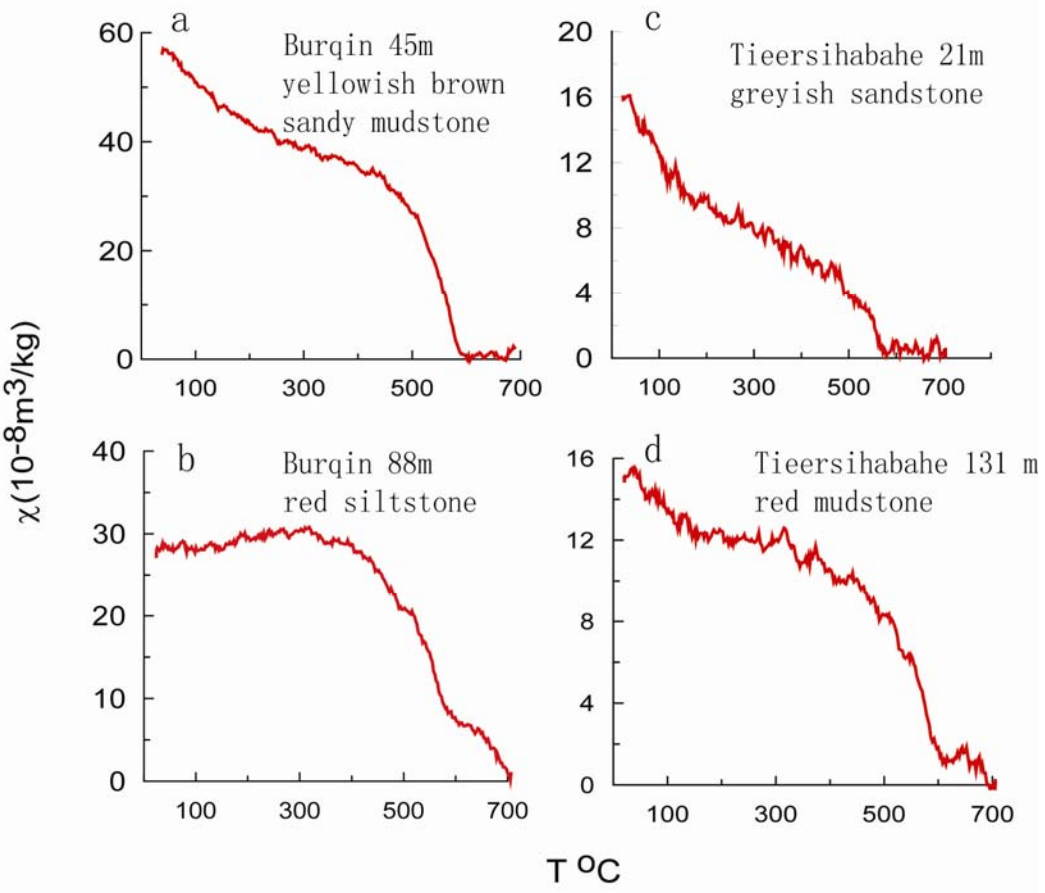

Figure 4.2 Temperature-dependent magnetic susceptibility curves for representative samples from the Burqin and Tieersihabahe sections. Magnetite and hematite are the main carriers of remnant magnetization in both localities.

4.4 Results

Figure 4.2 contains representative results of the temperature-dependent magnetic susceptibility (MS) measurements of specimens from the Burqin and Tieersihabahe sections of the Junggar Basin. The measurements show a steep drop in MS values from 450–585°C for all samples; this is characteristic of magnetite, the dominant contributor to magnetic susceptibility. Some samples from the

redbed layers underwent a second decrease in MS in the range of 600–690°C (Figures 4.2b and 4.2d), consistent with the presence of hematite. Loss of susceptibilities between 300 and 450°C, observed in Figures 4.2a, 4.2b, and 4.2c, is generally caused by the transformation from maghemite to hematite. Other moderate inflections below 200°C (Figures 4.2a, 4.2c, 4.2d) were possibly caused by a paramagnetic component.

Figure 4.3 shows representative orthogonal demagnetization diagrams (Zijderveld, 1967). Many samples possessed two magnetic components with variable but often north and down directions (in-situ coordinates) at low temperature (generally 20–200°C) that generally fit present day geomagnetic field directions although is scattered. We interpret this component as the present day overprint.

High temperature components (HTC) are usually unblocked at temperatures of 585°C, and normally decay toward the origin on orthogonal diagrams; this behavior is typical for magnetite. However in samples from the red layers, the original natural remanent magnetization (NRM) direction remained stable from 585°C to 690°C (Figures 4.3a, 4.3d, 4.3f), a characteristic of samples containing hematite. Samples with unblocking temperatures that corresponded to hematite had typical temperature dependent magnetic susceptibilities (examples are B-88m and T-131m in Figures 4.2b and 4.2d). When both magnetite and hematite were present in the same sample, the HTC directions did not differ in the 500–585°C and 610–690°C temperature ranges of the demagnetization spectra (Figures 4.3a, 4.3d, 4.3f). It confirms that magnetite and hemitate are the main magnetic minerals that carry primary magnetization directions.

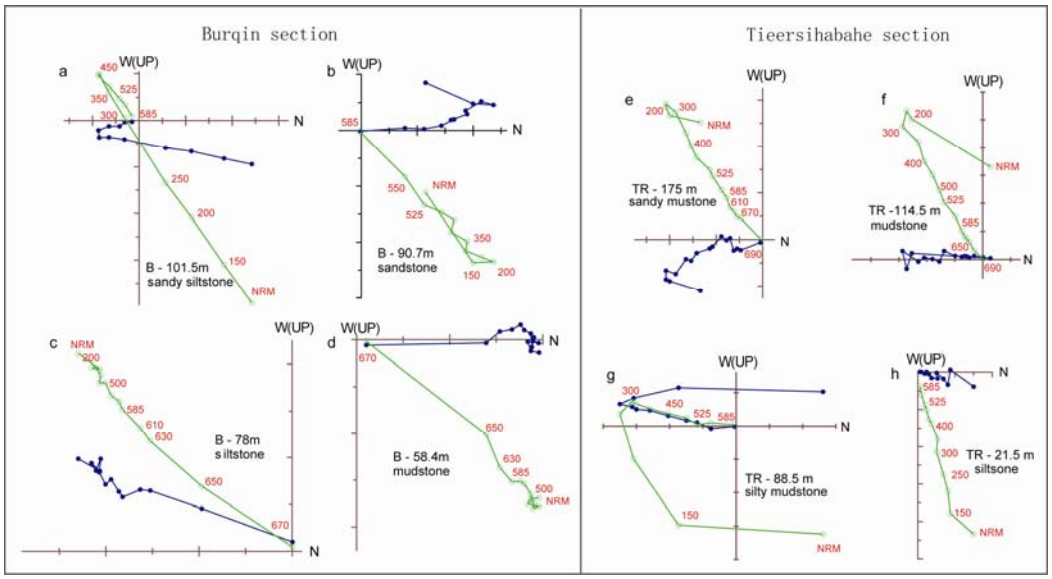

Figure 4.3 Representative orthogonal vector projections of the stepwise thermal demagnetization of the natural remanent magnetization for both studied localities. Demagnetization steps are in °C in all plots; open and solid circles represent vector endpoints projected onto the vertical and horizontal planes, respectively. Depth of the sample in meters is given from the top of the sampled section.

Among the 178 demagnetized samples from the Burqin section: 126 samples had linear magnetic components that decayed to the origin; 49 samples had positive HTC inclinations and corresponded to normal polarity intervals; 47 samples had negative inclinations (reverse polarity intervals); and 30 samples had directions that deviated more than 60° from the overall mean, a characteristic expected from samples that have recorded a transitional or unstable geomagnetic field. In the Tieersihabahe section: 224 samples out of the 359 possessed a magnetic component that decayed toward the origin; 62 samples presented normal polarity intervals; 106 samples presented reverse polarity intervals; and 56 samples had unstable magnetizations with weak NRM intensities or recorded a transitional geomagnetic field. The mean paleomagnetic directions are listed in Table 4.1.

Table 4.1 Mean paleomagnetic directions for high temperature component of the study localities.

Data set	N	D(°)	I (°)	k	α_{95}(°)
Burqin (44-25 Ma) 47.8°N/86.7°E					
Normal	49	357.9	59.8	12.0	6.1
Reverse	47	181.1	-54.4	15.2	5.5
Mean	96	359.6	57.1	13.3	4.1
*White-grey sandstone /siltstone	55	4.1	53.9	13.9	5.3
*Redbed mudstone/siltstone	42	354.0	60.7	12.9	6.4
Tieersihabahe (25-17 Ma) 46.7°N/88.5°E					
Normal	62	4.3	58.8	11.7	5.5
Reverse	106	177.4	60.1	12.4	4.1
Mean	168	0.1	59.7	11.8	3.3
*White-grey sandstone /siltstone	36	356.4	58.0	9.7	8.1
*Redbed mudstone/siltstone	132	1.0	60.1	13.0	3.5

N: number of samples. D: magnetic declination. I: magnetic inclination. k: precision parameter, α_{95}: confidence cone of radius of 95% probability.
*Directional results for the redbed (siltstone and mudstone) and white-grey (mudstone and sandstone/siltstone) data set. Analysis is applied to further explore the primary characteristic of the high temperature component.

Based on our temperature-dependent magnetic susceptibility and magnetic remanence demagnetization results, we conclude that magnetite and hematite are the dominant magnetic carriers in the high temperature components of the Burqin and Tieersihabahe sections. These magnetic carriers have identical HTC directions for all samples that contain magnetite only or for samples in which magnetite and hematite coexist (Figure 4.3).

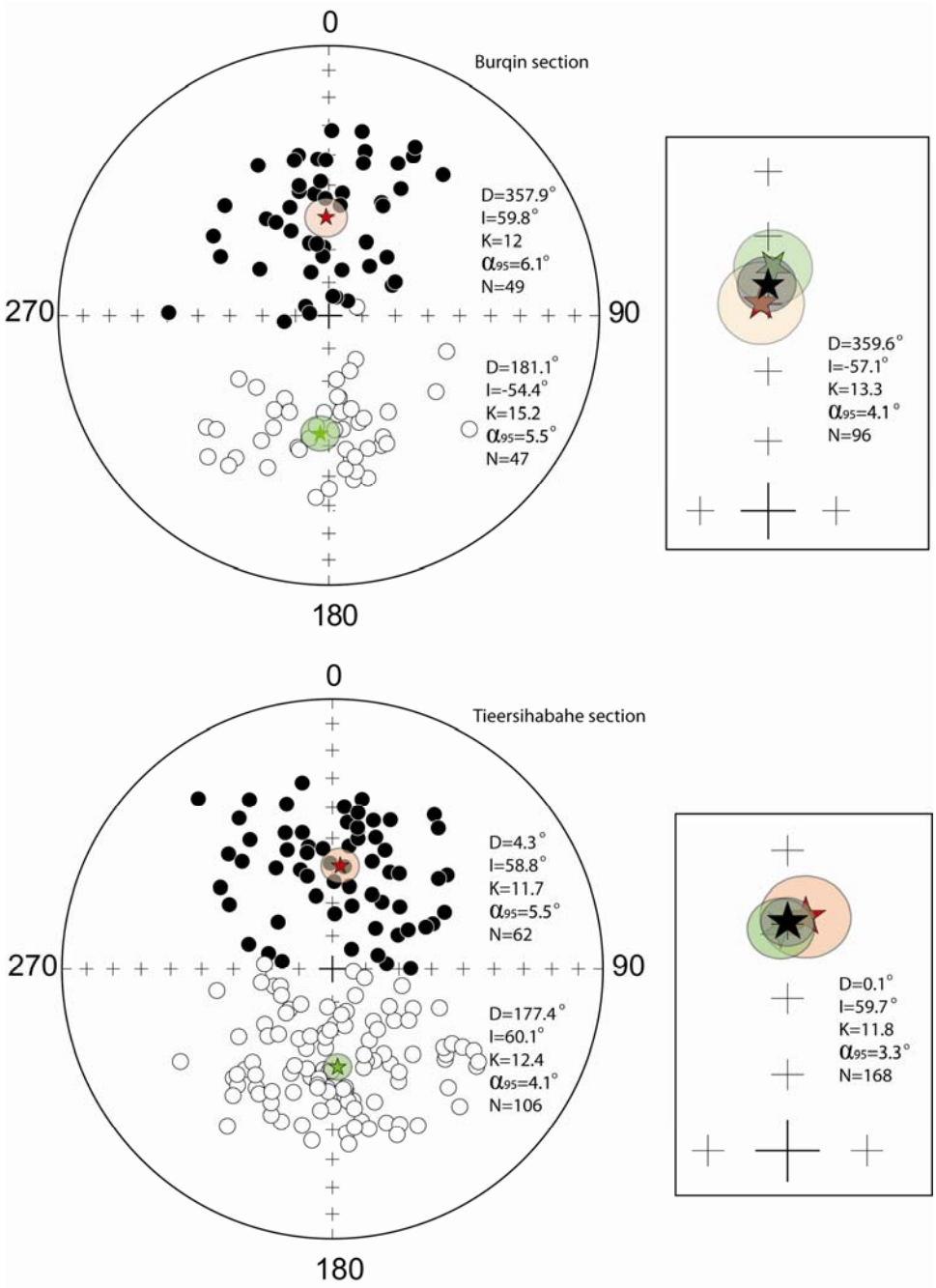

Figure 4.4 Equal area projection of the high-temperature component directions for 96 stable samples in the Burqin locality and 168 stable samples in the Tieersihabahe locality. Closed (open) symbols: downward (upward) inclinations. A red (green) star represents the mean direction for the normal (reverse) polarity in each locality based on its α_{95} circle of confidence. Black stars represent the overall mean direction of the section with its corresponding α_{95} circle of confidence.

In the Burqin section, 96 stable HTC directions were selected for calculation of the mean paleomagnetic direction: declination D = 359.6°, inclination I = 57.1°, k = 13.3, and α_{95} = 4.1° (precision parameter and half-angle ***radius*** of the ***95%*** ***probability confidence cone***) (Table 4.1). The presence of two opposite polarity directions yields a positive reversal test, (class B, following the classification of McFadden and McElhinny, 1990) (Figure 4.4). At 95% confidence, the difference between normal (N) and reverse (R) polarities is 5.7° (D_N = 0.1°, I_N = 64.4°, k = 12.0, α_{95} = 7.7°, N = 53 samples; D_R = 181.7°, I_R = 55.5°, k = 15.2, α_{95} = 6°, N = 43 samples) which is less than the critical angle γ_c = 8.2° (Figure 4.4).

The mean direction for the Tieersihabahe section was calculated for 168 samples yielding stable HTC (D = 0.1°, I = 59.7°, k = 11.8, α_{95} = 3.3°). The difference between normal and reverse polarity mean directions is 3.7° (D_N = 4.3°, I_N = 58.8°, k = 11.7, α_{95} = 5.5°, N = 62 samples; D_R = 177.4°, I_R = 60.1°, k = 12.4, α_{95} = 4.1°, N = 106 samples), which is less than the critical angle of 6.7°, indicating a positive reversal test (class B) (McFadden and McElhinny, 1990) (Figure 4.4).

To further explore the primary character of the HTC we analyzed separately two sets of samples; the first set was from the redbeds (siltstones and mudstones) and the second set was from white-grey mudstones to yellowish brown sandstones and siltstones. The first set of samples contained the magnetite and hematite as the carriers of magnetism; the second set of samples contained only magnetite. After inverting the individual reversal polarity samples we calculated the mean directions of both sets independently (Table 4.1). The result is illustrated in Figure 4.5. The confidence intervals for both sets of samples overlap noticeably in the Burqin and Tieersihabahe sections, suggesting that the two means cannot be

distinguished at the 95% level of confidence. Although the redbeds often are subject to inclination error (inclination shallowing) (Tauxe, 2008), in our study the mean directions for the redbeds and the greybeds demonstrated that there was no inclination shallowing and that the redbed data can be used for further paleomagnetic reconstructions.

The HTC obtained in the Paleogene and Neogene sediments of the Burqin and Tieersihabahe sections gave positive reversal tests and similar mean directions were obtained for sediments with different carriers of magnetization (hematite/magnetite in the redbeds and magnetite in the grey/yellowish beds). Therefore we interpret the HTC to be the primary carrier of magnetization.

4.5 Discussion

We built the age model for the studied sections using magnetostratigraphy and paleontological dating results from Zhang et al. (2007, 2011) (Figure 4.6). Figure 4.6 illustrates that in the north of the Junggar Basin the sedimentation rate was always low during Eocene–Miocene epochs, but increased from 0.76 cm/kyr at 45 Ma to 2.9 cm/kyr at 23 Ma. This may signify that one of the Tibetan uplift activations caused by penetration of the Indian continent into Asia moved into the northern Junggar area and caused the uplift of the Altay Mountains around 23 Ma. The Altay Mountains are situated between the Junggar block and Siberia and are the major source of sediments accumulated in the northern Junggar Cenozoic water basin. Uplift of the Altay Mountains would be accompanied by an increase in water flow and an increased sedimentation rate in the Junggar Basin.

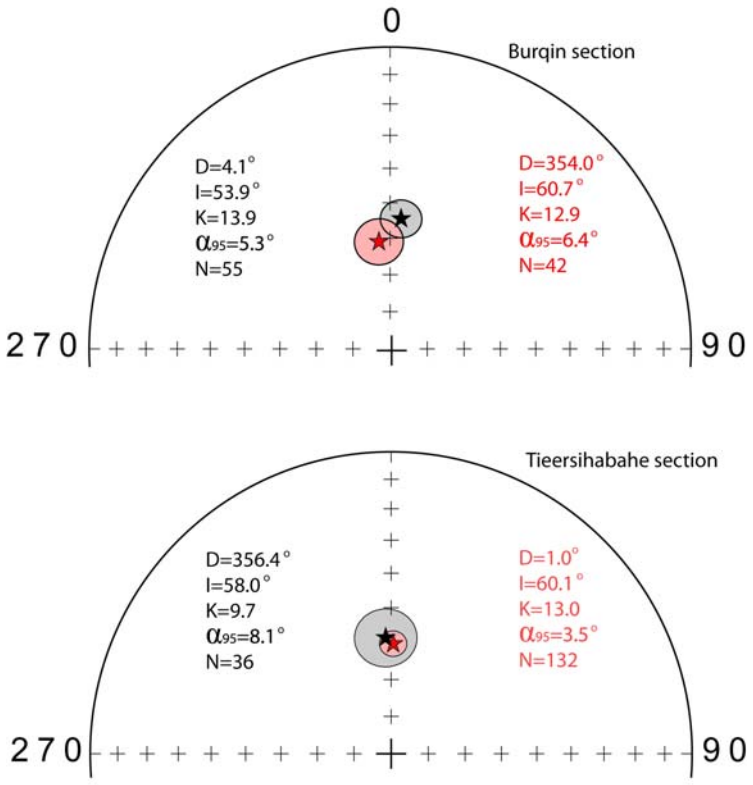

Figure 4.5 Comparison of the mean directions for the redbeds (siltstones and mudstones) and white-grey mudstones to yellowish brown sandstones and siltstones. Red (black) stars represent the mean directions of the redbeds (gray/yellowish sandstones/siltstones) based on a α_{95} circle of confidence in each locality. Note that the mean directions agree within a 95% confidence level implying that there is no inclination shallowing in the studied sections.

The increasing sedimentation rate from Eocene to Miocene periods agrees with data in Dai et al. (2006) and Charreau et al. (2009) from northeastern Tibet and the southern margin of the Junggar Basin, respectively. Dai et al. (2006, Figure 10) proposed that the higher sedimentation rate (from 2.3 cm/kyr up to ~4.0 cm/kyr for approximately the same time interval) was due to the proximity of the uplifting Tibet Plateau. However, the major change in sedimentation rate occurred around 35 Ma, earlier than in the northern Junggar, suggesting that processes related to the mountain uplift and continental compression took about 12 Myrs (from 35 to 23 Ma) to propagate from northern Tibet to the northern

Junggar Basin (about 1000 km). The speed of such propagation is on the order of a few cm/year which seems reasonable considering present-day continental drift rates. The sedimentation rate increase at ~23 Ma in the northern Junggar Basin indicates that the major Altay uplift caused by continental compression would have occurred after 23 Ma.

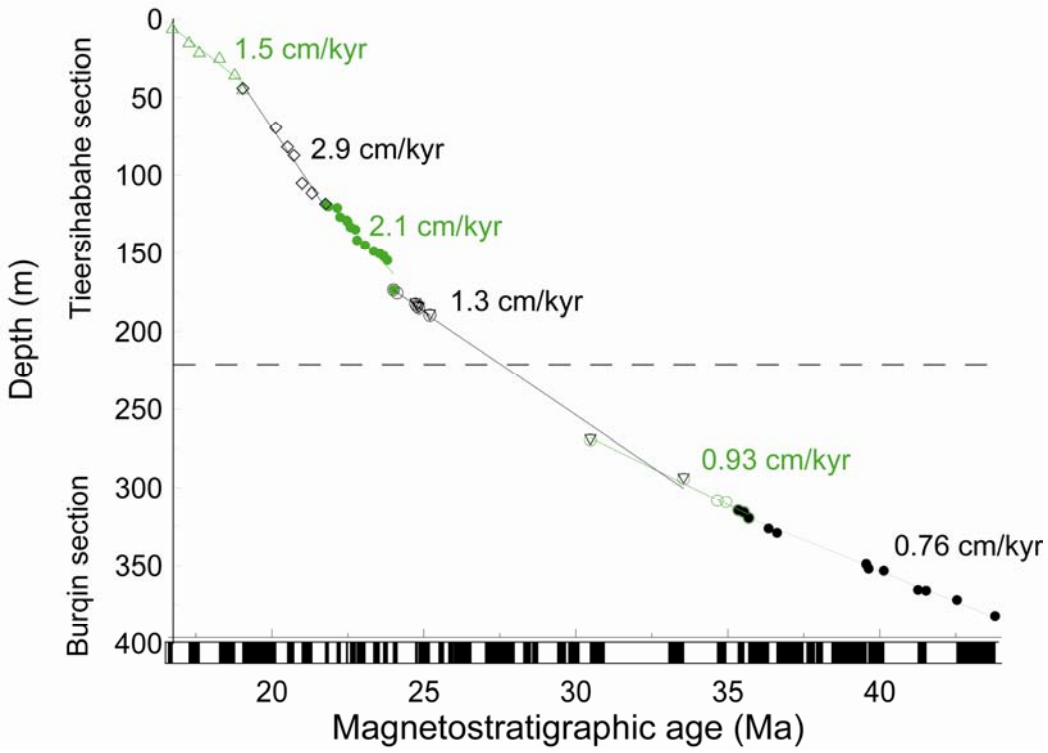

Figure 4.6 Stratigraphic level in meters versus age in Ma according to magnetostratigraphic dating for the Burqin (Zhang et al., 2011) and Tieersihabahe (Zhang et al., 2007) sections. The rate of sedimentation is given for samples retrieved from different layers of the studied areas.

We compiled existing reliable paleomagnetic poles for two study intervals from 44 to 25 Ma and from 25 to 14 Ma in central Asia in order to compare our new Junggar Basin results for 40 and 20 Ma with the major surrounding blocks at similar time intervals (Tables 4.2 and 4.3). Relative poleward displacement and apparent rotation with respect to the European apparent polar wander path (APWP)

from Besse and Courtillot (2002) were calculated for the poles (Figures 4.7 and 4.8), considering Europe to be a stable continental block. Calculations were performed following a procedure described by Coe et al. (1985). The majority of poles in the taken from the previous compilation of Hankard et al. (2007). However, for our reconstructions we chose only poles from internationally accessible sources where paleomagnetic procedures have been properly described. Some localities (denoted by asterisks) are listed in Tables 4.2 and 4.3 but are not shown on the maps in Figures 4.7 and 4.8 because we were not able to access the original papers; this restricted verification of the experimental procedures.

For a 44–25 Myr period the calculated paleopole for the Burqin locality presents a latitudinal offset of 12.2° ± 6.5° and a relative rotation of –17.2° ± 9.6° (negative sign means counter clockwise rotation) with respect to the reference 40 Ma European pole of Besse and Courtillot (2002). The observed latitudinal offset corresponds to ~1433 ± 764 km of intracontinental compression between the Junggar block and stable Europe. Such estimation is consistent with the Amuria block offset that ranges from 10.8° to 7.2° northward (Table 4.2, Figure 4.7). The Amuria block is a composite terrane for which relative rotations vary from –11.0° to 13.5° because small blocks of the terrane experience different amounts of rotation. The Kazakhstan block (Kyrgyzstan localities) offsets range from 13.2° to 19.2° northward displacement and have counter clockwise (CCW) rotations from –10.6° to –19.2°, consistent with our Junggar results and with results from India (15.9° northward displacement and –14.0° CCW rotation). These results imply that the northward displacement and CCW rotation of the Junggar block is related to the continuous accretion of India and Eurasia. Rotations can be correlated with the beginning of the formation of the Altay Mountain chain in the north and northeast of the Junggar Basin.

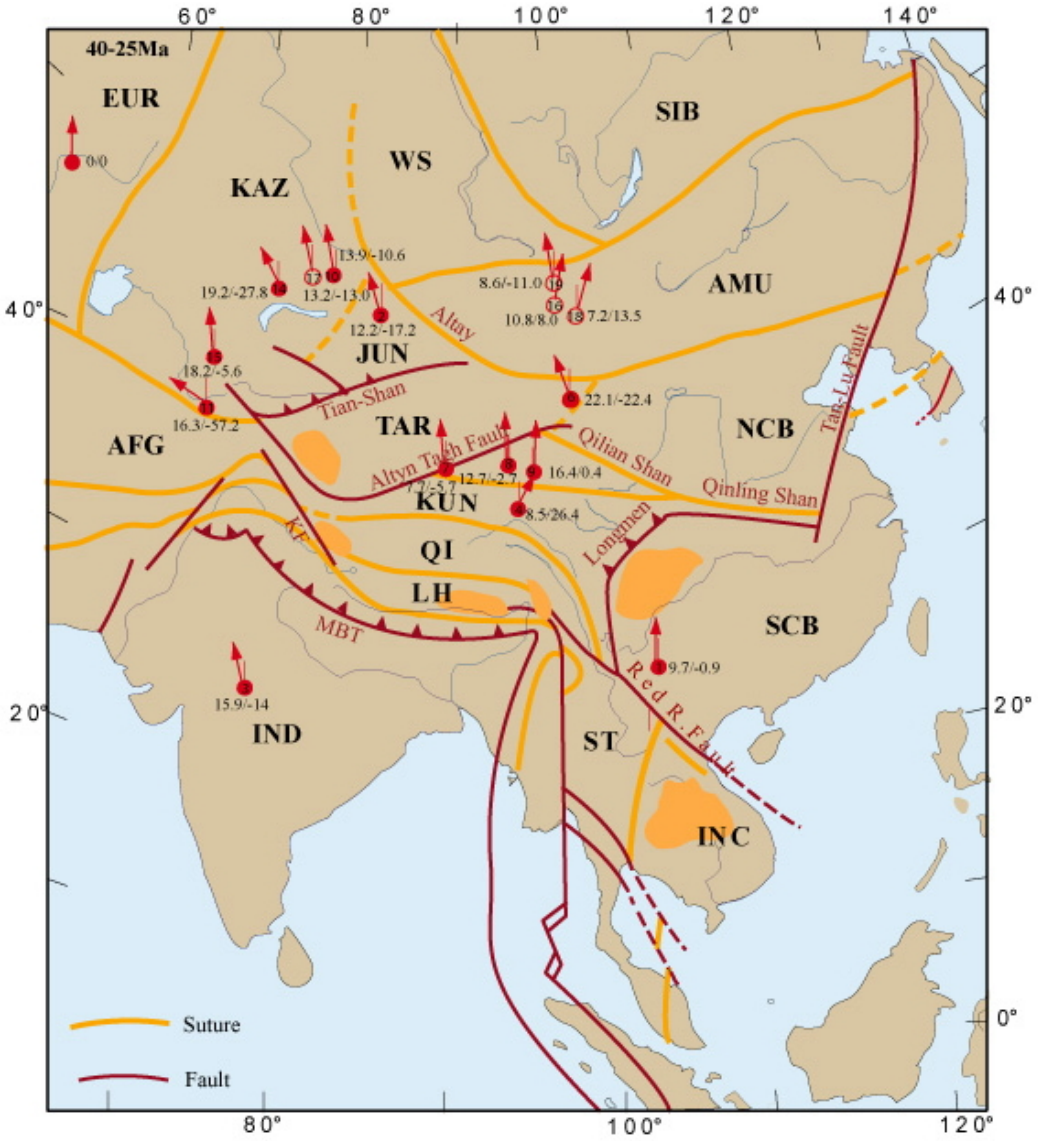

Figure 4.7 Compilation of paleomagnetic poleward displacements and rotations for Asia from 40 Ma to 25 Ma. Poleward displacements and rotations were calculated with reference to the European apparent polar wander path (APWP) of Besse and Courtillot (2002). Closed (open) circles represent sedimentary (volcanic) data. References are presented in Table 4.2.

Similar to our study, the effusive formations of Mongolia at ~40 Ma (Hankard et al., 2007) present a latitudinal offset of 10.8° ± 7.6° and an apparent rotation of 8.0° ± 10.7° with respect to the 40 Ma European pole of Besse and Courtillot (2002). These results and the fact that there are no high mountain

ranges in the Trans-Baikal area, led Hankard et al. (2007) to suggest that the Siberian continent that included this part of Mongolia at 40 Ma could be located ~1450 km farther south based on its expected paleolatitude calculated from the European reference pole. Our study demonstrates that the latitudinal displacement of the northern Junggar Basin (~1433 km) can be explained by intracontinental shortening and Altay Mountain formation without assuming a Siberia location toward the south. Alternatively, to explain the Mongolian 40 Ma latitude difference we may infer shortening between Mongolia and Siberia and the consequent growth of the Sayan Mountains.

For the 20 Ma Tieersihabahe locality (25–17 Ma interval poles) we obtained a latitudinal offset of 9.7° ± 4.1° (~1140 ± 482 km) and a CCW rotation of –11.8° ± 6.1° with respect to the 20 Ma pole of the European APWP (Besse and Courtillot, 2002). The rotation and poleward displacement between our two study localities from 40 to 20 Ma is negligible (2.5° ± 7.7° and –5.4° ± 15.7°), confirming that the Junggar Basin can be regarded as a single undeformed tectonic block. The latitudinal displacements and relative rotations at 40 Ma are 12.2° ± 6.5° and –17.2° ± 9.6° while at 20 Ma they are 9.7° ± 4.1° and –11.8° ± 6.1° compared to stable Europe during the corresponding time periods. The CCW rotation and intracontinental shortening between Junggar and Europe initiated before 40 Ma as a result of the Indo-Asian collision slowed down between 40 and 20 Ma in central Asia and reactivated only around or after 20 Ma. During the 40–20 Ma interval, the latitudinal displacement and relative rotation of the Junggar block and stable Europe were, respectively, 2.5° ± 7.7° (277.9 ± 856.2 km) and –5.4° ± 15.7°, which is lower than during the 20 Ma–present day interval of 9.7° ± 4.1° (1078.6 ± 455.9 km) and –11.8° ± 6.1°. This suggests that the major

intracontinental shortening between Junggar and Europe occurred at or after 20 Ma.

Large CCW rotations in the south of the Kazakhstan block observed at the Tajikistan depression can be related to the indentation of the Pamir Mountains into stable Asia (Thomas et al. 1994). Recent GPS results confirm a CCW rotation of the Junggar Basin at a rate of 0.3°/Myr (based on measurements in 1992–2006) about an Euler pole centered at 81.35°E, 40.57°N (Yang et al., 2008), compared with our result of 0.27°/Myr from 40 Ma to 20 Ma and 0.59°/Myr from 20 Ma to the present day. Cenozoic deformation of the Altay Mountains is characterized by east-trending thrusts and folds on the east side and a left-slip fault system on the west side of the Junggar Basin (Yin, 2010). Yin (2010) demonstrated that for the 30–20 Ma interval, continental shortening occurred only south of the Junggar Basin. His reconstruction of the shortening toward the north of Junggar 20–8 Ma agrees with our results. The Cenozoic uplift of the Gobi-Altay Mountain chain (one of the youngest mountain ranges in Central Asia) initiated 5 ± 3 Ma (Vassalo et al., 2007) confirms the relatively fast continental shortening north of the Junggar Basin after 20 Ma. Jolivet et al. (2009) used apatite fission track data to demonstrate an increase in tectonic activity in the Baikal rift system around the late Miocene–early Pliocene. Tectonic activity occurred along a NW–SE profile from the Siberian platform to the Barguzin Range across the Baikal–southern Patom Range and the northern termination of Lake Baikal. Their suggestion of increasing tectonic activity in the Baikai rift zone and east Sanyan after 20 Ma is compatible with our interpretation.

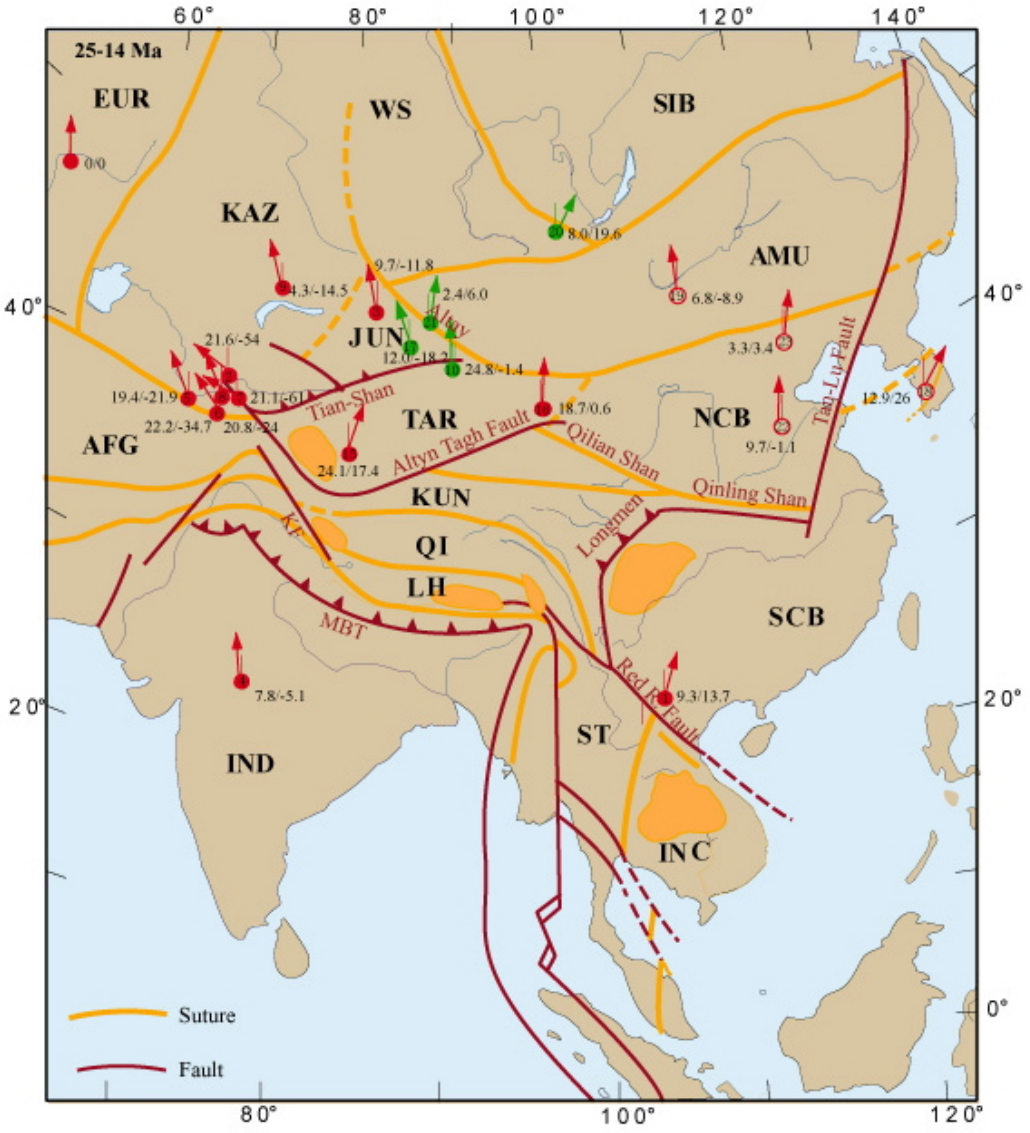

Figure 4.8 Compilation of paleomagnetic poleward displacements and rotations for Asia from 25 Ma to 14 Ma. Poleward displacements and rotations were calculated with reference to the European APWP of Besse and Courtillot (2002). Closed (open) circles represent sedimentary (volcanic) data. Data from mountain areas are represented by green circles. References are presented in Table 4.3.

4.6 Conclusion

We report the first paleomagnetic results for the Junggar block between ~40 Ma and ~20 Ma. Latitudinal displacements relative to the stable European craton

rotations (12.2° ± 6.5° and –17.2° ± 9.6° at 40 Ma and 9.7° ± 4.1° and –11.8° ± 6.1° at 20 Ma) are consistent with the displacement and rotations of India, Amuria, and Kazakhstan composite terranes as well as eastern Sayan which could characterize the edge of the Siberian platform. The rates of relative rotations and shortening are comparable with those of present day GPS data and the left-slip fault system in the west of the Altay Mountains. No significant vertical-axis rotation (–5.4° ± 15.7°) or intracontinental shortening (2.5° ± 7.7°) between the Junggar block and stable Europe was observed from 40 Ma to 20 Ma. The major intracontinental shortening and rotation between the Junggar block and Europe occurred after 20 Ma. The CCW rotation (–11.8° ± 6.1°) and northward shortening (9.7° ± 4.1°) of the Junggar block after 20 Ma are thought to be a the result of the continuous penetration of India into Eurasia that enforced the uplift of the Altay Mountains and increased the tectonic activity in the Baikal rift zone.

Table 4.2 Selected paleomagnetic poles from Asia for 40 – 25 Ma.

	Basin/Terrane	Mean Age (Ma)	Site		Paleomagnetic Direction		Paleomagnetic Pole		dp/dm (A_{95}) (°)	Paleolatitude Observed (°)	Poleward Displacement (°)	Apparent Rotation (°)	References
			Lat (°N)	Long (°E)	Dec (°)	Inc (°)	Lat (°N)	Long (°E)					
	Sediments												
1	South China Block	~45	22.9	108.4	5.7	35	83.6	228	11.2/6.5 (8.5)	19.6	9.7±7.4	-0.9±8.0	Zhao et al. [1994][a]
2	Northern Junggar Basin	40.0	47.8	86.7	359.6	57.1	79.9	268.5	6.0/4.3 (4.9)	37.7	12.2±6.5	-17.2±9.6	This study[b]
3	Indian Block	40.0	22.0	77.0	358.1	13.8	74.9	264.4	10.1/5.2 (7.2)	7.0	15.9±7.5	-14.0±7.9	Besse and Courtillot [2002][c]
4	Tibetan Plateau	30.5	35.0	93.0	36.6	44.3	57.4	188.8	7.7/12.7 (9.8)	26.0	8.5±8.2	26.4±9.3	Liu et al. [2003][d]
5	Tajikistan/Pamirs*	29.0	38.8	70.4	342.0	36.9	66.1	296.0	4.3/7.3 (5.6)	20.6	14.5±5.7	-27.5±6.5	Bazhenov and Burtman [1990][d]
6	China/Hexi	28.5	40.0	97.7	8.6	33.1	66.8	256.5	3.9/6.8 (5.2)	18.0	22.1±5.4	-22.4±6.5	Dupont-Nivet et al. [2003][d]
7	Altyn Tagh Range	28.5	38.9	91.4	5.0	49.6	80.6	243.9	4.8/7.2 (5.9)	30.5	7.7±5.8	-5.7±7.0	Dupont-Nivet et al. [2003][d]
8	Qaidam Basin	28.5	38.7	92.8	8.0	43.5	75.1	243.5	4.0/6.4 (5.1)	25.4	12.7±5.4	-2.7±6.5	Dupont-Nivet et al. [2002][d]
9	Qaidam Basin	28.5	37.5	95.2	11.0	37.3	70.8	242.3	7.9/13.5 (10.3)	20.8	16.4±8.5	0.4±9.5	Dupont-Nivet et al. [2002][d]
10	Kyrgyzstan/Northern Tien Shan	28.5	42.4	78.2	0.0	44.0	73.4	258.2	8.6/13.8 (10.9)	25.8	13.9±8.9	-10.6±10.2	Thomas et al. [1993][d]

Ref.: Reference number of the site locations on the map in Figure 4.7; Dec/Inc: paleomagnetic declination/inclination; dp /dm: semi-axes of the confidence circle of the palaeomagnetic pole; A_{95}: radius of the 95% confidence circle of the virtual palaeomagnetic pole. Poleward displacement and apparent rotations (positive difference indicates clockwise rotation) were calculated using the European APWP from Besse and Courtillot [2002] (data calculated for 10 Myr sliding window every 5 Myr, Table 5).

* Locality is not presented on map (Figure 7). Refer to the text for further explanation.

[a] APWP pole at 45 Ma: Lat =81.1°, Long = 150.4°, A95=5.3°.

[b] APWP pole at 40 Ma: Lat=78.8°, Long=160.2°, A95=7.3°.

[c] APWP pole at 35 Ma: Lat=81.2°, Long=173.4°, A95=4.6°.

[d] APWP pole at 30 Ma: Lat=81.6°, Long= 183.4°, A95=5.3°.

Table 4.3 Selected paleomagnetic poles from Asia for 25 – 14 Ma.

	Basin/Terrane	Age (Ma)	Site		Paleomagnetic Direction		Paleomagnetic Pole		dp/dm (A_{95})	Paleolatitude Observed (°)	Poleward Displacement (°)	Apparent Rotation (°)	References
			Lat (°N)	Long (°E)	Dec (°)	Inc (°)	Lat (°)	Long (°)					
	Sediments												
1	Yunnan Province/China	22.5	23.5	100.7	21.1	35.5	70.0	197.8	5.0/8.5 (6.5)	19.6	9.3±5.8	13.7±6.3	Haihong et al. [1995][a]
2	Tajikistan/Tukaynaron	22.5	38.8	69.6	317.1	33.3	47.5	323.0	7.0/12.5 (9.3)	18.2	21.6±7.6	-54.0±8.4	Thomas et al. [1994][a]
3	Northern Junggar	20.0	46.7	88.5	0.1	59.7	83.9	268.5	5.0/3.7 (3.3)	40.6	9.7±4.1	-11.8±6.1	This study[a]
4	India	20.0	22.0	77.0	4.0	30.7	83.4	221.9	6.0/3.4 (4.5)	16.6	7.8±4.7	-5.1±5.0	Besse and Courtillot [2002][a]
5	Tajikistan/Pulkhakim	19.5	38.1	67.4	349.0	35.1	69.0	277.5	8.5/15.0 (11.3)	19.4	19.4±8.9	-21.9±9.8	Thomas et al. [1994][a]
6	Tajikistan/Pyrygata	19.5	37.7	68.2	336.2	30.2	60.0	299.0	7.5/13.5 (10.1)	16.2	22.2±8.1	-34.7±8.8	Thomas et al. [1994][a]
7	Tajikistan/Kalinabad	19.5	38.0	69.0	309.9	32.7	42.0	328.5	6.0/10.0 (7.8)	17.8	21.1±6.6	-61.0±7.4	Thomas et al. [1994][a]
8	Tajikistan/Aksu	19.5	38.0	68.6	346.9	33.1	67.0	282.0	9.5/17.0 (12.7)	18.0	20.8±9.9	-24.0±10.7	Thomas et al. [1994][a]
9	Kyrgyzstan/Northern Tian Shan	19.5	42.2	76.7	357.0	59.0	86.7	300.6	10.0/13.5 (11.6)	39.8	4.3±9.1	-14.5±12.0	Thomas et al. [1993][a]
10	Turfan Basin	14.5	43.0	89.6	6.0	36.6	66.8	255.1	5.1/5.1 (5.1)	20.4	24.8±4.4	-1.4±5.2	Huang et al. [2004][b]
11	Uzbekistan/North Ferghana	14.5	41.2	71.9	354.9	54.9	83.0	288.0	1.0/1.4 (1.2)	35.4	6.2±2.5	-12.8±3.3	Abdullaev et al. [1993]*[b]
12	Uzbekistan/North Ferghana	14.5	41.0	72.8	348.6	46.8	74.0	292.0	7.5/11.6 (9.3)	28.0	13.5±7.2	-19.1±8.3	Abdullaev et al. [1993]*[b]
13	Uzbekistan/North Ferghana	14.5	41.1	72.2	358.9	54.6	84.0	261.0	1.0/1.4 (1.2)	35.2	6.4±2.5	-8.8±3.3	Abdullaev et al. [1993]*[b]
14	Uzbekistan/North Ferghana	14.5	41.5	72.2	357.0	47.6	77.0	264.0	5.0/7.8 (6.2)	28.7	13.2±5.1	-10.8±6.1	Abdullaev et al. [1993]*[b]
15	Central Tarim/China	14.0	38.5	80.5	24.7	29.5	58.6	210.0	3.8/6.8 (5.1)	15.8	24.1±4.4	17.4±4.9	Dupont-Nivet et al. [2002][b]
16	Nan Shan Range/China	14.0	39.1	96.7	7.2	40.7	73.0	253.5	4.2/7 (5.4)	23.2	18.7±4.6	0.6±5.3	Dupont-Nivet et al. [2003][b]
17	Jingou He/South Junggar (20Ma)	~8.1-23	44.2	85.5	348.5	53.1	76.2	309.6	2.2/3.2 (2.6)	33.7	12.0±3.0	-18.2±4.0	Charreau et al. [2009][c]
	Volcanic												
18	South Korea	20.5	36.0	129.5	30.1	50.2	64.5	222.1	10.4/15.5 (12.7)	31.0	12.9±9.9	26.0±11.8	Lee et al. [1999][a]
19	Inner Mongolia/China	20.0	41.0	116.2	358.1	60.1	88.6	29.2	9.4/7.1 (8.2)	41.6	6.8±6.9	-8.9±9.4	Zhao et al. [1994][a]
20	UstBokson/Siberia	19.9	52.1	100.3	31.7	66.5	69.8	186.5	8.4/10.2 (9.3)	49.0	8.0±7.6	19.6±12.1	Hankard et al. [2007][a]
21	Altai Mountains	17.0	46.9	90.0	17.7	65.9	78.0	167.6	12.1/9.9 (10.9)	48.1	2.4±8.7	6.0±13.1	Huang et al.[2006][a]
22	Shandong Province/China	16.0	36.3	118.6	5.0	53.3	85.2	238.4	6.7/4.6 (5.6)	33.8	9.7±5.3	-1.1±6.7	Zhao et al. [1994][a]
23	Hebei Province/China	15.0	41.0	114.7	8.7	61.0	83.4	192.8	6.2/6.2 (6.2)	42.0	3.3±5.1	3.4±7.0	Zheng et al. [1991][b]
24	Mongolia/Zavhan	14.0	46.5	96.5	18.7	67.6	77.0	162.0	21.0/17.6 (19.2)	50.4	-1.7±14.3	11.2±22.4	Gorshkov et al. [1991]*[b]

Ref.: Reference number of the site locations on the map in Figure 4.8; Dec/Inc: paleomagnetic declination/inclination; dp /dm: semi-axes of the confidence circle of the palaeomagnetic pole; A_{95}: radius of the 95% confidence circle of the virtual palaeomagnetic pole. Poleward displacement and apparent rotations (positive difference indicates clockwise rotation) were calculated using the European APWP from Besse and Courtillot [2002] (data calculated for 10 Myr sliding window every 5 Myr).

* Localities not presented on map (Figure ??). Refer to text for further explanation.

[a] APWP pole at 20 Ma: Lat =81.4°, Long = 149.7°, A95=4.5°.

[b] APWP pole at 15 Ma: Lat=84.2°, Long=154.9°, A95=3.2°.

[c] APWP pole at 10 Ma: Lat=85.0°, Long= 155.7°, A95=3.1°.

Bibliography

Bazhenov, M. L. & Burtman, V. S., 1990. Structural arcs of the Alpine Belt:Carpathians-Caucasus-Parmir (in Russian), pp. 168, Nauka, Moscow.

Besse, J. & Courtillot, V., 2002. Apparent and true polar wander and the geometry of the geomagnetic field for the last 200 Myr, Journal of Geophysical Research, 107(B11), 2300, doi:10.1029/2000JB000050.

Cande, S. C. & Kent D. V., 1995. Revised calibration of the geomagnetic polarity timescale for the Late Cretaceous and Cenozoic, Journal of Geophysical Research, 100(B4), 6093-6095, doi:10.1029/94JB03098.

Charreau, J., Chen, Y., Gilder, S., Dominguez, S., Avouac, J-P., Sen, S., Sun, D., Li, Y. & Wang, W., 2005. Magnetostratigraphy and rock magnetism of the Neogene Kuitun He section (northwest China): implications for Late Cenozoic uplift of the Tianshan mountains, Earth and Planetary Science Letters, 230, 177–192.

Charreau, J., Gilder, S., Chen, Y., Dominguez, S., Avouac, J-P., Sen, S., Jolivet, M., Li, Y. & Wang, W., 2006. Magnetostratigraphy of the Yaha section, Tarim Basin (China): 11 Ma acceleration in erosion and uplift of the Tian Shan mountains, Geology, 34, 181–184.

Charreau, J., Chen, Y., Gilder, S., Barrier, L., Dominguez, S., Augier, R., Sen, S., Avouac, J-P., Gallaud, A., Graveleau, F. & Wang, Q., 2009. Neogene uplift of the Tian Shan Mountains observed in the magnetic record of the Jingou River section (northwest China), Tectonics, 28, doi: 10.1029/2007TC002137.

Chauvin, A., Perroud, H. & Bazhenov, M. L., 1996. Anomalous low paleomagnetic inclinations from Oligocene-lower Miocene red beds of south-west Tien Shan, central Asia, Geophysical Journal International, 126, 303–313.

Chen, Y., Cogne, J-P., Courtillot, V., Avouac, J-P., Tapponnier, P., Wang, G., Bai, M., You, H., Li, M., Wei, C. & Buffetaut, E., 1991. Paleomagnetic study of Mesozoic continental sediments along the northern Tien Shan (China) and heterogeneous strain in central Asia, Journal of Geophysical Research, 96(B3), 4065–4082, doi:10.1029/90JB02699.

Coe, R. S., Globerman, B. R., Plumley, P. W. & Thrupp, G. A., 1985. Paleomagnetic results from Alaska and their tectonic implications, in Tectonostratigraphic Terranes of the Circum-Pacific Region, edited by Howell, D.G., pp. 85–108, Circum-Pacific Council for Energy and Mineral Resources, Houston, Texas.

Cogné, J.P., Y. Chen, Courtillot, V., Rocher, F., Wang, G., Bai, M. & You, H., 1995. A paleomagnetic study of Mesozoic sediments from Junggar and Turfan basins, NW China, Earth and Planetary Sciences Letters, 133, 353–366.

Dupont-Nivet, G., Butler, R.F., Yin, A. & Chen, X., 2002. Paleomagnetism indicates no Neogene rotation of the Qaidam Basin in northern Tibet during Indo-Asian collision, Geology, 30, 263–266.

Dupont-Nivet, G., Butler, R. F., Yin, A. & Chen, X., 2003. Paleomagnetism indicates no Neogene vertical axis rotations of the northeastern Tibetan Plateau, Journal of Geophysical Research, 108(B8), 2386, doi:10.1029/ 2003JB002399.

Gorshkov, E. S., Gooskova, E. G., Starunov, V. A., Tyuleneva, T. S., Ganhuyach, Z. & Khosbayar, P., 1991. Paleomagnetism of western Mongolia, paper presented at IV All-Soviet Union Congress on Geomagnetism, Vladimir-Suzdal, Russia.

Haihong, C., Dobson, J., Heller, F. & Jie, H., 1995. Paleomagnetic evidence for clockwise rotation of the Simao region since the Cretaceous: A consequence of India-Asia collision, Earth and Planetary Science Letters, 134, 203– 217.

Hankard, F., Cogne, J.P., Kravchinsky V.A., Carporzen, L., Bayasgalan, A. & Lkhagvadorj, P., 2007. New Tertiary paleomagnetic poles from Mongolia and Siberia at 40, 30, 20, and 13 Ma: Clues on the inclination shallowing problem in central Asia, Journal of Geophysical Research, 112 (B02101), doi:10.1029/2006JB004488.

Huang, B. C., Wang, Y. C., Liu, T., Yang, T. S., Li, Y. A., Sun, D. J. & Zhu, R. X., 2004. Paleomagnetism of Miocene sediments from the Turfan Basin, northwest China: No significant vertical-axis rotation during Neotectonic compression within the Tian Shan Range, central Asia, Tectonophysics, 384, 1–21.

Huang, B., Piper, J.D.A., Peng, S., Liu, T., Li, Z., Wang, Q. & Zhu, R., 2006. Magnetostratigraphic study of the Kuche Depression, Tarim Basin, and Cenozoic uplift of the Tian Shan Range, Western China, Earth and Planetary Science Letters, 251, 346–364.

Jolivet, M., De Boisgrollier, T., Petit, C., Fournier, M., Sankov, V. A., Ringenbach, J. C., Byzov, L., Miroshnichenko, A. I., Kovalenko, S. N. & Anisimova, S. V., 2009. How old is the Baikal Rift Zone? Insight from apetite fission track thermochronology, Tectonics, 28, TC3008, doi:10.1029/2008TC002404,

Kirschvink, J. L., 1980. The least-squares line and plane and the analysis of palaeomagnetic data, Geophysical Journal of the Royal Astronomical Society, 62, 699–718, doi: 10.1111/j.1365-246X.1980.tb02601.x.

Lee, Y. S., Ishikawa, N. & Kim, W. K., 1999. Paleomagnetism of Tertiary rocks on the Korean Peninsula: Tectonic implications for the opening of the East Sea (Sea of Japan), Tectonophysics, 304, 131–149.

Liu, Z., Zhao, X., Wang, C., Liu, S. & Yi, H., 2003. Magnetostratigraphy of Tertiary sediments from the Hoh Xil Basin: Implications for the Cenozoic tectonic history of the Tibetan Plateau, Geophysical Journal International, 154, 233–252.

McFadden, P. L. & M. W. McElhinny, 1990. Classification of the reversal test in paleomagnetism, Geophysical Journal International, 103, 725–729, doi:10.1111/j.1365-246X.1990.tb05683.x.

Thomas, J.-C., Perroud, H., Cobbold, P. R., Bazhenov, M. L., Burtman, V. S., Chauvin, A. & Sadybakasov, E., 1993. A paleomagnetic study of tertiary formations from the Kyrgyz Tien-Shan and its tectonic implications, Journal of Geophysical Research, 98, 9571–9590.

Thomas, J.-C., Chauvin, A., Gapais, D., Bazhenov, M.L., Perroud, H., Cobbold, P.R. & Burtman, V.S., 1994. Paleomagnetic evidence for Cenozoic block rotations in the Tadjik depression (Central Asia), Journal of Geophysical Research, 99, 15,141–15,160.

Vassallo, R., Jolivet, M., Ritz, J. F., Braucher, R., Larroque, C., Sue, C., Todbileg, M. & Javkhlanbold, D., 2007. Uplift age and rates of the Gurvan Bogd system (Gobi-Altay) by apatite fission track analysis, Earth and Planetary Science Letters, 259, 333–346.

Wu, W. Y., Ye, J. & Meng, J., 1998. Progress of study of Tertiary biostratigraphy in North Junggar Basin, Vertebrata PalAsiatica, 36(1), 24–31.

Yang, S., Li, J. & Wang, Q., 2008. The deformation pattern and fault rate in the Tianshan Mountains inferred from GPS observations, Science in China Series D: Earth Sciences, 51, 1064-1080.

Ye, J., Wu, W. Y. & Meng J. 2000. New result in the study of Tertiary Biostratigraphy in the Ulungur River Region of Xinjiang, China, Vertebrata PalAsiatica, 38, 192–202.

Ye, J., Meng, J. & Wu, W., 2003. Oligocene/Miocene beds and faunas from Tieersihabahe in the Northern Junggar Basin of Xinjiang, Bulletin of the American Museum of Natural History, 279, 568–585.

Ye, J., Meng, J., Wu, W. & Ni, X., 2005. Lithological and biostratigraphic sequence across the Eocene-Oligocene boundary in Burqin of Xinjiang, Vertebrata PalAsiatica, 43, 49–60.

Yin, A., 2010. Cenozoic tectonic evolution of Asia: A preliminary synthesis, Tectonophysics, 488, 293-325.

Zhang, R., Yue, L.P. & Wang, J.Q., 2007. Magnetostratigraphic dating of mammalian fossils in Junggar Basin, northwest China, Chinese Science Bulletin, 11, 1526–1531.

Zhang, R., Kravchinsky, V. A. & Yue, L.P., 2011. Reconstruction of the Missing Link between Global Cooling and Mammalian Transformation across the Eocene-Oligocene Boundary in the Continental Interior of Asia. *Submitted to* Palaeogeography, Palaeoclimatology, Palaeoecology.

Zhao, X., Coe, R. S., Zhou, Y., Hu, S., Wu, H., Kuang, G., Dong, Z. & Wang, J., 1994. Tertiary paleomagnetism of north and south China and a reappraisal of Late Mesozoic paleomagnetic data from Eurasia: Implications for the Cenozoic tectonic history of Asia, Tectonophysics, 235, 181– 203.

Zheng, Z., Kono, M., Tsunakawa, H., Kimura, G., Wei, Q., Zhu, X. & Hao, T., 1991. The apparent polar wander path for the North China Block since the Jurassic, Geophysical Journal International, 104, 29– 40.

Zijderveld, J.D.A., 1967. AC Demagnetization of Rocks-Analysis of Results, in Methods in Palaeomagnetism, pp.254-286, ed. Collinson, D.W., Creer, K. M., Runcorn, S.K, Elsevier, New York.

Chapter 5
Conclusions

This research first explored eolian sediments in the Chinese Loess Plateau in order to assess the paleomonsoon route and paleoenvironmental fluctuations during the last 130 kys in the regional area and eastern Asia. The AMS measurements shown in the steronet reveal clusters of maximum magnetic susceptibility axes in the SE quadrant and minimum magnetic susceptibility axes in the NW quadrant. To explain this result I postulate that the ellipsoild orientation of anisotropy of magnetic susceptibility is determined by the moist summer monsoon rather than by the dry winter monsoon as previously hypothesized. The major flow of paleowind for the last 130 kys was generally similar to the present day summer monsoon routes. I propose that, although the winter monsoon brings eolian sediments to the Plateau, the summer monsoon is stronger and has played a major role in the formation of the magnetic fabric in central and western parts of the Chinese Loess Plateau.

The second study presented here estimated the Eocene–Oligocene climate transition in central Asia and was compared with available records from Tibet, Mongolia and the ocean. Paleomagnetic analysis yielded reliable Characteristic remnant magnetization (ChRM) directions from 126 sample intervals, 11 with normal polarity and 11 with reversed polarity. The detailed magnetostratigraphy was determined by declination and inclination correlations to the geomagnetic polarity time scale (GPTS) of Cande and Kent (1995). Gradual change to a higher sedimentation rate, approximately at the Eolocene-Oligocene boundary (EOB) in our section, suggests that uplift of the Altay Mountains north of the Junggar Basin could have occurred due to shortening of the distance between India and northern Eurasia. I established that the faunal reorganization in the Junggar Basin occurred between 34.8 and 33.7 Ma; these results agree with

marine oxygen isotope data that demonstrate that the marine climate transition occurred 34.1–33.6 Ma, around the Eocene–Oligocene boundary (33.9 Ma). It is possible that central Asia experienced both cooling and aridification around the EOB, with the uplift of Tibet and retreat of the Paratethys epicontinental sea triggering aridification of the continental environment.

In my third research theme I obtained the first paleomagnetic poles for the Junggar block for the time between ~40 Ma and ~20 Ma and performed tectonic reconstructions of the paleopositions for the Asian blocks relative to the European continent. Latitudinal displacements relative to stable European craton rotations (12.2° ± 6.5° and –17.2° ± 9.6° at 40 Ma and 9.7° ± 4.1° and –11.8° ± 6.1° at 20 Ma) are consistent with displacement and rotations of the Indian craton, Amuria and Kazakhstan composite terranes, as well as Eastern Sayan which could characterize the edge of the Siberian platform. The rate of relative rotations and shortening between the Junggar block and the European craton compare well with present day GPS data and the left-slip strike fault system in the west of the Altay Mountains. No significant vertical-axis rotations (–5.4° ± 15.7°) and intracontinental shortening (2.5° ± 7.7°) between the Junggar block and stable Europe were observed from 40 Ma to 20 Ma. The major intracontinental shortening and rotation between the Junggar block and Europe occurred after 20 Ma. Counterclockwise rotation (–11.8° ± 6.1°) and northward shortening (9.7° ± 4.1°) of the Junggar block after 20 Ma are interpreted to be a result of the continuous penetration of India into Eurasia that enforced the uplift of the Altay Mountains and increased the tectonic activity in the Baikal rift zone.

Future work

It is still a matter of future study to verify if the AMS signals from the northern parts of the Chinese Loess Plateau fit my model of AMS signal formation. The winter monsoon wind in the north of the Plateau is much stronger than the summer monsoon wind and the magnetic particles may be oriented during winter only. Such a scenario could result in an AMS ellipsoid orientation toward the NW, i.e., in the direction opposite to the model proposed here.

To further identify the global cooling proposed during the Eocene – Oligocene boundary, a theory that is based on mammalian evolution, I plan to collect samples from pollen assemblages preserved in well-dated sediments. Palynological analyses combined with the paleoenvironmental reconstructions provided here may render an improved reference record.

My results showed that the major intracontinental shortening and vertical-axis rotation of the central Asian blocks happened mostly after 20 Ma. I propose to apply paleomagnetic techniques to the fossil-bearing sediments of Mongolia in order to extend my reconstructions of Cenozoic tectonic activity in central Asia between 45 Ma and the present day.